IDŐJÁRÁS

QUARTERLY JOURNAL
OF THE HUNGARIAN METEOROLOGICAL SERVICE

Special Issue: Weather forecasting and related applications
Guest Editors: **András Horányi** and **Tamás Weidinger**

CONTENTS

****

http://www.met.hu/Journal-Idojaras.php

VOL. 114 * NO. 1–2 * JANUARY– JUNE 2010

IDŐJÁRÁS

Quarterly Journal of the Hungarian Meteorological Service

Editorial Office: Gilice tér 39, H-1182 Budapest, Hungary
P.O. Box 39, H-1675 Budapest, Hungary
E-mail: bozo.l@met.hu or antal.e@met.hu
Fax: (36-1) 346-4809

Indexed and abstracted in Science Citation Index Expanded™ and Journal Citation Reports/Science Edition
Covered in the abstract and citation database SCOPUS®

Subscription by

mail: IDŐJÁRÁS, P.O. Box 39, H-1675 Budapest, Hungary
E-mail: kenderesy.k@met.hu or antal.e@met.hu

Editorial

Weather forecasting and related applications

During autumn of 2008, Meteorological Scientific Days (which is a traditional event of the meteorological society) were organized at the Hungarian Academy of Sciences on the subject of weather forecasting. The organization of this scientific event was ensured by the Working Committee of Atmospheric Dynamics under the Meteorological Scientific Committee of the Hungarian Academy of Sciences. After this workshop (see the presentations at http://www.met.hu/seminars/metnap2008.php), the idea arose to devote a special issue of the quarterly journal of the Hungarian Meteorological Service to this topic. Therefore, an invitation was submitted to the participants of the Meteorological Scientific Days and to other scientists working on the field of theoretical and applied weather forecasting (including researchers from other disciplines, who are applying weather forecasting information) to propose scientific papers to this special issue. Finally, eight articles were gathered, which are covering wide-range of topics on weather forecasting and related applications: data assimilation (including ensemble data assimilation), physical parameterization, ensemble forecasting, the special case of wind prediction for wind-power stations, environmental modeling, and urban heat island issues. All these subjects give a broad, but certainly not exhaustive overview of the weather forecasting and related applications in Hungary.

Unfortunately, there is also a bitter actuality of this special issue: the sudden and unbelievable death of our colleague and friend *Dezső Dévényi* (who was also member of the Editorial Board of IDŐJÁRÁS and also contributed to the special issue with the review of one of the article), therefore, we would like to dedicate the entire special issue to the memory of *Dezső Dévényi* (see the obituary of him in the same issue), since he had outstanding and long-lasting achievements to the topics of this special issue, i.e., on weather forecasting in general and numerical weather prediction in particular.

Finally, we would like to express our thanks to the Editor-in-Chief of IDŐJÁRÁS supporting the idea of the special issue, special gratitude is going to the authors of the articles and also to the dedicated reviewers making the critical review of the articles keeping the high standards of the journal. We are also grateful to the Executive Editor of the journal taking care about all the practical issues of the recent volume.

András Horányi[1] and *Tamás Weidinger*[2]
Guest Editors

[1]Hungarian Meteorological Service
[2]Eötvös Loránd University, Budapest

IDŐJÁRÁS

Quarterly Journal of the Hungarian Meteorological Service
Vol. 114, No. 1–2, January–June 2010, pp. 1–19

Diagnosis and tuning of background error statistics in a variational data assimilation system

Gergely Bölöni[1*] and **Kristian Horvath**[2]

[1]*Hungarian Meteorological Service*
P.O. Box 38, H-1525 Budapest, Hungary; E-mail: boloni.g@met.hu

[2]*Meteorological and Hydrological Service of Croatia*
Gric 3, Zagreb, HR-10000, Croatia; E-mail: horvath@cirus.dhz.hr

[*]*Corresponding author*

(Manuscript received in final form November 9, 2009)

Abstract—A very important source of information in data assimilation is the background, which is usually a short-range forecast of the numerical weather prediction (NWP) model valid at the assimilation time. The background is corrected by the atmospheric observations providing the analysis during the process of data assimilation. Errors of the background are estimated statistically and are taken into account with the aim of giving a proper weight to both the background and observations. Although, in theory, the background errors can be defined as the difference between the truth and the background, it is a great challenge to generate appropriate background error samples in practice for the computation of the background error statistics, because the true state is always unknown. A possible way to improve the background error representation is the development of the background sampling methods themselves. Another complementary approach is the "a posteriori" diagnosis or tuning of the already predefined background error statistics by a certain sampling technique. This paper presents two attempts for such a tuning within the ALADIN limited area model (LAM) and its 3d-var assimilation system used operationally at the Hungarian Meteorological Service (HMS). The first one is based on the comparison of the predefined statistics with those expected in a statistically optimal assimilation system. The second one is inspired by single observation experiments and it addresses the improvement of the multivariate statistical balance between humidity and the other analyzed variables.

Key-words: data assimilation, background errors, "a posteriori" tuning, multivariate statistical balance

1. Introduction

Data assimilation methods based on statistical optimality (*Gandin*, 1963; *Lorenc*, 1986; *Thépaut* and *Courtier*, 1991; *Bouttier* and *Courtier*, 1999) take into account the error of each available information type for weighting their

contribution to the analysis $\mathbf{x}_a$, i.e., the initial condition for the forecast. This is done by solving the so-called BLUE (best linear unbiased estimation) analysis equation:

$$\mathbf{x}_a = \mathbf{x}_b + \mathbf{B}\mathbf{H}^T\left(\mathbf{H}\mathbf{B}\mathbf{H}^T + \mathbf{R}\right)^{-1}\left(\mathbf{y} - H(\mathbf{x}_b)\right). \quad (1)$$

Main available information are the atmospheric observations $\mathbf{y}$ and the background $\mathbf{x}_b$, which is usually a short-range forecast of the NWP model. The notation H stands for the so-called non-linear observation operator, which projects from the space of the model variables to that of the observed variables. The operator $\mathbf{H}$ is the linearized of H. The matrices $\mathbf{B} = \mathrm{E}\left(\boldsymbol{\varepsilon}_b \boldsymbol{\varepsilon}_b^T\right)$ and $\mathbf{R} = \mathrm{E}\left(\boldsymbol{\varepsilon}_o \boldsymbol{\varepsilon}_o^T\right)$ denote the background and observation error covariance matrices respectively, where E stands for the statistical expectation. The corresponding errors are defined as the difference from the true state of the atmosphere $\mathbf{x}_t$, i.e., $\boldsymbol{\varepsilon}_b = \mathbf{x}_b - \mathbf{x}_t$ can be written for the background errors and $\boldsymbol{\varepsilon}_o = \mathbf{y} - \mathbf{H}(\mathbf{x}_t)$ for the observation errors. In the lack of $\mathbf{x}_t$ the sampling of these errors is a real challenge in the field of data assimilation. For the sampling of background errors, many ideas have been developed, like the method of innovations (*Hollingsworth* and *Lönnberg*, 1986; *Lönnberg* and *Hollingsworth*, 1986) or the NMC (*Parrish* and *Derber*, 1992) and Ensemble (*Fisher,* 2003; *Belo Pereira* and *Berre*, 2006; *Stefanescu et al.,* 2006) methods. Also attempts have been taken to characterize LAM specific background errors with the lagged-NMC approach (*Siroká et al.*, 2003). With the application of the above sampling techniques the representation of the background errors has been improved in some aspects indeed. In this paper, however, we would like to point out, that as $\mathbf{x}_t$ is never known, it is impossible to compute perfect $\mathbf{B}$ and $\mathbf{R}$ matrices with any method, and it is always reasonable to tune certain elements of the predefined covariance matrices "a posteriori". We will concentrate on the tuning of the $\mathbf{B}$ matrix statistics primarily, which was applied to the 3d-var system of the ALADIN model (*Horányi et al.*, 1996) in our experiments. In Chapter 2 we describe a tuning experiment aiming to improve the background error variances based on statistical optimality criteria of analysis residuals. In Chapter 3 we show a tuning to improve the multivariate balance in the analysis based on the simplified analysis Eq. (1) and single observation tests.

2. Tuning of the background error statistics based on covariances of residuals

Based on the optimal estimation theory, several approaches exist for "a posteriori" validation and tuning. A technique applied earlier in ARPEGE/ALADIN was based on the assumption that the expected value of the variational cost function J at the minimum is proportional to the number of observations used, i.e.,

$E(J_{min})=p/2$ hold, where p is the number of observations used in the analysis (*Talagrand*, 1998; *Désroziers* and *Ivanov*, 2001; *Chapnik et al.*, 2004; *Sadiki* and *Fischer*, 2005; *Fischer et al.*, 2005). Another method was proposed by *Désroziers et al.* (2006) later on, which is the theoretical basis for the tuning described in this chapter.

2.1. The method of tuning

It is explained in the above-mentioned paper that in a linear analysis system, where the **B** background and the **R** observation error covariance matrices are properly estimated, the following equations hold:

$$\begin{aligned} E\left(\mathbf{d}_b^o \mathbf{d}_b^{oT}\right) &= \mathbf{HBH}^T + \mathbf{R} \\ E\left(\mathbf{d}_b^a \mathbf{d}_b^{oT}\right) &= \mathbf{HBH}^T \\ E\left(\mathbf{d}_a^o \mathbf{d}_b^{oT}\right) &= \mathbf{R} \\ E\left(\mathbf{d}_b^a \mathbf{d}_a^{oT}\right) &= \mathbf{HAH}^T \end{aligned} \tag{2a}$$

where

$$\begin{aligned} \mathbf{d}_b^o &= \mathbf{y} - \mathbf{H}(\mathbf{x}_b) \\ \mathbf{d}_b^a &= \mathbf{H}(\mathbf{x}_a) - \mathbf{H}(\mathbf{x}_b) \\ \mathbf{d}_a^o &= \mathbf{y} - \mathbf{H}(\mathbf{x}_a) \end{aligned} \tag{2b}$$

are residuals of the model and the observations provided by the assimilation system. The notation **A** in Eq. (2a) stands for the analysis error covariance matrix. The optimality of the analysis system can be diagnosed if one computes the covariances of residuals on the left-hand side and substitutes the predefined error statistics to the right-hand side of Eq. (2a). The residuals on the left-hand side can be easily obtained as a by-product of the assimilation system. The second and the third equations in Eq. (2a) can be applied for instance for the diagnosis of the background and observation error standard deviations:

$$\sigma_{bd} = \sqrt{\frac{1}{P}\sum_{i=1}^{P} d_{bi}^a d_{bi}^o} \qquad \sigma_{od} = \sqrt{\frac{1}{P}\sum_{i=1}^{P} d_{ai}^o d_{bi}^o}\,, \tag{3}$$

where d_{bi}^a, d_{oi}^a, and d_{bi}^o stand for the individual i realizations of the background and analysis departures (i=1, …, P). Then the misfit of the predefined standard deviations (σ_{bp} and σ_{op}) can be obtained as follows:

$$r_b = \frac{\sigma_{bd}}{\sigma_{bp}} \qquad r_o = \frac{\sigma_{od}}{\sigma_{op}}\,. \tag{4}$$

These misfit ratios can be used as guidance for tuning the predefined standard deviations in the assimilation system. One has to notice, that through Eq. (1), the Eq. (2b) residuals depend on σ_{bp} and σ_{op}, which means that ideally the tuning with the misfit ratios and the computation of the analysis (Eq. (1)) should be done iteratively until r_b and r_o converge. It has also been shown by *Désroziers et al.* (2006) in a simplified system, that the convergence can be reached in a few iterations.

2.2. Estimation of the misfit ratios in our analysis system

The above method was applied in the ALADIN 3d-var system used at HMS (*Bölöni*, 2006) for the estimation of the misfit ratio for the background error standard deviations. The Eq. (2b) residuals were taken from two assimilation cycles run over an autumn (October–November 2005) and a summer (June 2006) period. In these assimilation cycles all the available observations were included, which are used operationally in the ALADIN 3d-var system at HMS (*Randriamampianina*, 2006). However, for the diagnosis of the background error standard deviations, only the residuals based on direct observations (i.e., radiosondes and aircrafts) were used. There was no iteration applied in the estimation for the sake of simplicity. In the fully spectral version of the ALADIN 3d-var system, predefined background error standard deviations are uniform horizontally and variable in the vertical, so they are available as one value for each model level and analyzed meteorological variables (i.e., temperature (T), specific humidity (q), vorticity (ζ), divergence (η)) (*Berre*, 2000). On the other hand, the diagnosed standard deviations can be obtained at the observation locations and for the observed quantities (T, q, and wind u, v components). In our estimation, a vertical averaging was applied both for the predefined and diagnosed values so that they became comparable independently from the height. For the comparison of predefined (ζ,η) and diagnosed (uv) wind error values, an average wind standard deviation (σ_b(uv)) was defined that can be computed as:

$$\sigma_{bd}(uv) = \sqrt{\frac{1}{2}\left(\sigma_{bd}^2(u) + \sigma_{bd}^2(v)\right)} \tag{5}$$

from the diagnosed u and v standard deviations values, and as:

$$\sigma_{bp}(uv) = \sqrt{-\frac{1}{2}\Delta^{-1}\left(\sigma_{bp}^2(\zeta) + \sigma_{bp}^2(\eta)\right)} \tag{6}$$

from the predefined ζ and η standard deviations, where Δ denotes the Laplace operator, i.e., the second space derivative in horizontal. *Table 1* shows the misfit

ratios computed as explained above and also the predefined and diagnosed background error standard deviations both for the autumn and summer periods.

Table 1. Predefined, diagnosed background error standard deviations and misfit ratios (dimensionless) for specific humidity (kg/kg), temperature (K) and average wind speed ($m\ s^{-1}$) computed over the autumn (October 26–November 10, 2005) and the summer (June 05–20, 2006) periods

Variable	**Predefined**	**Autumn period**		**Summer period**	
		Diagnosed	**Misfit ratio**	**Diagnosed**	**Misfit ratio**
	(σ_{bp})	(σ_{bd})	(r_b)	(σ_{bd})	(r_b)
Specific humidity (q)	2.27×10^{-4}	5.34×10^{-4}	2.35	5.82×10^{-4}	2.56
Temperature (T)	0.4917	0.7071	1.43	0.8010	1.62
Wind (u,v)	1.4840	1.9878	1.33	1.9203	1.29
Average	**0.65**	**0.89**	**1.36**	**0.9**	**1.38**

Large misfit ratios for humidity suggest that the humidity background error standard deviations are the less accurate as predefined by the original **B** matrix in our assimilation system. The misfit ratios are slightly different for the two different time periods, which suggests a possible seasonal dependence of the accuracy in the predefined background error modeling.

2.3. The tuning experiments

The analysis system can be tuned by multiplying the predefined standard deviations with the misfit ratios introduced in the previous section. In our experiments such tuning was done only for the background error standard deviations in two steps with different complexity:

1. ENS1 uses a uniform misfit ratio for all the variables and vertical model levels. This means that the misfit ratio used was averaged over the vertical levels and over the variables q, T, and wind.
2. ENS2 uses a variable dependent misfit ratio still averaged over the vertical levels.

It is to be mentioned, that the predefined statistics were computed based on the Ensemble sampling method. Both the ENS1 and ENS2 tuning options were tested in real assimilation cycling experiments over the summer period. It means a 16-day assimilation cycle (64 analysis steps) using the operational observational dataset. Simulations of 48-hour production runs were started from 00 UTC after 2 days of warm up cycling. The impact of the tuning was measured through rmse and bias score (e.g., *Wilks*, 1995) computations of the above-mentioned production forecasts against surface and radiosonde observations. The reference

assimilation cycle for the tuning experiments (ENS0) was the same as ENS1 and ENS2, except that no tuning of the background error standard deviations was applied, i.e., the predefined values were used. In experiment ENS1, a uniform misfit ratio, r_b=1.3 was used as a multiplication factor to increase the predefined background error standard deviations. This value was chosen based on the average misfit ratios shown in *Table 1*. The verification results show that the ENS1 tuning had no impact on the 2-meter parameters (not shown) but did improve the humidity forecasts on 700 hPa and the wind forecasts on 250 hPa (*Fig. 1b* and *d*). The impact on geopotential and temperature in the altitude was found to be rather neutral (*Fig. 1a* and *c*).

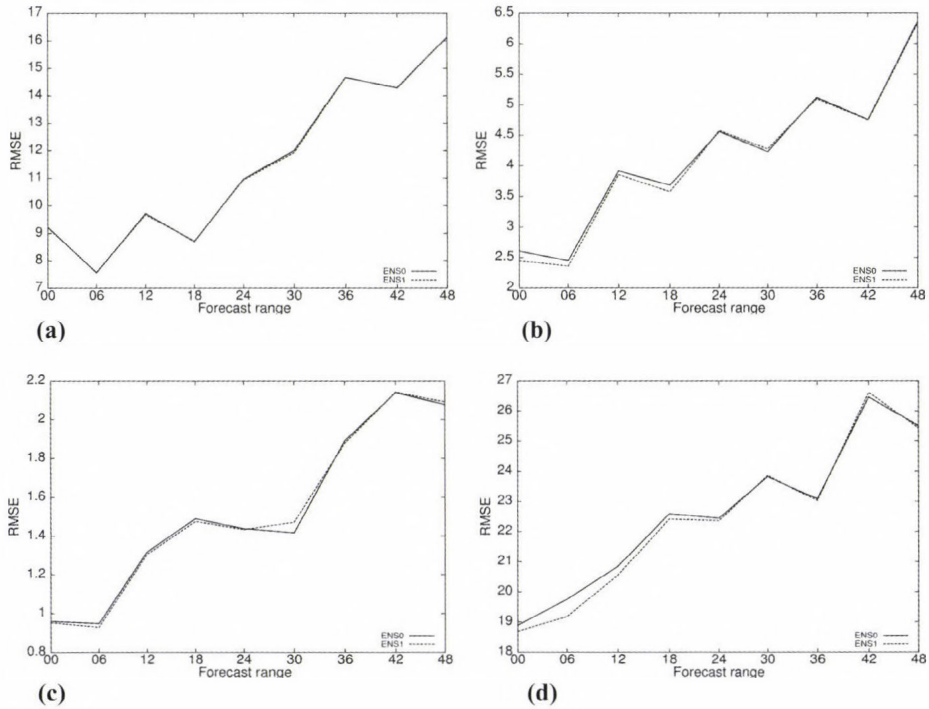

Fig. 1. Verification scores (rmse) computed for (a) geopotential at 500 hPa ($m^2\ s^{-2}$), (b) wind speed at 250 hPa ($m\ s^{-1}$), (c) temperature at 850 hPa (K), (d) relative humidity at 700 hPa (%). Dashed: experiment ENS1, solid: reference ENS0. The scores are computed over the period June 7–20, 2006.

In experiment ENS2, the misfit ratios computed from the autumn period were used. These are r_b=1.33 for the wind and mass variables (vorticity, divergence, surface pressure, and geopotential), r_b=1.43 for temperature, and r_b=2.35 for humidity, as shown in *Table 1*. The tuning had no impact on the 2-meter fields (not shown). Results for the atmospheric variables are displayed in *Fig. 2*. One

can see that ENS2 gives clearly worse results than the reference ENS0 for temperature on 850 hPa and also somewhat for relative humidity on 700 hPa. There is a positive impact of the tuning for the wind on 250 hPa.

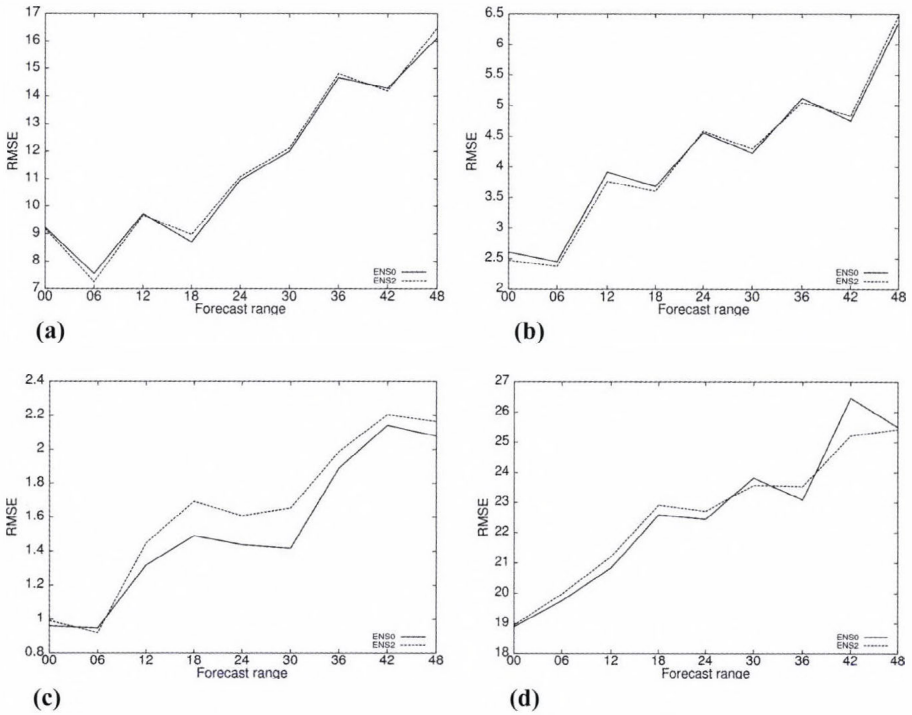

Fig. 2. Verification scores (rmse) computed for (a) geopotential at 500 hPa ($m^2\ s^{-2}$), (b) wind speed at 250 hPa ($m\ s^{-1}$), (c) temperature at 850 hPa (K), (d) relative humidity at 700 hPa (%). Dashed: experiment ENS2, solid: reference ENS0. The scores are computed over the period June 7–20, 2006.

The above results show that the uniform tuning (ENS1) provides better results than the variable dependent one (ENS2), which looks curious, because in theory Eq. (3) holds for each variable separately as well. In *Fig. 3* one can see the predefined and the tuned background error standard deviation profiles used in the experiments. It is obvious that the tuned profiles (ENS1 and ENS2) are quite similar to each other for wind. The difference is larger for temperature, and it is the largest for humidity. This suggests that the disappointing results of experiment ENS2 are mostly due to the large misfit ratios for humidity and temperature. A probable reason for the poorer result of the ENS2 experiment is that the misfit is averaged in the vertical, which can lead to an exaggerated tuning on those levels where the real misfit is drastically smaller than the average.

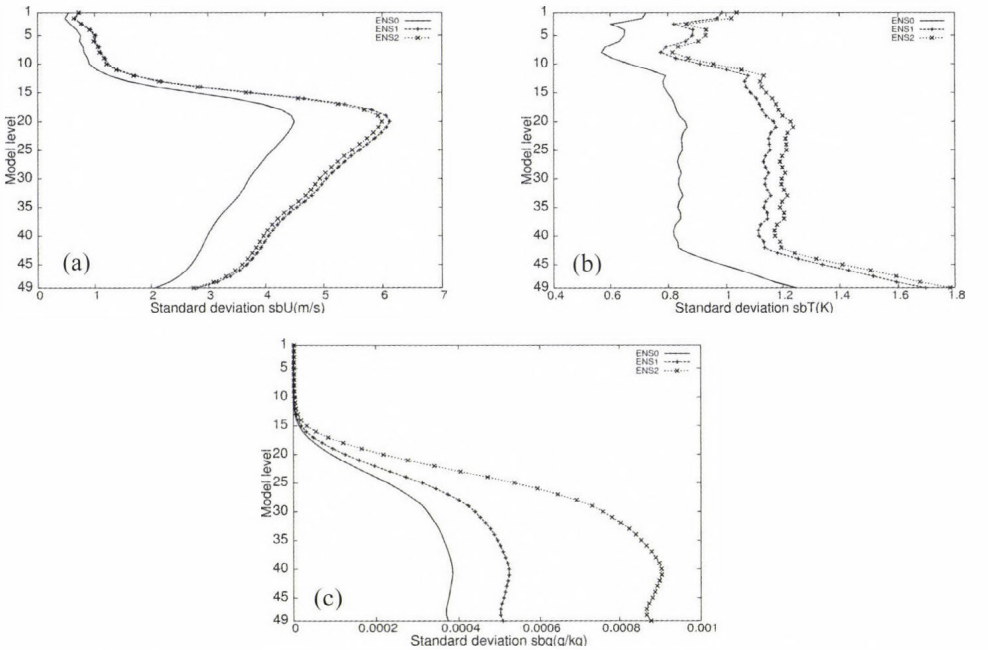

Fig. 3. Predefined (ENS0) and tuned (ENS1 and ENS2) profiles of total background error standard deviations of (a) wind, (b) temperature, (c) specific humidity.

3. Tuning of the multivariate balance

The ALADIN 3d-var is a multivariate analysis system provided by the statistical balance described by *Rabier et al.* (1998), *Courtier et al.* (1998), *Berre* (2000), and *Gustafsson et al.* (2001). In short, this statistical balance couples the analyzed variables in a meteorologically meaningful way by propagating a part of the increments of a given variable to those of another one. This insures the dynamical balance of the variables in the analysis. Experiments done at HMS showed that temperature observations have a large impact on the relative humidity analysis, which results in degradation of the relative humidity analysis and forecast verification scores in some weather situations. On the other hand, the humidity observations influence the temperature analysis in a very limited extent. This asymmetry in the multivariate balance brought us to study the analysis equation in a simplified framework and to propose a tuning of the error variances for a more symmetric balance.

3.1. Theoretical considerations

It can be shown that in a single point model (i.e., $\mathbf{H} = \mathbf{I}$, where $\mathbf{I}$ is the identity matrix), restricting to two variables only (T: temperature and Rh: relative humidity), the analysis Eq. (1) can be written as:

$$\delta T = \frac{\mathrm{cov}\left(\boldsymbol{\varepsilon}_{b,T}\boldsymbol{\varepsilon}_{b,Rh}\right)}{\sigma^2\left(\boldsymbol{\varepsilon}_{b,Rh}\right)+\sigma^2\left(\boldsymbol{\varepsilon}_{o,Rh}\right)}\Delta Rh\,, \tag{7}$$

where δ denotes the analysis increment (analysis minus background) and Δ stands for the observation increment or innovation (observation minus background). Based on *Daley* (1991) and *Hollingsworth* (1987), Eq. (7) can be decomposed as:

$$\delta Rh = \frac{\sigma^2\left(\boldsymbol{\varepsilon}_{b,Rh}\right)}{\sigma^2\left(\boldsymbol{\varepsilon}_{b,Rh}\right)+\sigma^2\left(\boldsymbol{\varepsilon}_{o,Rh}\right)}\Delta Rh \tag{8a}$$

$$\delta T = \frac{\mathrm{cov}\left(\boldsymbol{\varepsilon}_{b,T}\boldsymbol{\varepsilon}_{b,Rh}\right)}{\sigma^2\left(\boldsymbol{\varepsilon}_{b,Rh}\right)}\delta Rh\,, \tag{8b}$$

where (8a) is the univariate or filtering step, which provides humidity analysis increment from the humidity innovation and (8b) is the multivariate propagation step, which transforms the humidity analysis increment to temperature analysis increment. Multiplying and dividing the right-hand side of (8b) with $\sigma_b\left(\boldsymbol{\varepsilon}_T\right)$ and using the definition of the correlation, Eq. (8b) can be rewritten as:

$$\delta T = \mathrm{corr}\left(\boldsymbol{\varepsilon}_{b,T}\boldsymbol{\varepsilon}_{b,Rh}\right)\frac{\sigma\left(\boldsymbol{\varepsilon}_{b,T}\right)}{\sigma\left(\boldsymbol{\varepsilon}_{b,Rh}\right)}\delta Rh\,. \tag{8c}$$

In case of a temperature innovation, one can write the corresponding equations similarly to Eqs. (8a) and (8b) as follows:

$$\delta T = \frac{\sigma^2\left(\boldsymbol{\varepsilon}_{b,T}\right)}{\sigma^2\left(\boldsymbol{\varepsilon}_{b,T}\right)+\sigma^2\left(\boldsymbol{\varepsilon}_{o,T}\right)}\Delta T \tag{9a}$$

$$\delta Rh = \mathrm{corr}\left(\boldsymbol{\varepsilon}_{b,T}\boldsymbol{\varepsilon}_{b,Rh}\right)\frac{\sigma\left(\boldsymbol{\varepsilon}_{b,Rh}\right)}{\sigma\left(\boldsymbol{\varepsilon}_{b,T}\right)}\delta T\,. \tag{9b}$$

The asymmetry in the multivariate propagation step can be quantified as the ratio of T and Rh analysis increments induced by T and Rh innovations:

$$S = \left(\frac{\delta Rh}{\delta T}\right)_{\Delta T} \Big/ \left(\frac{\delta T}{\delta Rh}\right)_{\Delta Rh}\,. \tag{10}$$

The ratio **S** was computed within the ALADIN 3d-var system using single observations ($\Delta T = 1\,K$ and $\Delta Rh = 2\%$), taking the analysis increments right at the origin point (*Fig. 4*).

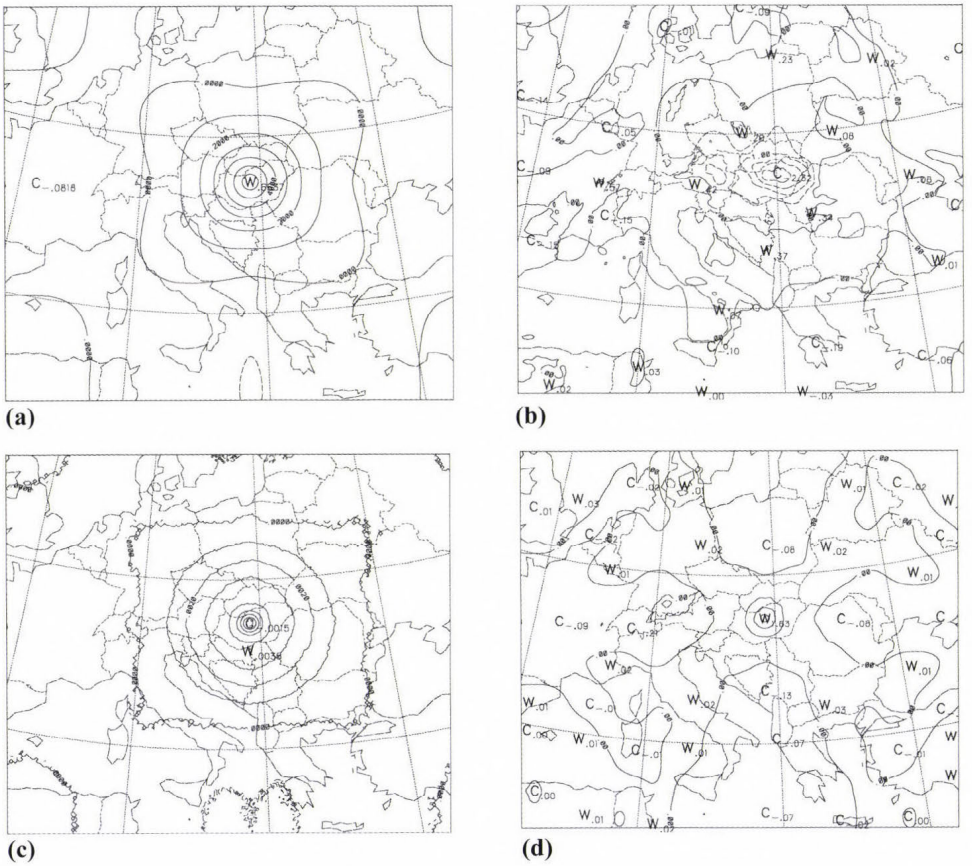

Fig. 4. Analysis increments due to single observations: (a) temperature increment induced by a temperature innovation, (b) relative humidity increment induced by a temperature innovation, (c) temperature increment induced by a relative humidity innovation, (d) relative humidity increment induced by a relative humidity innovation. The innovation values are $\Delta T = 1\,K$ and $\Delta Rh = 2\%$, observation error used are $\sigma(\varepsilon_{o,Rh}) = 0.12\%$, $\sigma(\varepsilon_{o,T}) = 1.1\,K$.

Note that the single observation experiments were run using NMC background error statistics sampled from differences of 36- and 12-hour forecasts of the operational ALADIN model over the period May–July 2004. Substituting the analysis increments shown in *Fig. 4* into Eq. (10), S≡3688 was found. It is easier to interpret this value if one writes up Eq. (10) using the Eqs. (8c) and (9b), which gives:

$$S = \left(\frac{\sigma\left(\boldsymbol{\varepsilon}_{b,Rh}\right)}{\sigma\left(\boldsymbol{\varepsilon}_{b,T}\right)} \right)^2 \cong 3688. \tag{11}$$

This shows that the symmetry of the multivariate coupling depends only on the variance ratios of the two variables. Taking the square root of the above equation one gets:

$$\sqrt{S} = \frac{\sigma\left(\boldsymbol{\varepsilon}_{b,Rh}\right)}{\sigma\left(\boldsymbol{\varepsilon}_{b,T}\right)} \cong 60 \frac{\%}{K}. \tag{12}$$

According to the above equation, a 1 K temperature error is associated to a 60% error in relative humidity and vice versa, which points out the rather asymmetric behavior of the multivariate propagation steps taking into account typical changes of temperature and humidity in the troposphere. The proposal for the tuning is thus to decrease the above ratio of standard deviations, which can be done either by increasing $\sigma(\boldsymbol{\varepsilon}_{b,T})$ or by decreasing $\sigma(\boldsymbol{\varepsilon}_{b,Rh})$. Examining the univariate steps in case of the T (*Fig. 4a*) and Rh innovations (*Fig. 4d*), one can see that the Rh analysis increment is about the 80% of the Rh innovation, while the T analysis increment is about the 60% of the T innovation. This means that the trust in the humidity background is indeed very small, which was the basis for assuming that $\sigma(\boldsymbol{\varepsilon}_{b,T})$ is well chosen and $\sigma(\boldsymbol{\varepsilon}_{b,Rh})$ is overestimated. As a consequence, it was decided to run tuning experiments by reducing the humidity background error standard deviations. An additional remark is that beside reducing humidity background error standard deviations, we considered to reduce also the humidity observation error standard deviations in order to keep Eq. (8a) univariate filtering step unchanged.

It should be clarified here, that the ALADIN 3d-var uses specific humidity (q) instead of relative humidity as analysis control variable, which also implies that the $\sigma(\boldsymbol{\varepsilon}_{b,q})$ specific humidity background error standard deviations were chosen for tuning instead of $\sigma(\boldsymbol{\varepsilon}_{b,Rh})$. The reason for using Rh in the above elaboration was that the asymmetry of the multivariate balance was observed first in relative humidity scores, and also the reader might judge relative humidity changes in the atmosphere easier than those of specific humidity.

Another feature that requires explanation here is that Rh single observation increments in *Figs. 4b* and *4d* show some obvious anisotropy in spite of the fact that the ALADIN horizontal background error structure is designed to be isotropic by origin (*Berre*, 2000). The clue for this seeming contradiction is that the anisotropy is not included by the structure functions directly but rather by the computation Rh from q. Namely, to derive and plot relative humidity

increments, first the $q \rightarrow Rh$ computation is performed both on the background and analysis fields, and then their difference is taken. As the $q \rightarrow Rh$ computation is a non-linear function of specific humidity and temperature, the resulting relative humidity increment will not keep the isotropic structure even if both specific humidity and temperature increments alone are isotropic.

3.2. The method of tuning

The extent of reduction of humidity errors was determined on the basis of an error estimation proposed by *Hollingsworth* and *Lönnberg* (1986) (HL method), which is independent from the NMC method. In short, the HL method estimates the observation and background errors based on the first equation of Eq. (2a), where the innovations are composed by the difference of radiosonde observations and model forecasts. By sorting the innovations in vertical and horizontal distance categories, one can estimate a vertical profile of observation and background error standard deviations and horizontal correlation length scales. This independent method was used as a guideline for estimating new background and observation standard deviations for humidity within our analysis system. The HL method was applied for the same period as the one used for the NMC sampling (May 2–August 2, 2004). The HL standard deviations were first computed on the standard levels of the radiosonde observations, and then they were interpolated on the model levels for the comparison with the NMC statistics.

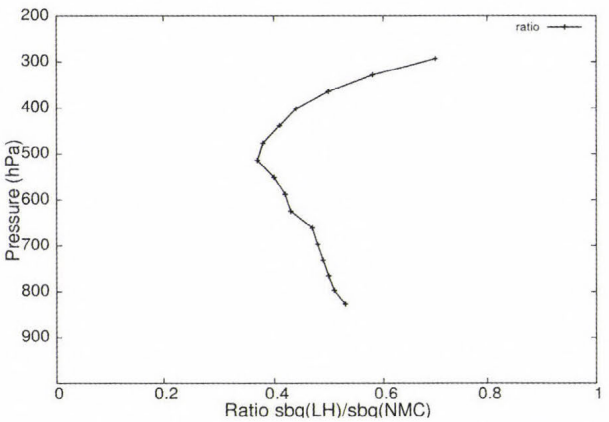

Fig. 5. Vertical profile of specific humidity background error standard deviation ratios obtained by the HL and NMC methods.

In *Fig. 5* the ratio of HL and NMC background error standard deviations are shown for specific humidity. Levels under 850 hPa were not considered for the tuning due to the small amount of radiosonde observations. Despite the strong vertical variability, the ratio is smaller than 1 for all the vertical levels,

which means that the HL estimation of $\sigma(\boldsymbol{\varepsilon}_{b,q})$ is smaller than the NMC one in the whole troposphere. This is in accordance with the notion of $\sigma(\boldsymbol{\varepsilon}_{b,q})$ being overestimated in the NMC statistics, which was also suggested by the theoretical considerations described earlier. Thus, it was decided to tune the $\sigma(\boldsymbol{\varepsilon}_{b,q})$ and $\sigma(\boldsymbol{\varepsilon}_{o,q})$ profiles used in the ALADIN 3d-var experiments according to the ratio profile shown in *Fig. 5*. Additionally, in some of the experiments $\sigma(\boldsymbol{\varepsilon}_{b,q})$ was drastically reduced (multiplied by a factor of 0.005) above 250 hPa in order to prevent to propagate high altitude humidity increments to the lower troposphere. This latter modification was based on the experiences at ECMWF (*Andersson et al.*, 1998).

3.3. The tuning experiments

The tuning experiments were run with the following three settings:

1. EX1Q: modified $\sigma(\boldsymbol{\varepsilon}_{b,q})$ between 850 and 250 hPa according to the HL/NMC ratio, reduced $\sigma(\boldsymbol{\varepsilon}_{b,q})$ above 250 hPa.
2. EX2Q: same as in EX1Q but also $\sigma(\boldsymbol{\varepsilon}_{o,q})$ is reduced in the same heights and in the same extent as $\sigma(\boldsymbol{\varepsilon}_{b,q})$.
3. EX3Q: same as EX2Q except that there was no tuning applied above 250 hPa.
4. REFQ: reference run using the predefined $\sigma(\boldsymbol{\varepsilon}_{o,q})$ and $\sigma(\boldsymbol{\varepsilon}_{b,q})$ values.

As a first step, the computation of Eq. (10) was repeated with the tuned error standard deviations based on single observation experiments again. It was proven that the tuning indeed reduced the asymmetry in the expected way as $\sqrt{S} = 35\%/\mathrm{K}$ was found with the EX1Q and $\sqrt{S} = 33\%/\mathrm{K}$ was obtained with the EX2Q settings. As a second step, complete assimilation cycles were run for a two-week period (August 29–September 10, 2004) with all the above experimental settings in order to see the impact of the tuning in a real operational-like context. The assimilation cycles were run with a 6-hour frequency, using surface, radiosonde, aircraft, and satellite (ATOVS AMSU-A and B) observations. Production forecasts (up to 48 hours) were run from the 00 UTC analyses. In general, the tuning had a smaller impact in these real cycling experiments than expected in terms of verification scores, which was surprising after the firm effect in the single observation experiments. This can be explained by the fact that the single observation experiments are much closer to the simplified system Eqs. (7)–(10) than the complex assimilation cycling experiments, where also the spatial correlations may play an important role. The largest impact was found for the experiment EX2Q, which will be referred in the further comparison against the reference run REFQ. In *Figs. 6* and *7*, bias and rmse scores for the analyses are shown for the EX2Q and REFQ runs. The tuning

resulted in a better (worse) fit to the observations concerning the temperature (humidity) analysis rmse. The impact on the wind analysis is rather mixed.

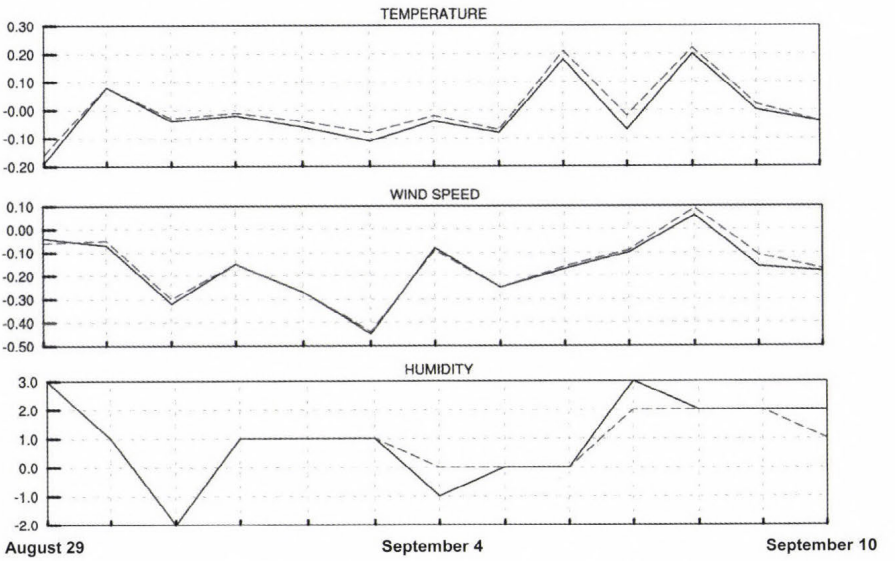

Fig. 6. Evolution of analysis bias scores for the experiments EX2Q (solid line) and the reference REFQ (dashed line). From top to bottom: temperature at 850 hPa (K), wind speed at 500 hPa (m s^{-1}), relative humidity at 700 hPa (%). The scores are computed over the period August 29 – September 10, 2004.

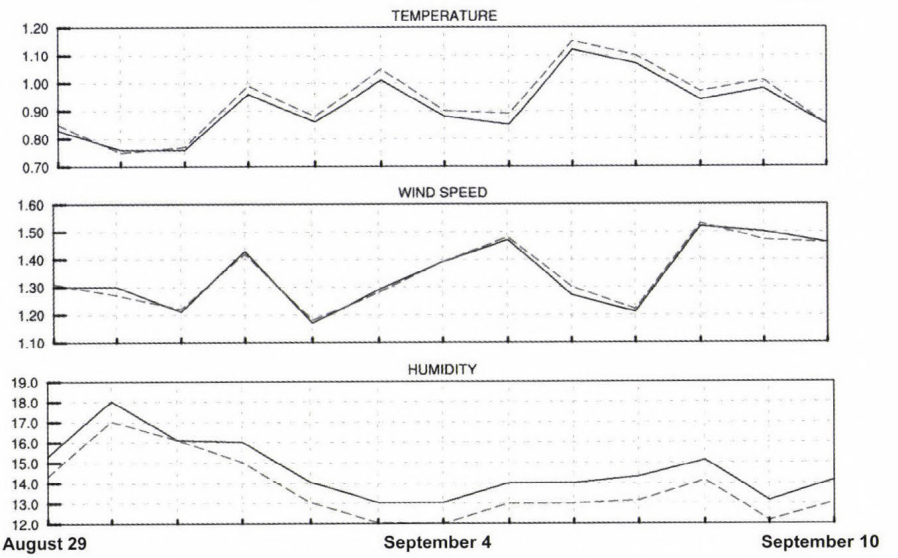

Fig. 7. Evolution of analysis rmse scores.....→

In our explanation the good fit of temperature comes indeed from the improved multivariate analysis, namely from a larger multivariate propagation of the humidity increments into those of temperature through the process described by Eq. (8b). On the other hand, the increased analysis departure of humidity may have two reasons: (i) multivariate humidity increments induced by those of temperature and wind became too small by excessively decreasing $\sigma(\boldsymbol{\varepsilon}_{b,q})$; and (ii) the univariate step of the humidity analysis Eq. (8a) was degraded by reducing $\sigma(\boldsymbol{\varepsilon}_{b,q})$, in spite of our compensation by reducing $\sigma(\boldsymbol{\varepsilon}_{o,q})$ at the same time.

Figs. 8 and *9* show that the positive impact on temperature decreases quickly with the forecast range. Nevertheless, humidity 6-hour forecast scores are improved by the performed tuning both in terms of bias and rmse. The impact on wind is kept mixed for this forecast range, while the overall effect of the tuning on longer forecast ranges is rather neutral (not shown).

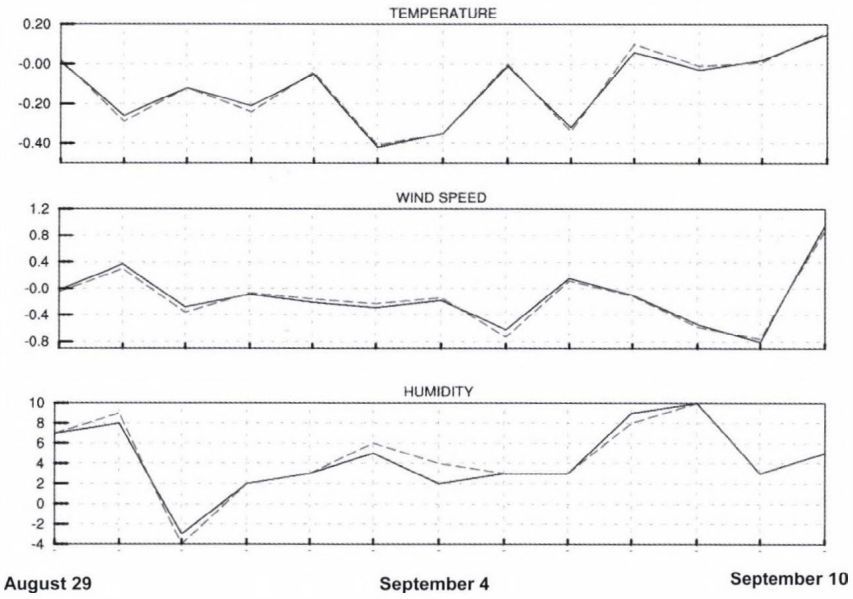

Fig. 8. Evolution of 6-hour forecast bias scores for the experiments EX2Q (solid line) and the reference (dashed line). From top to bottom: temperature at 850 hPa (K), wind speed at 500 hPa (m s^{-1}), relative humidity at 700 hPa (%). The scores are computed over the period August 29–September 10, 2004.

Fig. 7. Evolution of analysis rmse scores for the experiments EX2Q (solid line) and the reference REFQ (dashed line). From top to bottom: temperature at 850 hPa (K), wind speed at 500 hPa (m s^{-1}), relative humidity at 700 hPa (%). The scores are computed over the period August 29 – September 10, 2004.

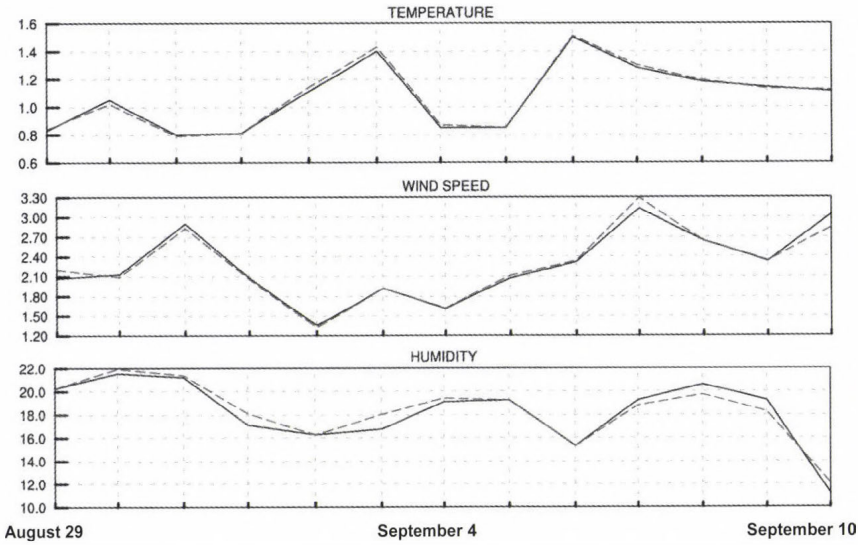

Fig. 9. Evolution of 6-hour forecast rmse scores for the experiments EX2Q (solid line) and the reference (dashed line). From top to bottom: temperature at 850 hPa (K), wind speed at 500 hPa (m s^{-1}), relative humidity at 700 hPa (%). The scores are computed over the period August 29–September 10, 2004.

4. Discussion

Two attempts to improve the Hungarian version of the ALADIN 3d-var analysis system were described. Both of them involve the tuning of the background and observation error standard deviations "a posteriori", but on a different theoretical basis.

The first tuning shown is based on the statistical optimality criteria derived by *Désroziers et al.* (2006) and aims to tune the errors for the full set of the background variables. The tuning was applied both in a variable dependent way and also as a uniform tuning for all the variables. A clear positive impact of the uniform tuning was found, while in the variable dependent case the verification showed a degradation of the forecasts. This seems to be a contradiction, as the more complex tuning had a worse impact than the simpler one. A probable explanation of this feature is that no vertical dependence of the tuning was included in any of the experiments, but a vertically averaged tuning ratio was used instead, being a considerable limitation of the approach. It is assumed that the degrading effect of the vertical averaging appears more intensively in the variable dependent tuning if the background error of the given variable shows a large vertical dependence (i.e., in the case of temperature and humidity). The uniform tuning has been introduced in the operational ALADIN 3d-var data assimilation system of HMS after the experiments.

The second tuning shown is based on the simplified BLUE analysis equations, proposing a modification only for the humidity errors. On the basis of single observation experiments, it was shown that the predefined error statistics produce an asymmetric multivariate balance between humidity and the other variables. Namely, humidity increments due to wind and temperature innovations are excessive compared to temperature and wind increments due to humidity innovations. On the basis of the simplified BLUE Eqs. (7)–(10), it was derived that the asymmetry can be decreased by reducing the background error standard deviations of humidity, which was demonstrated in a set of single observation experiments. To estimate the decrease in the humidity background error standard deviations the HL method was used (*Hollingsworth* and *Lönnberg*, 1986), which suggested a decrease of approximately half of the predefined standard deviation values on average. Full-observation experiments were performed with the modified multivariate propagation step, as well as experiments where the observation error standard deviations of humidity were also decreased to the same extent in order to keep the univariate analysis step unchanged. In real assimilation cycling experiments, the overall impact of the tuning was found to be quite moderate. This was probably caused by additional effects of spatial correlations of background errors, which were not taken into account in the simplified equations used as the basis of the tuning. However, a positive impact on 6-hour humidity forecasts was found with the application of the tuning procedure, suggesting that methodology and humidity tuning performed have a potential to improve humidity scores of numerical weather prediction models, at least for the shorter forecast ranges.

Note that the two tuning approaches described in the paper were performed independently from each other, mainly because they were motivated by independent problems. However, the two approaches are surely in a strong interaction, as both of them account for the modification of background error standard deviations. One can notice that the two tuning approaches propose to modify the humidity background error standard deviations in the opposite direction. This probably comes from the important fact that the tuning by residual covariances (Chapter 2) was based on predefined statistics sampled with the Ensemble method, while in the tuning of the multivariate balance (Chapter 3), the predefined statistics were sampled by the NMC method. Namely, background error standard deviations sampled by the Ensemble method are found to be smaller than those sampled by the NMC method (*Belo Pereira* and *Berre*, 2006; *Stefanescu et al.*, 2006), which may explain the seemingly opposing guidance on humidity tuning by the two tuning experiments. The change in the sampling method was due to better performance of the ALADIN 3d-var system of HMS using the Ensemble method, which entailed also its operational use. It is, thus, desirable to repeat the tuning of the multivariate balance within the Ensemble sampling framework in the future and to see its interaction with the tuning based on residuals covariances.

Acknowledgements—The authors would like to thank first the great help and encouragement given by *Loïk Berre* during the work related to the tuning of the multivariate balance. We also appreciate very much the advices of *Roger Randriamampianina* and *Claude Fischer* in several issues during our experimentations. The work of *Helga Tóth* is appreciated concerning the implementation of the HL diagnostic tool. We are very grateful for *Edit Adamcsek* for her useful suggestions regarding the text and formulas. This work was supported by the Hungarian National Scientific Foundation (OTKA T049579) and Ministry of Science, Technology and Sports of Republic of Croatia (MZOS project 0004001), as well as scholarship grants awarded by the Regional cooperation for Limited Area modeling in Central Europe and Hungarian Scholarship Board.

References

Andersson, E., Haseler, J., Undén, P., Courtier, P., Kelly, G., Vasiljevic, D., Brankovic, C., Gaffard, C., Hollingsworth, A., Jakob, C., Janssen, P., Klinker, E., Lanzinger, A., Miller, M., Rabier, F., Simmons, A., Strauss, B., Viterbo, P., Cardinali, C., Thépaut, J-N., 1998: The ECMWF implementation of three-dimensional variational assimilation (3D-Var). III : Experimental results. *Q J Roy Meteor Soc 124*, 1831-1860.

Belo Pereira, M. and *Berre, L.*, 2005: The use of an ensemble approach to study the background error covariances in a global NWP model. *Mon Weather Rev 134*, 2466-2489.

Berre, L., 2000: Estimation of synoptic and meso scale forecast error covariances in a limited are amodel. *Mon Weather Rev 128*, 644-667.

Bouttier, F. and *Courtier, P.*, 1999: Data assimilation concepts and methods. *ECMWF Lecture Series (Data assimilation and use of satellite data http://www.ecmwf.int/newsevents/training/lecture_notes/pdf_files/ASSIM/Ass_cons.pdf)*, 72.

Bölöni, G., 2006: Development of a variational data assimilation system for a limited area model at the Hungarian Meteorological Service. *Időjárás 110*, 309-327.

Chapnik, B., Désroziers, G., Rabier, F., Talagrand, O., 2004: Properties and first application of an erro- statisticstuning method in variational assimilation. *Q J Roy Meteor Soc 130*, 2253-2275.

Courtier, P., Andersson, E., Heckley, W., Pailleux, J., Vasiljevic, D., Hamrud, M., Hollingsworth, A., Rabier, F., and *Fisher, M.*, 1998: The ECMWF implementation of three dimensional variational assimilation (3D-Var). Part I: Formulation. *Q J Roy Meteor Soc 124*, 1783-1808.

Daley, R., 1991: *Atmospheric Data Analysis.* Cambridge University Press, Cambridge, 457 pp.

Désroziers, G. and *Ivanov, S.*, 2001: Diagnosis of adaptive tuning of information error parameters in a variational assimilation. *Q J Roy Meteor Soc 127*, 1433-1452.

Désroziers, G., Berre, L., Chapnik, B. and *Poli, P.*, 2006: Diagnosis of observation, background and analysis error statistics in observation space. *Q J Roy Meteor Soc 131*, 3385-3396.

Fischer, C., Montmerle, T., Berre, L., Auger, L., Stefanescu, S., 2005: An overview of the variational assimilation in the Aladin/France numerical weather prediction system. *Tellus 131*, 3477-3492.

Fisher, M., 2003: Background error covariance modelling. *ECMWF Seminar on Recent Developments in Data Assimilation for Atmosphere and Ocean*, 45-63.

Gandin, L.S., 1963: *Objective Analysis of Meteorological Fields.* Gidrometeorologicheskoe Izdatelstvo, Leningrad. English translation by Israeli Program for Scientific Translations, Jerusalem, 1965.

Gustaffson, N., Berre, L., Hörnquist, S., Huang, X.-Y., Lindskog, M., Navascués, B., Mogensen, K.S., and *Thorsteinnson, S.*, 2001: Three-dimensional variational data assimilation for a limited area model. Part I: General formulation and the background error constraint. *Tellus 53A*, 425-446.

Hollingsworth, A., 1987: Objective analysis for numerical weather prediction. Short and medium-range numerical weather prediction. *Proc. of the WMO/IUGG NWP Symp., Tokyo.* Meteorological Society of Japan, 11-59.

Hollingsworth, A. and *Lönnberg, P.*, 1986: The statistical structure of short-range forecast errors as determined from radiosonde data. Part I. The wind field. *Tellus 38A*, 111-136.

Horányi, A., Ihász, I. and *Radnóti, G.*, 1996: ARPEGE/ALADIN: A numerical weather prediction model for Central-Europe with the participation of the Hungarian Meteorological Service. *Időjárás 100*, 277-301.

Lorenc, A.C., 1986: Analysis methods for numerical weather prediction. *Q J Roy Meteor Soc 114*, 205-240.

Lönnberg, P. and *Hollingsworth, A.*, 1986: The statistical structure of short-range forecast errors as determined from radiosonde data. Part II: The covariance of height and wind errors. *Tellus 38A*, 137-161.

Parrish, D.F. and *Derber, J.C.*, 1992: The National Meteorological Centre's spectral statistical interpolation system. *Mon Wea Rev*, 1747-1763.

Rabier, F., Andersson, E., McNally, A., Courtier, P., Undén, P., Eyre, J., Hollingsworth, A., Bouttier, F., 1998: The ECMWF implementation of three-dimensional variational assimilation (3D-Var). II: Structure functions. *Q J Roy Meteor Soc 124*, 1809-1829.

Randriamampianina, R., 2006: Impact of high resolution observations in the ALADIN/HU model. *Időjárás 110*, 329-349.

Sadiki, W. and *Fischer, C.*, 2005: A posteriori validation applied to the 3D-VAR ARPEGE and ALADIN data assimilation system. *Tellus* 57A, 21-34.

Siroká, M., Fischer, C., Cassé, V., Brozková, R. and *Geleyn, J-F.*, 2003: The definition of mesoscale selective forecast error covariances for a limited area variational analysis. *Meteor Atmos Phys* 82, 227-244.

Stefanescu, S.E., Berre, L., and *Belo Pereira, M.*, 2006: The evolution of dispersion spectra and the evluation of model differences in an ensemble estimation of error statistics for a limited area analysis. *Mon Wea Rev 134*, 3456-3478.

Talagrand, O., 1998: A posteriori evaluation and verification of analysis and assimilation algorithms. *Workshop on Diagnosis of Data Assimilation Systems*, 2-4 November 1998, ECMWF, 17-18.

Thépaut, J.-N. and *Courtier, P.*, 1991: Four-dimensional data assimilation using the adjoint of a multilevel primitive equation model. *Q J Roy Meteor Soc 117*, 1225-1254.

Wilks, D.S., 1995: *Statistical Methods in the Atmospheric Sciences*. Academic Press, San Diego, California, 467 pp.

IDŐJÁRÁS

Quarterly Journal of the Hungarian Meteorological Service
Vol. 114, No. 1–2, January–July 2010, pp. 21–37

Application of the Ensemble Transform Kalman Filter technique at the Hungarian Meteorological Service: Preliminary results

Edit Adamcsek*, Gergely Bölöni, Petra Csomós, and **András Horányi**

Hungarian Meteorological Service
P.O. Box 38, H-1525 Budapest, Hungary
E-mails: adamcsek.e@met.hu; boloni.g@met.hu; csomos.p@met.hu; horanyi.a@met.hu

**Corresponding author*

(Manuscript received in final form March 18, 2010)

Abstract—The provision of the best background error estimates for data assimilation is crucial to derive the best initial conditions for a numerical weather prediction model. Using the Ensemble Transform Kalman Filter (ETKF) method a forecast ensemble can be generated at each analysis time, which can be used to estimate the background error statistics. The error growth implied by the forecast ensemble, which is measured with the forecast differences, characterizes the reliability of the actual background. In the present paper, the theoretical background of the Ensemble Transform Kalman Filter method is presented first. The ETKF transformation technique was applied in our tests for generating analysis ensemble containing the initial conditions for the model, then experiments were run with different setups to create forecast ensembles. At this stage of the research, estimation of the background errors was left aside, and as primary validation of this technique, the ensemble generation scheme and the transformation itself were studied. According to the results it can be said that the ensembles generated with the ETKF rescaling scheme have too small spread, which should be further improved with the proper application of the inflation procedure.

Key-words: data assimilation, Kalman Filter, Ensemble Transform Kalman Filter, transformation matrix, inflation factor, background errors

1. Introduction

Numerical weather prediction (NWP) is an intensively progressing field of meteorology, where the main objective is to numerically solve the set of hydro-thermodynamics equations for the prediction of the future states of the atmosphere. The numerical forecasts can be decomposed into two major steps: the determination of the initial conditions of the model and the model integration

itself. Since a small difference in the initial atmospheric state can evolve into a large change in the forecast (*Lorenz*, 1963), it is indispensable to have an estimation of the state of the atmosphere as accurate as possible. Data assimilation is the method for creating the analysis, the initial condition of the model, by combining observed values and background information (basically numerical weather prediction forecasts). A proper statistical estimation of observational and background errors is crucial in the assimilation process since it ensures the necessary weights of the available information in the course of assimilation. At the Hungarian Meteorological Service (HMS) the ALADIN 3d-var data assimilation system is used in the operational context, and for the time being, background errors are considered to be constant in time (*Bölöni*, 2006) and they are computed from a relatively small ensemble of ALADIN forecasts valid for a period of early spring. However, background forecast errors might be of variable quality depending on the season and weather situation. Kalman Filter is an approach to take into account the time dependency of background errors in the analysis cycle by ensuring the evolution of the background error covariance matrix from one analysis time step to another. The implementation of Kalman Filter, however, is computationally expensive in large dimensional systems such as numerical weather prediction models (*Evensen*, 2007), which excludes the possibility of a real time operational application with the currently available computer technology. In order to reduce the computing costs, ensemble techniques (so-called Ensemble Kalman Filter methods) have been introduced, where the background error covariance matrix is estimated from a small size sample of background forecasts. Different approaches exist for the generation of perturbations for these forecast ensembles, there are two main categories: perturbed observation Ensemble Kalman Filter (*Houtekamer* and *Mitchell*, 1998, 2001; *Hamill* and *Snyder*, 2000) and Ensemble Square-Root Kalman Filter (*Anderson*, 2001; *Whitaker* and *Hamill*, 2002; *Tippett et al.*, 2003; *Ott et al.*, 2004; *Hamill* and *Whitaker*, 2005). The so-called Ensemble Transform Kalman Filter (ETKF), which is a type of the Ensemble Square-Root Kalman Filters, has been used for targeted observations first (*Bishop et al.*, 2001; *Majumdar et al.*, 2001, 2002). Now it is tested for generating initial conditions for ensemble prediction systems (*Wei et al.*, 2006; *Johansson et al.*, 2009). The ETKF technique can be used for creating flow-dependent background errors as well. Since it is computationally inexpensive yet effective scheme, at the Hungarian Meteorological Service this method has been chosen for implementation. In this scheme the background perturbations are converted into analysis perturbations with the help of a transformation matrix. Using these dispersions an analysis ensemble is created, which will constitute the initial conditions for those model integrations which will form the ensemble system for the background error computations.

The paper is organized as follows. In the next section the basic concepts of data assimilation in general and Ensemble Transform Kalman Filter in particular

will be summarized. The transformation matrix, which is the heart of the ETKF procedure is presented in Section 3. Experiments realized so far are described in Section 4. Section 5 provides the summary, discussion, and conclusions of the present study.

2. Data assimilation and Ensemble Transform Kalman Filter

Data assimilation systems provide initial conditions for NWP models by using the actual observations and a background forecast valid at the analysis time as primary information for the assimilation procedure. First, the notations are summarized. From now on let x_a, x_f, and y denote the analysis and background fields, and the observations, respectively. Let n be the degree of freedom of the NWP model ($n \approx 10^7$, typically the number of variables to be determined for the entire model grid), and let p be the number of observations ($p \approx 10^4 - 10^6$). Then x_f and x_a are vectors of size n, and y is a vector of size p. Let $\mathcal{H}$ denote the observation operator, which maps the state variables on the model grid to the observational points, and let H denote its Jacobian matrix at the point x_f (i.e., around the background state, $H = \frac{\partial \mathcal{H}}{\partial x}(x_f)$). The background and observation error covariance matrices P_f and P_o, respectively, are defined as follows:

$$P_f \coloneqq E\left(\varepsilon_f \cdot {\varepsilon_f}^T\right) \text{ and } P_o \coloneqq E(\varepsilon_o \cdot {\varepsilon_o}^T), \tag{1}$$

where $E(\cdot)$ denotes the expected value, $\varepsilon_f = x_t - x_f$ and $\varepsilon_o = \mathcal{H}(x_t) - y$ stand for the background and observation errors, respectively, where x_t is the unknown, true state of the atmosphere. We call the attention that $\varepsilon_f \cdot {\varepsilon_f}^T$ is the diadic product of vectors ε_f and ${\varepsilon_f}^T$ (and similarly for $\varepsilon_o \cdot {\varepsilon_o}^T$). Similarly to Eq. (1), the analysis error covariance matrix can be defined as

$$P_a \coloneqq E(\varepsilon_a \cdot {\varepsilon_a}^T), \tag{2}$$

where $\varepsilon_a = x_t - x_a$. We define the matrix

$$K = P_f H^T (P_o + H P_f H^T)^{-1} \tag{3}$$

called the gain or weight matrix. Optimal least-square data assimilation methods estimate the true state of the atmosphere by the analysis using the following estimation (*Bouttier* and *Courtier*, 1999):

$$x_a = x_f + K(y - \mathcal{H}(x_f)). \tag{4}$$

In an assimilation system based on Eq. (4), the following relation is valid between the analysis and the background error covariance matrices (*Bouttier* and *Courtier*, 1999):

$$P_a = (I - KH)P_f \,, \tag{5}$$

where I denotes the identity matrix. In practice, the P_f background error covariance matrix is often assumed to be constant in time in data assimilation systems, however, it is rather well known that background errors depend on the actual weather situation to a great extent, therefore, it is desirable to release this consideration. The main idea of the Kalman Filter methods is to update matrix P_f at each analysis step. The standard Kalman Filter method was introduced by *Rudolf Emil Kalman* (1960), who has shown that the following equation can be derived for the forecast error covariance matrix at the time level t_i:

$$P_f(t_i) = M_{i-1}^{i} P_a(t_{i-1}) {M_{i-1}^{i}}^{T} + P_M(t_i), \tag{6}$$

where M_{i-1}^{i} is the linear model forecast operator at time level t_{i-1} (acting from time t_{i-1} to t_i, which is a matrix of size $n \times n$), $P_a(t_{i-1})$ is the analysis error covariance matrix at time t_{i-1} and $P_M(t_i)$ is the covariance matrix of the linear model error at t_i. Kalman introduced his technique originally only for the case of linear model M, however, it can be generalized for non-linear model $\mathcal{M}$, as well. Then M is the linearized of $\mathcal{M}$. Updating the P_f matrix based on Eq. (6) is computationally expensive. The evolution of the error covariance matrix requires at least $2n$ model integrations, and the storage of matrices of dimension $n \times n$, which is not practically tractable for an operational model with $n \approx 10^7$. In order to overcome these difficulties ensemble techniques were introduced. Such method is the Ensemble Transform Kalman Filter (ETKF), which is an approximation to the traditional Kalman Filter. It uses an ensemble (i.e., a statistical population) to estimate the error covariance matrices P_a and P_f. The matrix P_a can be estimated for k ensemble members as follows (see *Houtekamer* and *Mitchell*, 2001):

$$P_a \approx \frac{1}{k-1} \sum_{j=1}^{k} (x_{a,j} - \bar{x}_a) \cdot (x_{a,j} - \bar{x}_a)^T. \tag{7}$$

Let us consider

$$Z_a = \frac{1}{\sqrt{k-1}} (z_{a,1}, z_{a,2}, \dots, z_{a,k}), \tag{8}$$

the matrix of size $n \times k$, where the $z_{a,j} = x_{a,j} - \bar{x}_a (j = 1, \dots, k)$ values are the analysis dispersions, i.e., the differences between the jth member $x_{a,j}$ and the

ensemble average $\bar{x}_a$. Note, that with this notation the analysis error covariance matrix P_a can be written from Eq. (7) as

$$P_a = Z_a Z_a^T, \tag{9}$$

which is the product of matrix Z_a and its transpose. (It is remarked here that the Ensemble Transform Kalman Filter is one of the so-called square-root filters, because Z_a is the mathematical square-root of P_a according to Eq. (9); see *Tippett et al.*, 2003.) Using the above notations for Z_f and Z_a, the Kalman Filter method can be derived from the formula

$$Z_f = MZ_a, \tag{10}$$

where M is the linearized of the model operator $\mathcal{M}$. This means that the background dispersions are obtained by integrating the analysis dispersions with the linearized model. In the case of ETKF, instead of making k integrations as in Eq. (10), a relationship is assumed between the dispersions of the analysis and the dispersions of the background, that is

$$Z_a = Z_f T, \tag{11}$$

where $Z_f = \frac{1}{\sqrt{k-1}}\left(z_{f,1}, z_{f,2}, \dots, z_{f,k}\right)$ contains the background dispersions $z_{f,j} = x_{f,j} - \bar{x}_f$ $(j = 1, \dots, k)$, and T denotes the (for the time being unknown) transformation matrix of size $k \times k$ describing this relationship.

The Ensemble Transform Kalman Filter method (the schematic algorithm can be seen in *Fig. 1*) provides an ensemble generation scheme so as to estimate the background error covariance matrix by the covariance matrix of the ensemble forecast perturbations. Let us assume that k $(x_{f,1}, \dots, x_{f,k})$ forecasts have been created at the initial time. Then the matrix of the dispersions Z_f can be computed. The algorithm transforms forecast perturbations into analysis perturbations by the transformation matrix T, whose derivation is shown in the next section. The matrix $Z_a = Z_f T$ contains the dispersions to be added to the analysis x_a computed from the control member (e.g., $x_{f,1}$). The new background members $x_{f,j}^{new}$ are determined by integrating the model with the new analysis ensemble members $x_{a,j}$ $(j = 1, \dots, k)$ as initial states. From their dispersions the new values of the matrix P_f can be computed, then the procedure can be restarted.

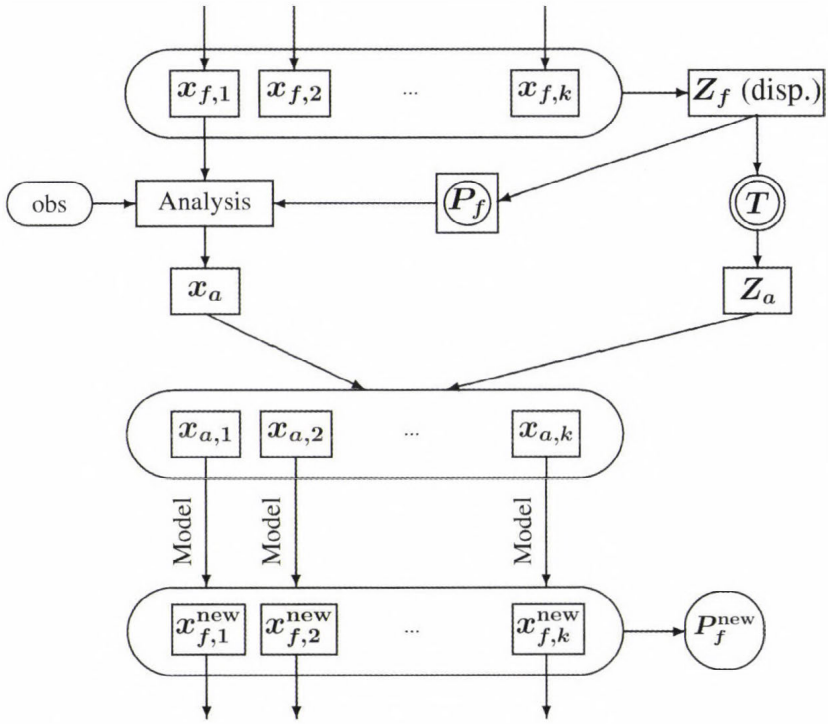

Fig. 1. The schematic algorithm of the Ensemble Transform Kalman Filter.

3. The transformation matrix

According to the Ensemble Transform Kalman Filter method the transformation matrix T is derived from the error covariance update, Eq. (5), provided that the matrix of background dispersions is the square-root of the background error covariance matrix. Hence, matrix T can be determined based on the following formulas:

$$\begin{aligned} Z_a &= Z_f T, \\ P_a &= (I - KH)P_f \ , \quad \text{where } K = P_f H^T (P_o + H P_f H^T)^{-1}, \\ P_f &= Z_f Z_f^T . \end{aligned}$$

Bishop et al. (2001) showed that according to the above assumptions, matrix T can be determined as

$$T = C(\Gamma + I)^{-1/2}, \tag{12}$$

where

$$Z_f^T H^T P_o^{-1} H Z_f = C \Gamma C^T. \tag{13}$$

Thus, matrix C contains the normalized eigenvectors of matrix $Z_f^T H^T P_o^{-1} H Z_f$, and the diagonal matrix Γ contains the corresponding eigenvalues.

The analysis perturbations $z_{a,j}$ obtained by the use of this T matrix are not centered around their mean, so the mean of the generated ensemble will not be identical to the analysis x_a. Ideally, one would like the ensemble mean to be equal to the best available estimate of the true state, that is, the analysis. Therefore, a centering method is required, which converts the analysis dispersions into centered ones. *Wang et al.* (2004) demonstrated that the method is to post-multiply the transformation matrix T by the matrix C^T to form the new, centered analysis dispersions: $Z_a = Z_f T C^T$. Hence, matrix T can be obtained as

$$T = C(\Gamma + I)^{-1/2} C^T. \tag{14}$$

However when the size of the ensemble k is significantly smaller than the rank of the true forecast error covariance, $P_a = Z_a Z_a^T$ underestimates total analysis error variance. To increase the ensemble covariance, the inflation method is used, that is, the analysis perturbations are multiplied by an estimated inflation factor Π: $Z_a = Z_f T \Pi$, which makes the transformation matrix to be computed as

$$T = C(\Gamma + I)^{-1/2} C^T \Pi. \tag{15}$$

In the following, the derivation of the estimation of the inflation factor can be read. The objective of the inflation method is to insure that the background ensemble variance P_f is consistent with the control forecast error. In order to insure this consistency, an equation is derived, which needs to hold. The following consistency diagnostic derived by *Desroziers et al.* (2005) is applied:

$$E(d \cdot d^T) = P_o + H P_f H^T, \tag{16}$$

where $d = y - \mathcal{H}(x_f)$ is the innovation vector: the difference of the observation vector y and its background counterpart $\mathcal{H}(x_f)$, that is the background forecast mapped into the observation space. Now define $\tilde{d}_i$ as the innovation vector at time level t_i, normalized by the square root of the observation error covariance matrix, that is, $\tilde{d}_i = {P_o}^{-1/2}(y_i - \mathcal{H}(x_i^f))$, where index i refers to the time level t_i. Let $\widetilde{\mathcal{H}}$ be the observation operator normalized by the square root of the observation error covariance matrix, that is $\widetilde{\mathcal{H}} = {P_o}^{-1/2}\mathcal{H}$, and let $\widetilde{H}$ be its linearized version. Now Eq. (16) can be rewritten as

$$E\left(\tilde{d}_i \cdot \tilde{d}_i^T\right) = I + \tilde{H} P_f(t_i) \tilde{H}^T, \tag{17}$$

where $P_f(t_i)$ indicates the background error covariance matrix estimated from the forecast ensemble at t_i. For the estimation of the inflation factor Π, this formula can be simplified as *Wang* and *Bishop* (2003) proposed:

$$\tilde{d}_i^T \tilde{d}_i = trace(I + \tilde{H} P_f(t_i) \tilde{H}^T). \tag{18}$$

The data of the next forecast being valid at t_{i+1} is not available at the update time t_i. Therefore, one assumes that the statistics of the next forecast will be similar to that at t_i, which may be a good approximation since the time interval between t_i and t_{i+1} is 6 hours in our experiments. Now the inflation factor is obtained by first checking if $\tilde{d}_i^T \tilde{d}_i$ is equal to $trace(I + \tilde{H} P_f(t_i) \tilde{H}^T)$, i.e., if Eq. (18) holds. If not, an inflation factor is needed: $Z_a = Z_f T \Pi_i$. Since $Z_f T \Pi_i = Z_f \Pi_i T$, the inflated ensemble covariance matrix is $\left(Z_f \Pi_i\right)^T Z_f \Pi_i = \Pi_i^2 Z_f^T Z_f = \Pi_i^2 P_f(t_i)$. To make Eq. (18) hold, the inflated covariance matrix is to be used, and the suitable inflation factor can be determined by the equation:

$$\tilde{d}_i^T \tilde{d}_i = trace\left(I + \tilde{H} \Pi_i^2 P_f(t_i) \tilde{H}^T\right). \tag{19}$$

From Eq. (19) using Eq. (13) we obtain:

$$\Pi_i = \sqrt{\frac{\tilde{d}_i^T \tilde{d}_i - p}{\sum_{j=1}^{k-1} \lambda_j}}, \tag{20}$$

where λ_j, $j = 1, \ldots, k-1$, are the diagonal elements of Γ. Using this inflation factor Eq. (19) will hold, which means that the new, inflated background ensemble variance P_f is consistent with the control forecast error.

4. Experiments

The preliminary experiments with ETKF were based on the ALADIN limited area model (LAM) and were embedded into an operational environment using real observations. A detailed description of the operational ALADIN LAM used in Hungary has been given by *Horányi et al.* (1996, 2006). The ETKF system needs an initial forecast ensemble, which was provided by the operational LAMEPS (Limited Area Model Ensemble Prediction System) used at HMS, which is the downscaling of the singular vector based global ensemble system PEARP (Prévision d'Ensemble ARPege) (*Hágel* and *Mile*, 2009). The members

of the same LAMEPS system were used as lateral boundary conditions for ETKF. As this particular ensemble includes one control forecast $x_{f,1}$ and ten perturbed members $x_{f,2}, \ldots, x_{f,11}$, the ensemble size of eleven was chosen in the experiments as well. The analysis in ETKF was provided by the ALADIN 3d-var data assimilation system used at HMS (*Bölöni*, 2006). Although the ultimate goal is to make the background error covariance matrix P_f flow-dependent, in these first experiments it was not yet updated from the ETKF ensemble, but always remained the static one used operationally. Therefore, the experiments have been limited to the examination of the transformation and perturbations so far.

4.1. Basic test of the transformation matrix

In this first experiment only one data assimilation step was performed. A detailed explanation on the practical computation of the transformation matrix and the perturbations was given by *Csomós* and *Bölöni* (2008). For the estimation of the inflation factor Eq. (20) was used. The innovation vectors were obtained from the initial forecast ensemble and observations (the same as used for the calculation of the transformation matrix). The very first estimation of the inflation factor was computed as $\Pi_1 = 10.06$. The analysis perturbations generated by ETKF were compared with those obtained by running eleven real 3d-var assimilations. The analysis perturbations in the latter case were provided in the following manner (as shown in *Fig. 2*). Eleven 3d-var assimilations were run using the same ensemble of background forecasts as in the ETKF run. In these computations the same background error covariance matrix (now denoted by B referring that it is constant in time) and the same set of observations were used, namely those used in the ETKF run. Finally, the perturbations were obtained by subtracting the analysis $x_{a,1}$ from each $x_{a,i}$ $(i = 1, \ldots, 11)$. Note that now the analysis $x_{a,1}$ is identical to the ETKF analysis x_a (see in *Figs. 2* and *3*).

The goal of this comparison was to investigate in what extent the transformation matrix approximates the real data assimilations. Although the two methods are different and the analysis perturbations are not expected to be the same, some resemblance must be shown. It was found that the spatial structure of the ETKF perturbations was very similar to those provided by the real 3d-var assimilation runs. As an example, one corresponding member of the perturbation sets is shown from the real assimilation and from the ETKF in *Fig. 4*. As a statistical comparison of the two analysis ensembles, the correlation of the corresponding members was computed, i.e., $cor\left(x_{a,i}^{a11}, x_{a,i}^{etkf}\right)$ $(i = 1, \ldots, 11)$, where the superscript corresponds to the derivation of the analysis. In *Fig. 5* the correlations are shown for some standard and physically important verification variables: 300 hPa wind components, 700 hPa relative humidity, and 850 hPa temperature. (In standard atmospheric situation the above-mentioned pressure levels are the corresponding model levels, i.e., level 15, 30, and 36, respectively.)

The analysis ensemble members are highly correlated, their correlation is above 0.974 for all variables, therefore, based on visual and then statistical comparison, it can be concluded that the transformation itself works well.

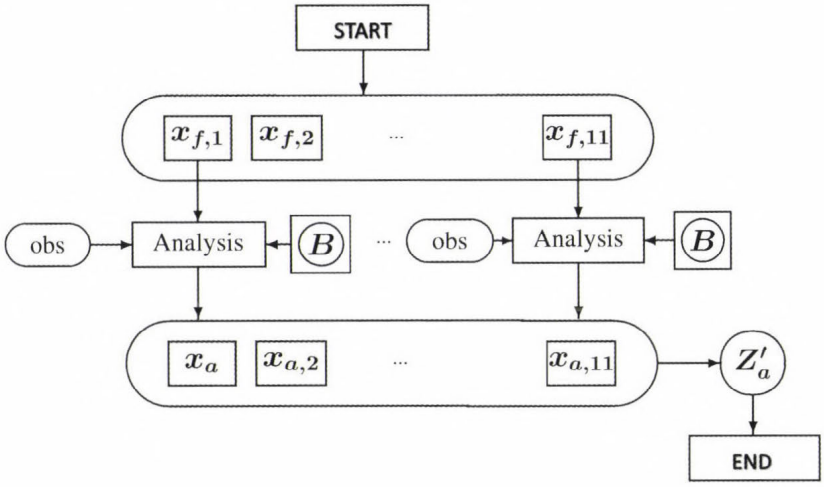

Fig. 2. The scheme of the eleven assimilations used for the test of the transformation matrix.

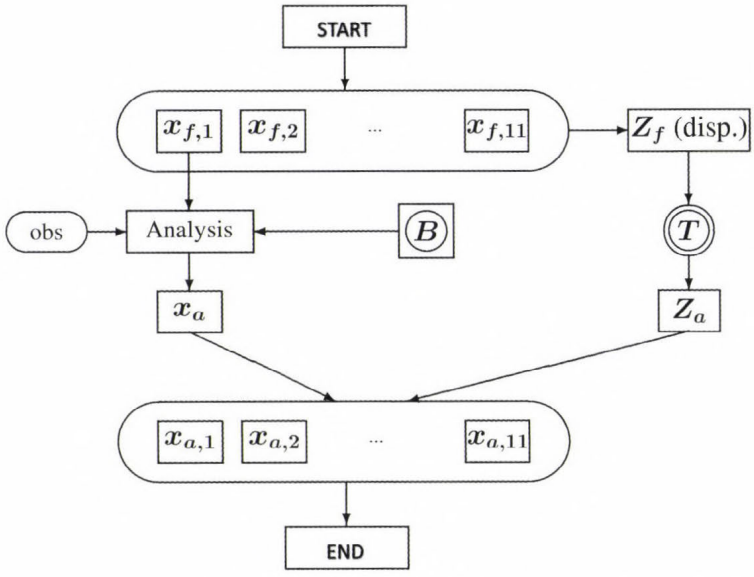

Fig. 3. The schematic algorithm of the Ensemble Transform Kalman Filter based ensemble generation scheme. The background error covariance matrix is now denoted with B referring to its static character used in the test with 11 ensemble members.

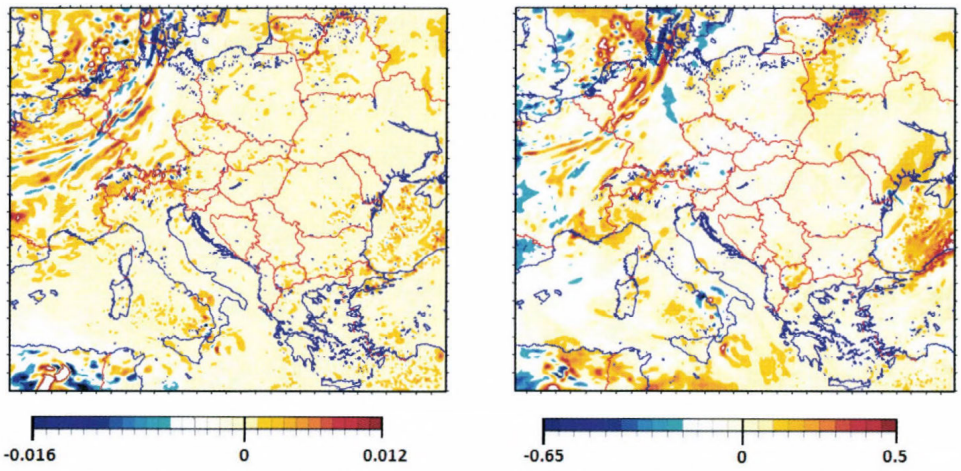

Fig. 4. The 5th analysis perturbation for temperature on the 36th model level obtained from the ETKF ensemble generation scheme (left) and obtained from the eleven assimilations (right).

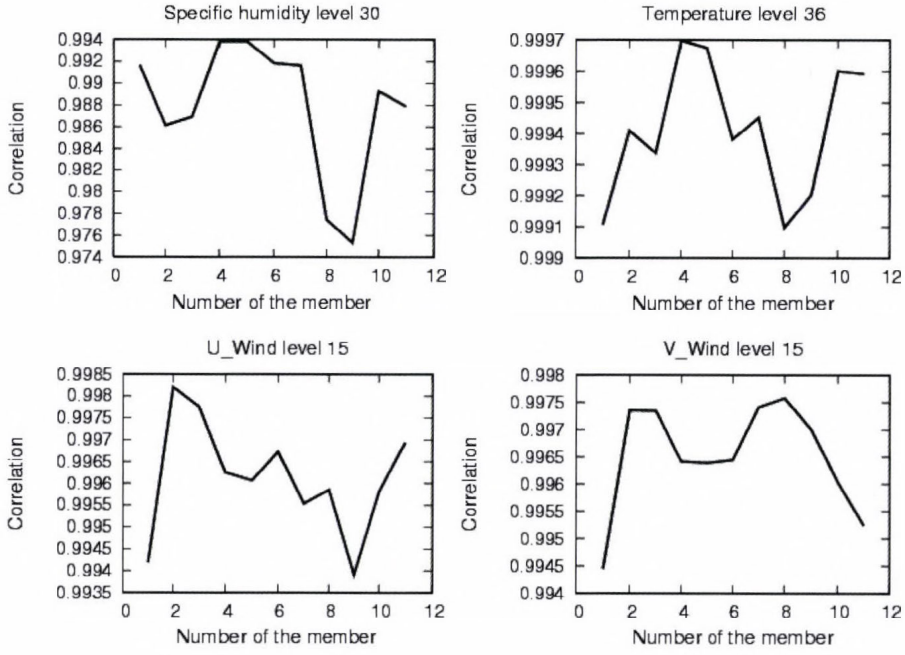

Fig. 5. Correlation of the corresponding analysis ensemble members for specific humidity at around 700 hPa (upper left panel), temperature at around 850 hPa (upper right panel), and zonal and meridional wind components at around 300 hPa (lower panels). On the x-axis the number of the ensemble members is shown, while y-axis shows the correlation value of the two analysis perturbation.

4.2. Experiments with inflation

In this experiment, the algorithm was organized in a cycle as shown in *Fig. 1*. The matrix P_f was still not updated, so the operational forecast error covariance matrix (denoted by B) was used at all analyses steps. The test was run from 00 UTC, September 3 to 18 UTC, September 9, 2008, which is a randomly chosen period, with a 6-hour cycling frequency in agreement with the operational data assimilation cycling setup at HMS. As already mentioned above, the lateral boundary conditions (LBCs) were taken from the operational LAMEPS system. Thus, a sufficient sample of analysis and background dispersions was collected for their statistical analysis.

In order to study the influence of the inflation factor on the perturbations, the following two experiments were run. In the first one, which provided a reference, there was no inflation used. In the second one the inflation factor was estimated in each analysis time as described above and built into the transformation matrix. The evolution of this parameter is shown in *Fig. 6* with solid line, it varies between 10.09 and 22.28.

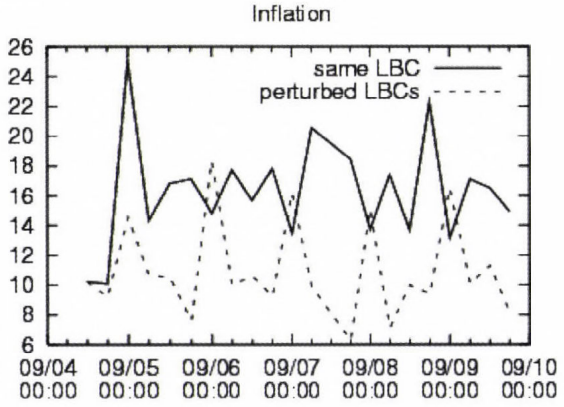

Fig. 6. Evolution of the inflation factor. The solid line represents the experiment with unperturbed LBCs and the dotted line is for experiment with perturbed LBCs.

In these tests the main intention was to focus purely on the impact of the inflation on the perturbations, therefore, the LBCs were kept constant for all the ETKF members, i.e., all of them were coupled to the same LAMEPS member. For the evaluation of forecast dispersions, the rank histograms (also known as Talagrand diagrams) were examined. For more details about the Talagrand diagram, *Hamill* (2000) is referred. These histograms were generated by verifying the forecast ensembles against ECMWF (European Center for Medium-Range Weather Forecasts) analysis. In *Fig. 7* the Talagrand diagram for the background ensembles are shown without and with inflation. It is

apparent that the extreme ranks are overpopulated, which indicates that there is a lack of variability in the ensemble. Although *Hamill* (2000) pointed out, that the U-shape of a Talagrand diagram can indicate conditional bias in the sampling (due to different weather regimes), in this specific case, where such a small sample was evaluated, we do think that the U-shape refers to under-variability. However, certainly the small sample size might prevent to have a really representative diagnostics. As some values appear in the middle ranks on the right panel in *Fig. 7*, the inflation had some minor impact on the variability, but it did not change the spread significantly. In order to gain additional variability in the background ensemble, it was decided that the LBCs are also to be perturbed.

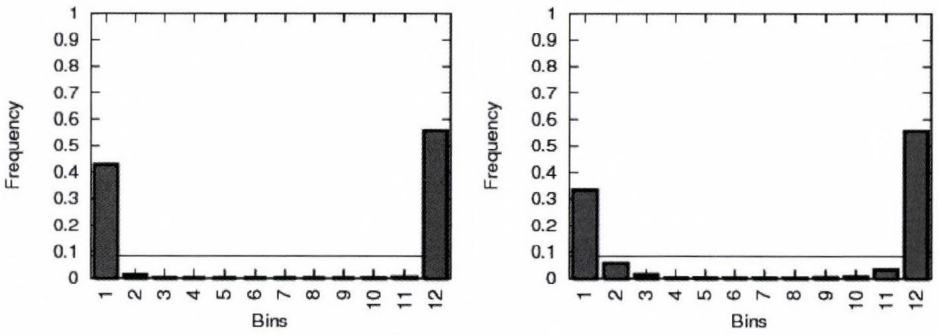

Fig. 7. Talagrand diagrams for forecast ensembles generated without inflation (left) and with inflation (right) for the period 00 UTC, September 3 to 18 UTC, September 9, 2008 for 925 hPa geopotential.

In a limited area model, such as ALADIN, the forecasts depend a lot not only on the initial, but also on the lateral boundary conditions. Thus, in this experiment, uncertainties through LBCs were also included beside the initial perturbations. This was achieved by coupling each member of the background forecast ensemble with a different member of the PEARP global system. It is to be mentioned that there is an inconsistency in this approach, since the perturbation generation methods are fundamentally different in the global and in the LAM system, e.g., the PEARP system applies the singular vector method and not ETKF. This coupling strategy was a technical constraint for we have no access to any global ETKF ensemble system. On the other hand, the effect of this inconsistency on our experiments is unknown. Both the inflated and un-inflated ETKF cycles were rerun with perturbed LBCs. The evolution of the inflation factor can be seen in *Fig. 6* with dashed line, it varies between 6.32 and 18.34. It can be clearly seen, that in this case lower inflation was estimated. The corresponding Talagrand diagrams are shown in *Fig. 8*. In both the inflated and un-inflated cases, the middle ranks are much more populated compared to the previous test. This indicates that the perturbation of the LBCs increases the

ensemble spread in a larger extent than the applied inflation itself. However, it is to be noticed that the Talagrand diagram still shows a U-shape profile, which means that the ensemble does not reflect the true state in spite of the perturbed LBC. This finding suggests that the LBCs are not the only factors in forecast uncertainties and most probably there is still room for improvement in the construction of the initial conditions in order to have a better spread of the forecast ensemble.

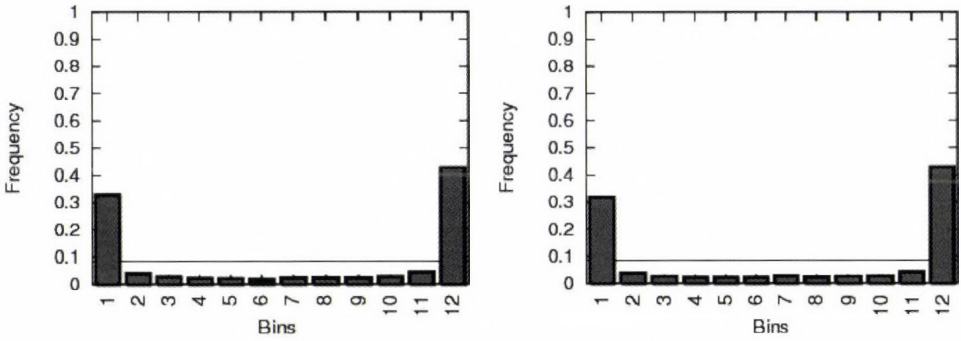

Fig. 8. Talagrand diagrams for forecast ensembles created with perturbed LBCs for the period 00 UTC, September 3 to 18 UTC, September 9, 2008 for 925hPa geopotential. The ensembles were generated without inflation (left) and with inflation (right).

5. Summary and discussion

The primary objective of the application of the Ensemble Transform Kalman Filter (ETKF) method at the Hungarian Meteorological Service is to compute flow-dependent background errors for the operational ALADIN 3d-var data assimilation system. Hence, the implementation was embedded into the operational version of the ALADIN model in Hungary. Yet, the present paper concentrates on the preliminary testing of the ETKF algorithm and performs the first, basic validations of the system. Consequently, the computation of the time-dependent background errors was left aside and the transformation matrix (as heart of the ETKF algorithm) and inflation technique were tested.

As regards the transformation matrix it was found, that the ETKF transformation technique produces analysis perturbations with a reasonable spatial structure as compared to the perturbations created by 3d-var data assimilations. The analysis ensembles generated in two different ways were shown to be similar in terms of correlation. Further tests were carried out to understand the impact of the inflation in an ETKF cycling environment (but still keeping the background errors constant in time). A 7 days period was randomly chosen and the ensemble spread of the background errors was diagnosed with the help of Talagrand diagrams. The Talagrand diagram diagnostics indicated

that the spread of the analysis and forecast ensembles was insufficient in spite of the fact that the inflation slightly improved the characteristics of the forecast ensemble. It was also proven that the perturbed lateral boundary conditions further improved the spread of the ensemble, however, it was still far from being optimal. This latter finding indicates that there is still room for improvements in the initial analyses perturbations with the application of a more optimal inflation factor.

Otherwise, the insufficient spread in the ETKF ensemble might have several sources. One reason may be the operational environment that was used in the implementation. The ETKF study made by *Wang* and *Bishop* (2003) showed good results in a simplified experimental setup assuming that the number, quality, and location of observations are similar at all analysis times, while none of these assumptions are met in an operational data assimilation system. The inflation method was derived by assuming that the statistics are not changing significantly from one analysis time to the other, so this inflation strategy needs to be modified in an operational system.

Another potential cause of the small spread of the ETKF implementation is that in the experiments the matrix P_f was not updated using the generated forecast ensemble, although it is assumed in the ETKF theory. This inconsistent setup was due to the fact that an ensemble of size eleven does not provide a sufficient sample to compute a matrix P_f. One possibility would be to increase the ensemble size, however, this would not be feasible in an operational framework with the present available computational resources. Two other options would be to accumulate the ensemble dispersions over several analysis times or to construct a so-called hybrid P_f matrix with a climatological and a flow-dependent component, where the first would come from a long-time accumulation and the latter from the actual analysis time. Both of these solutions would, however, weaken the flow-dependence of P_f. A future challenge will be to find an affordable solution that keeps the dependence of the background errors on the actual weather.

Since the primary goal for the ensemble generation is to provide a sample of forecast differences for the computation of a time-dependent P_f matrix at every assimilation step, one has to think of the proper diagnostics to be used to evaluate the quality of the ETKF ensemble. In this context, the correlation of the background perturbations and the forecast error are planned to be computed, as *Wei* and *Toth* (2003) suggested. It is believed that this will give a better insight into the characteristics of the ensemble forecasts used in the ETKF procedure.

Acknowledgements—The authors are very grateful to all the participants of the ALADIN international project, who contributed to the development of the numerical weather prediction tools (especially the data assimilation configurations of the ALADIN model) for the study. Particularly, the support of *Claude Fischer* is highly appreciated. We are also grateful to the members of the NWP team of the Hungarian Meteorological Service with special mention to *Sándor Kertész*, who laid down the first theoretical and practical basis of ETKF in Hungary. For the EPS verification

issues, the support of *Edit Hágel* and *Máté Mile* was greatly recognized and appreciated. The useful discussions with *Jelena Bojarova* are also particularly acknowledged. Many thanks for the two anonymous reviewers for their useful comments, which helped to improve the quality of the paper. The authors would like to dedicate this paper to the memory of their colleague and friend *Dezső Dévényi*, who had inevitable role in the initiation of numerical weather prediction in general and data assimilation in particular at the Hungarian Meteorological Service.

References

Anderson, J.L., 2001: An Ensemble Adjustment Kalman Filter for Data Assimilation. *Mon Weather Rev 129,* 2884-2903.

Bishop, C.H., Etherton, B.J. and *Majumdar, S.J.*, 2001: Adaptive sampling with the Ensemble Kalman Transform Filter. Part I: Theoretical aspects. *Mon Weather Rev 129,* 420-436.

Bouttier, F. and *Courtier, Ph.*, 1999: Data assimilation concepts and methods. *ECMWF Meteorological Training Course Lecture Series* (http://www.ecmwf.int/newsevents/training/rcourse_notes/-DATA_ASSIMILATION/ASSIM_CONCEPTS/Assim_concepts.html).

Bölöni, G., 2006: Development of a variational data assimilation system for a limited area model at the Hungarian Meteorological Service. *Időjárás 110,* 309-328.

Csomós, P., Bölöni, G., 2008: First steps towards the Ensemble Transform Kalman Filter technique at the Hungarian Meteorological Service. *HIRLAM Newsletter 54,* 9-19.

Desroziers, G., Berre, L., Chapnik, B., and *Poli, P.*, 2005: Diagnosis of observation, background and analysis error statistics in observation space. *Q J Roy Meteor Soc 131,* 3385-3396.

Evensen, G., 2007: *Data Assimilation, The Ensemble Kalman Filter.* Springer-Verlag, Berlin. pp. 37-38.

Hágel, E. and *Mile, M.*, 2009: The limited area ensemble prediction system of the Hungarian Meteorological Service. *ALADIN Newsletter 35.*

Hamill, T.M., 2000: Interpretation of rank histograms for verifying ensemble forecasts. *Mon Weather Rev 129,* 550-560.

Hamill, T.M. and *Snyder, C.*, 2000: A Hybrid Ensemble Kalman Filter-3D variational analysis scheme. *Mon Weather Rev 128*, 2905-2919.

Hamill, T.M. and *Whitaker, J.*, 2005: Accounting for the error due to unresolved scales in ensemble data assimilation: A comparison of different approaches. *Mon Weather Rev 133,* 3132-3147.

Horányi, A., Ihász, I. and *Radnóti, G.*, 1996: A numerical weather prediction model for Central-Europe with the participation of the Hungarian Meteorological Service. *Időjárás 100,* 277-301.

Horányi, A., Kertész, S., Kullmann, L. and *Radnóti, G.*, 2006: The ARPEGE/ALADIN mesoscale numerical modeling system and its application at the Hungarian Meteorological Service. *Időjárás 110,* 203-327.

Houtekamer, P.L. and *Mitchell, H.L.*, 1998: Data assimilation using an ensemble filter technique. *Mon Weather Rev 126,* 796-811.

Houtekamer, P.L. and *Mitchell, H.L.*, 2001: A sequential ensemble Kalman filter for atmospheric data assimilation. *Mon Weather Rev 129,* 123-137.

Johansson, Å., Bojarova, J., Gustafsson, N. and *Vignes, O.*, 2009: ETKF rescaling scheme for HIRLAM: application to ensemble forecasting. *HIRLAM Newsletter 55A, 55-62.*

Kalman, R.E., 1960: A new approach to linear filtering and prediction problems. *ASME Journal of Basic Engineering 82,* 35-45.

Lorenz, E.N., 1963: Deterministic nonperiodic flow. *J Atmos Sci 20,* 130-141.

Majumdar, S.J., Bishop, C.H., Etherton, B.J., Szunyogh, I. and *Toth, Z.*, 2001: Can an ensemble transform Kalman filter predict the reduction in forecast-error variance produced by targeted observations? *Q J Roy Meteor Soc 127,* 2803-2820.

Majumdar, S.J., Bishop, C.H., Etherton, B.J. and *Toth, Z.*, 2002: Adaptive sampling with the Ensemble Transform Kalman Filter. Part II: Field program implementation. *Mon Weather Rev 130,* 1356-1369.

Ott, E., Hunt, B.R., Szunyogh, I., Zimin, A.V., Kostelich, E., Corazza, M., Kalnay, E., Patil, D.J. and *Yorke, J.A.*, 2004: A local Ensemble Kalman Filter for atmospheric data assimilation. *Tellus 56A,* 415-428.

Tippett, M.K., Anderson, J.L., Bishop, C.H., Hamill, T.M. and *Whitaker, J.S.*, 2003: Ensemble square root filters. *Mon Weather Rev 131,* 1485-1490.

Wang, X., Bishop, C.H., 2003: A comparison of breeding and Ensemble Transform Kalman Filter ensemble forecast schemes. *J Atmos Sci 60,* 1140-1158.

Wang, X., Bishop, C.H., Julier, S.J., 2004: Which is better, an ensemble of positive-negative pairs or a centered spherical simplex ensemble? *Mon Weather Rev 132,* 1590-1605.

Wei, M. and *Toth, Z.*, 2003: A new measure of ensemble performance: Perturbations versus Error Correlation Analysis (PECA). *Mon Weather Rev 131,* 1549-1565.

Wei, M., Toth, Z., Wobus, R., Zhu, Y., Bishop, C.H., Wang, X., 2006: Ensemble Transform Kalman Filter-based ensemble perturbations in an operational global prediction system at NCEP. *Tellus 58,* 28-44.

Whitaker, J. and *Hamill, T.M.*, 2002: Ensemble data assimilation without perturbed observations. *Mon Weather Rev 130,* 1913-1924.

IDŐJÁRÁS

Quarterly Journal of the Hungarian Meteorological Service
Vol. 114, No. 1–2, January–June 2010, pp. 39–55

Sensitivity of local convective precipitation to parameterization of the field capacity and wilting point soil moisture contents

Ferenc Ács[1*], **Ákos Horváth**[2], **Hajnalka Breuer**[1], and **Franz Rubel**[3]

[1]*Department of Meteorology, Eötvös Loránd University*
P.O. Box 32, H-1518 Budapest, Hungary
E-mails: acs@caesar.elte.hu, bhajni@nimbus.elte.hu

[2]*Hungarian Meteorological Service*
Vitorlás u. 17, H-8600 Siófok, Hungary; E-mail: horvath.a@met.hu

[3]*WG Biometeorology, Institute of Medical Physics and Biostatistics*
University of Veterinary Medicine Vienna, Austria; E-mail: franz.rubel@vu-wien.ac.at

[*]*Corresponding author*

(Manuscript received in final form December 10, 2009)

Abstract—Sensitivity of local convective precipitation to parameterization of the field capacity (θ_f) and wilting point (θ_w) soil moisture contents was analyzed. The analysis was performed using simulation results of the Penn State – NCAR MM5 Modeling System obtained on nine days in 2006 and 2007. 24-hour accumulated precipitation fields over the territory of Hungary were considered. Precipitation fields were statistically analyzed. The observed fields were obtained from rain gage data applying a kriging interpolation technique. The agreement between simulated and observed fields was estimated using categorical and continuous verification indices. Significance tests were done to estimate how large (important) or small the obtained differences were.

The main results are as follows. In average, 20 percent relative differences in the θ_f resulted in about 5–10 percent relative differences in the true skill statistic (*TSS*) categorical verification index. In several cases these *TSS* differences are significant on the 10% level. Similarly, in average, 50 percent relative differences in the θ_w resulted in about 10–50 percent relative differences in the *TSS*. These *TSS* differences were significant on the 10% level on eight from the nine days.

The results obtained can be useful in quantifying the strength of the soil moisture – precipitation feedback mechanisms.

Key-words: convective precipitation, field capacity, wilting point, MM5 modeling system, Hungary, true skill statistic categorical verification index, significance test

1. Introduction

The impact of biophysical mechanisms on atmospheric processes is revealed by *Charney* (1975). Since then an array of different sensitivity studies was performed to show the type and rate of the land-surface-atmosphere interaction processes (e.g., *Wolker* and *Rowntree*, 1977; *Deardorff*, 1978; *Shukla* and *Mintz*, 1982; *Sud et al.*, 1988; *Xue*, 1997; *Betts*, 2001; *Betts* and *Viterbo*, 2005). Recently, there are serious efforts not only to explain, but also to quantify the strength of the feedback mechanisms. Among these studies, it could be mentioned the numerical experiment performed by *Koster et al.* (2004) for present-day climate conditions and the study of *Seneviratne et al.* (2006) which was performed for near-future climate conditions in Central Europe.

Among feedback mechanisms, the soil moisture – precipitation feedback is one of the most important (e.g., *Yeh et al.*, 1984; *Oglesby* and *Erickson*, 1989; *Beljaars et al.*, 1996). For a complete analysis, all relevant processes have to be considered: processes occuring in the soil (water transport) and in the planetary boundary layer (triggering of convection), as well as the cloud physical (convection and microphysic) processes (*Hurk van den*, and *Blyth*, 2008). It could not be said that any of these processes is more important than the other one; this hierarchy of the processes according to the importance is highly case-dependent. The importance of soil hydraulic processes is well recognized (*Seneviratne et al.*, 2006), but there is no fully comprehensive analysis. An extensive analysis is made by *Guo et al.* (2006). They argued that the effect of soil moisture (θ) on precipitation should be examined in two distinctly separated parts: (1) when soil moisture affects evaporation and (2) when evaporation affects precipitation. According to *Guo et al.* (2006), the model results are highly dependent on the processes related to the first part. This statement is also confirmed by *Ács* (2002, 2003). Therefore, in this study we investigated the soil – convective precipitation relationship.

From the meteorological point of view, among soil features, soil hydraulic properties are the most important. Among them, the field capacity (θ_f) and the wilting point (θ_w) soil moisture contents have a special role. They depend not only on soil type, but also on the parameterization of soil hydraulic functions (soil water retention and soil water conductivity functions) and the criteria applied in their estimation procedure (*Ács*, 2005). At the same time, θ_f and θ_w are relevant for estimating evapotranspiration (*Chen* and *Dudhia*, 2001). One can pose the question whether local convective precipitation – via sensitivity of evapotranspiration – is also sensitive to the parameterization of θ_f and θ_w. To the best of our knowledge, this question is not discussed to date in the scientific community.

The investigation was made by performing a total of nine one-day case studies during a storm season period in Hungary. Simulations were made by the Penn State – NCAR MM5 modeling system (fifth generation mesoscale model).

The results obtained are statistically evaluated and validated with rain gauge measurements.

2. Model description

2.1. General characteristics of the nonhydrostatic model MM5

Numerical simulations were performed by the version 3 of the Penn State – NCAR MM5 (Fifth-generation Mesoscale Model) modeling system (*Dudhia*, 1993). The model applies a terrain-following sigma coordinate system. The predictive variables are: pressure perturbation, the three momentum components, temperature, specific humidity, and the mixing ratio of the different types of hydrometeors (cloud water, cloud ice, rain, snow, and graupel particles). The partial differential equation system is solved by using a relaxation lateral boundary condition and a radiation upper boundary condition. Model runs were performed using horizontal resolution of 6×6 km, and 26 vertical levels.

Scheme of *Grell et al.* (1994) was applied for parameterization of convection based on rate of destabilization or quasi-equilibrium. A simple single-cloud scheme with updraft and downdraft fluxes and compensating motion determining heating/moistening profile was used. Formation of cloud and precipitation elements are simulated with an explicit bulk microphysical scheme (*Reisner et al.*, 1998) with five different types of hydrometeors: cloud water, cloud ice, rain, snow, and graupel particles. Collision coalescence processes between different types of hydrometeors, furthermore, the diffusion of vapor, freezing of liquid elements, and melting of ice particles are simulated. The equation of conservation is not only solved for the mixing ratios of hydrometeors but for the concentration of cloud ice as well.

The planetary boundary layer (PBL) is described by the local mixing PBL scheme based on the work of *Janjic* (1990, 1994). Compared with other non-local or high-order closure schemes, this PBL scheme proved to be more efficient, because it needs less computer capacity.

2.2. Basic characteristics of the OSU LSM

Land-surface processes are simulated by the OSU LSM (Oregon State University Land-Surface Model). The model consists of a multilayer soil model (*Mahrt* and *Pan*, 1984), a single-layer snow model (*Chen* and *Dudhia*, 2001), and a canopy model (*Pan* and *Mahrt*, 1987).

Evapotranspiration of soil-plant system is estimated as the sum of transpiration and evaporation from the soil and the wetted parts of vegetation. Both transpiration and soil evaporation depend on θ_f and θ_w. They are estimated from soil hydraulic functions (soil water retention (Ψ) and conductivity (K) functions) parameterized after *Campbell* (1974) using *Clapp* and *Hornberger's*

(1978) parameter values, and supposing inhomogeneous areal distribution of soil moisture content.

Detailed description of the model can be found in the work of *Chen* and *Dudhia* (2001).

2.3. Parameterization of θ_f and θ_w

θ_f and θ_w depend not only on soil texture but also on many other factors which are relevant in their estimation: for instance, soil type, transpiration, areal distribution of soil moisture content, and parameterization of soil hydraulic functions. Therefore, their values are quite uncertain.

In this study, soil hydraulic functions referring to Hungarian soils were estimated using *Campbell's* (1974) parameterization and *Clapp* and *Hornberger*'s (1978) parameter values. θ_f values were estimated in two steps as in *Chen* and *Dudhia* (2001): in the first one, the so-called homogeneous (areal distribution of soil moisture content is homogeneous) θ_f values (θ_f^h) were calculated according to the following criteria:

$$pF = \log_{10}[\Psi(\theta_f^h)] = 2.3, \tag{1}$$

$$K_S \left(\frac{\theta_f^h}{\theta_S} \right)^{(2b+3)} = 0.5 \text{ mm day}^{-1}, \tag{2}$$

where θ_S is the saturated soil moisture content, K_S is the saturated soil water conductivity, and b is a dimensionless fitting parameter. The pF value and the corresponding θ_f^h value in Eq. (1) were experimentally determined using the method of *Várallyay* (1973). This criterion applied together with the Várallyay method was common for estimating of θ_f^h in Hungary. Eq. (2) is used for USA soils by *Chen* and *Dudhia* (2001). The effect of the inhomogeneous areal distribution of θ is taken into account as follows:

$$\theta_f = \theta_f^{inh} = \frac{\theta_S}{3} + \frac{2}{3} \cdot \theta_f^h, \tag{3}$$

where Eq. (3) implicitly expresses the fact that the slope of transpiration curve obtained for inhomogeneous distribution of θ is considerably smaller than the slope of transpiration curve obtained for homogeneous distribution of θ (*Ács*, 2003).

θ_w values were also estimated in two steps: as above, the so-called homogeneous θ_w values were calculated according to the following criteria:

$$pF = \log_{10}[\Psi(\theta_w^h)] = 4.2, \tag{4}$$

$$\theta_w^h = 5\rho_b hy, \tag{5}$$

where ρ_b is the bulk soil density and hy is the so-called hygroscopic coefficient. hy is determined by exposing a thin soil layer to an atmosphere saturated with water vapor for a period of about a day. As in Eq. (1), the pF value and the corresponding θ_w^h value in Eq. (4) were experimentally determined using the Várallyay method. In most cases, this expression serves for estimating θ_w^h. If there are no $\Psi(\theta)$ measurements, θ_w^h is usually estimated by expressions like Eq. (5) (*Stefanovits et al.*, 1999). Similarly to the former case, the effect of the inhomogeneous areal distribution of θ is taken into account as

$$\theta_w = \theta_w^{inh} = 0.5\theta_w^h. \tag{6}$$

Eq. (6) has the same meaning as Eq. (3). It expresses the fact that the slope of transpiration curve obtained for inhomogeneous distribution of θ is considerably smaller than the slope of transpiration curve obtained for homogeneous distribution of θ (*Ács*, 2003).

3. Data and numerical experiments

The nine days chosen for analysis include: June 27, 2006, August 1, 2006, August 7, 2006, May 5, 2007, May 22, 2007, June 1, 2007, June 2, 2007, August 10, 2007, and August 20, 2007. On all nine days the weather prevailed was favorable for evolution of local convective storms when the land-surface – air interaction is strong.

3.1. Rain gage data

24-hour accumulated precipitation data for Hungary was acquired from the Hungarian Meteorological Service (HMS). Information was created using data of stations whose type and number varied. In two cases only the main, approximately 100 stations' data were used, in the remaining 7 days the non-automatic gage (about 560 stations) data were incorporated if there was a measurement, otherwise the precipitation was taken as 0. To avoid errors from the rounding and calculation of coordinates, only those stations were added that were more than approximately 6 km from the actual measurements. Overall, on all days the Kriging interpolation error was below 0.5% at the gridcells located in Hungary.

3.2. Basic land-surface parameters

In this study, the USGS-25 category land use dataset was used. Vegetation characteristics in the model domain for May, June, and August are as follows: vegetation cover veg (vegetated part of one complete grid cell) changes between 0.5 and 1.0. In the Carpathian Basin, the prevailing vegetation type is type 2, "dryland, cropland, and pasture". The lowest veg values can be found in the case of type 2. Towards mountain regions, the "grassland" type increases. *veg* is estimated on the basis of leaf area index (LAI). Details concerning the specification of vegetation parameters are described in the work of *Chen* and *Dudhia* (2001).

Table 1. Main physical characteristics of the Hungarian soils

Soil texture	No. of samples	Clay fraction (%)	Sand fraction (%)	Silt fraction (%)	ρ_b (g cm^{-3})
Sand	7	3.84	91.61	4.54	1.32
Loamy sand	20	8.03	78.28	13.69	1.09
Sandy loam	32	14.39	60.29	25.33	1.44
Loam	28	25.36	41.18	33.47	1.45
Sandy clay loam	2	28.80	57.80	13.40	1.55
Clay loam	3	41.53	26.53	31.93	1.3
Clay	37	51.21	6.63	42.19	1.49
Heavy clay	24	60.20	5.37	34.43	1.32
Silt loam	181	19.42	23.33	57.26	1.41
Silty clay loam	154	36.87	9.05	54.08	1.46
Silt	6	5.77	8.05	86.18	1.46

Soil hydraulic properties are obtained from a Hungarian soil data set. Dataset comprises soil data from 576 samples collected in Hungary. Beside hydraulic properties, some other important physical characteristics are also measured. Their mean values for ten different soil textural classes are presented in *Table 1*. Soil textural classes are determined according to criteria given by *Filep* and *Ferencz* (1999). Bulk soil density varies from 1.09 g cm^{-3} for loamy sand to 1.55 g cm^{-3} for sandy clay loam soils. Note, that in the Hungarian soil database there are only two samples for sandy clay loam, three samples for clay loam, and six samples for silt. Noteworthy, that there are only three clay loam samples from the clay loam areas which are quite large in Hungary. Dataset does not contain information about the single map units, that is, we do not know how large the area is to which they are representative. Therefore, it is impossible to upscale this data. Soil hydraulic functions were obtained using results of *Nemes* (2003) and *Fodor* and *Rajkai* (2005).

In this study, θ_f and θ_w values were estimated using all equations. Equation combinations are presented and discussed in the section „Experimental design". The obtained θ_f and θ_w values are presented in *Table 2*. All other soil hydraulic

parameters used in this study are presented in *Table 3*. Note that these soil parameter values can slightly differ from the ones given in the work of *Horváth et al.* (2007). This is caused since slightly different soil data sets and estimation procedures were applied. Soil parameter values represent grid point values. Grid cell values were calculated from the grid point values, but no subgrid-scale variability was considered.

Table 2. Field capacity and wilting point soil moisture content values and the corresponding relative differences for different soil textures estimated by different equation combinations

Soil texture	Θ_f ($m^3\ m^{-3}$)			Θ_w ($m^3\ m^{-3}$)		
	Eqs (1), (3)	Eqs (2), (3)	Rel. diff.	Eqs (4), (6)	Eqs (5), (6)	Rel. diff.
Sand	0.325	0.272	0.163	0.029	0.068	1.345
Loamy sand	0.479	0.348	0.273	0.080	0.141	0.763
Sandy loam	0.379	0.288	0.240	0.064	0.045	0.297
Silt loam	0.408	0.316	0.225	0.080	0.043	0.463
Silt	0.437	0.312	0.286	0.069	0.027	0.609
Loam	0.406	0.296	0.271	0.088	0.044	0.500
Sandy clay loam	0.354	0.273	0.229	0.061	0.032	0.475
Silty clay loam	0.435	0.355	0.184	0.119	0.071	0.403
Clay loam	0.479	0.387	0.192	0.139	0.081	0.417
Sandy clay	0.340	0.330	0.029	0.055	0.056	0.018
Silty clay	0.340	0.273	0.197	0.113	0.032	0.717
Clay	0.489	0.406	0.170	0.147	0.132	0.102
Average	**0.406**	**0.321**	**0.205**	**0.087**	**0.064**	**0.509**

Table 3. Hungarian soil hydraulic parameters as used in the OSU LSM. θ_S = saturated soil moisture content, Ψ_S = saturated soil water retention, K_S = saturated water conductivity, b = dimensionless fitting parameter

Soil texture	b	ψ_s (m)	K_s ($m\ s^{-1}$)	Θ_s ($m^3\ m^{-3}$)
Sand	3.02	0.060	3.26E-05	0.507
Loamy sand	3.90	0.126	2.52E-05	0.598
Sandy loam	3.99	0.143	1.14E-05	0.476
Silt loam	4.18	0.182	2.73E-06	0.487
Silt	3.54	0.223	2.00E-06	0.496
Loam	4.20	0.224	4.58E-06	0.468
Sandy clay loam	4.21	0.132	7.98E-06	0.439
Silty clay loam	5.04	0.234	6.20E-07	0.491
Clay loam	4.74	0.207	3.05E-06	0.580
Sandy clay	3.58	0.890	4.58E-06	0.500
Silty clay	4.06	0.324	1.05E-06	0.453
Clay	6.21	0.228	8.00E-07	0.541

In all runs, that areal distribution of soil texture was used which was originally implemented in the MM5. According to this distribution six textural classes are used from the ten textural classes presented in *Table 1*. They are as follows: loamy sand, sandy loam, loam, sandy clay loam, clay loam and clay.

3.3. Initializations

Initial conditions for MM5 model runs were obtained from the ECMWF analysis and forecast. 00 UTC data were used for all nine days. 100 hPa layer was chosen for the top level of the MM5. Initial soil data (temperature and soil moisture) were also taken from the ECMWF analysis. According to soil moisture content values (about 180–300 mm m^{-3}) in the surface layer, on all nine days $\theta_w < \theta < \theta_f$.

3.4. Experimental design

In the comparative analyses, three runs were performed. The conditions used in the runs are presented in *Table 4*. Run 1 is the reference run. In this run, θ_f was parameterized using Eqs. (1) and (3), while θ_w by Eqs. (4) and (6). Run 2 differs from run 1 only in the parameterization of θ_f. In run 2, θ_f was parameterized using Eqs. (2) and (3). Run 3 and run 1 are different only in the parameterization of θ_w. In run 3, θ_w was parameterized by Eqs. (5) and (6). Comparing the results of runs 1 and 2 (comparison 1), we can analyze how important the parameterization of θ_f is. Comparing the results of runs 1 and 3 (comparison 2), we get an insight into how important the parameterization of θ_w is.

Table 4. Brief description of the conditions in the runs used in the study

	Definition of Θ_f	**Definition of Θ_w**
Run 1	Eqs. (1), (3)	Eqs. (4), (6)
Run 2	Eqs. (2), (3)	Eqs. (4), (6)
Run 3	Eqs. (1), (3)	Eqs. (5), (6)

4. Validation, comparison, and discussion

Storm events occurring on all nine days were analyzed. The model was running for 30 hours to ensure a 6-hour spin-up time. In all cases, the model was started at 00 UTC. 24-hour accumulated precipitation fields were obtained from +6 and +30 hours accumulated precipitation fields. The domain considered has 115 × 49 grid points (in total 5635 grid points). Precipitation fields were statistically analyzed in detail. Statistical analysis is performed only for the territory of Hungary (area of Hungary: 2288 grid points). First, the simulated and observed

fields were compared. Observed fields were estimated from rain gage data applying the ordinary block kriging interpolation technique. In the second step, the agreement between simulated and observed fields was estimated using a categorical and a continuous verification index. At the end, significance tests were also done to estimate how large (important) or small the obtained differences are.

Kriging interpolation technique was used because this method is an approved method for interpolating precipitation data (*Rubel*, 1996). Among the various categorical verification indices, true skill statistics (*TSS*) was chosen. It is based on the two dimensional contingency table (*Table 5*). *TSS* is computed as

$$TSS = \frac{hz - fm}{(h+m)(f+z)}. \tag{7}$$

TSS changes between –1 and +1. For perfect simulation, it tends towards +1. This is a perfect verification measure, because it is independent from the fraction of rain/no rain events. Root mean square error (*RMSE*) was chosen as the continuous verification index. Significance tests were made by using the Student t-test hypothesis. This is appropriate for independent, small-number samples with Gaussian distribution. In the following, we will be dealing with the validation and sensitivity experiments.

Table 5. Contigency table for the calculation of true skill statistics. Symbols: h = hits, f = false, m = misses, z = zero, n = h + f + m + z

	Observation YES	**Observation NO**	**Forecast TOTAL**
Forecast YES	h	f	h + f
Forecast NO	m	z	m + z
Observation TOTAL	h + m	f + z	n

4.1. Validation results

Distribution of the nine-day mean values of the true skill statistics obtained by run 1 (reference run) for different precipitation threshold limits is presented in *Fig. 1a*. Threshold limits denote precipitation intervals from the threshold to its maximum value. Three ranges can be separated. For small threshold limits (small and large precipitation together), the *TSS* values are quite low, about 0.2. For large threshold limits (referring to large precipitation events), the *TSS* values obtained are also small, between 0.05 and 0.2. The distinct break in the values of *TSS* at 13 mm·day^{-1} is caused by the dropout of one day, since there were no precipitation over that threshold. In between (from about 5 to 12 mm day^{-1}), the

TSS values estimated are somewhat larger, about 0.3. The same distribution but obtained on May 5, 2007 is presented in *Fig. 1b*. The main difference with respect to *Fig. 1a* can be observed for small threshold limits. In this case, the *TSS* values are larger, somewhere between 0.4 and 0.7. Note, that abrupt decrease from threshold limit of 13 mm day^{-1} does not exist. Distribution of the nine-day average values of the root mean square errors (*RMSE*) obtained using the reference run for different precipitation threshold limits is presented in *Fig. 2a*. *RMSE* values are smaller (about 10 mm day^{-1}) for larger and larger (about 11–12 mm day^{-1}) for smaller *TSS* values. The same behaviour can also be observed for *RMSE* values calculated on May 5, 2007. This is presented in *Fig. 2b*. In this case, the largest *RMSE* values are about 14 mm day^{-1}.

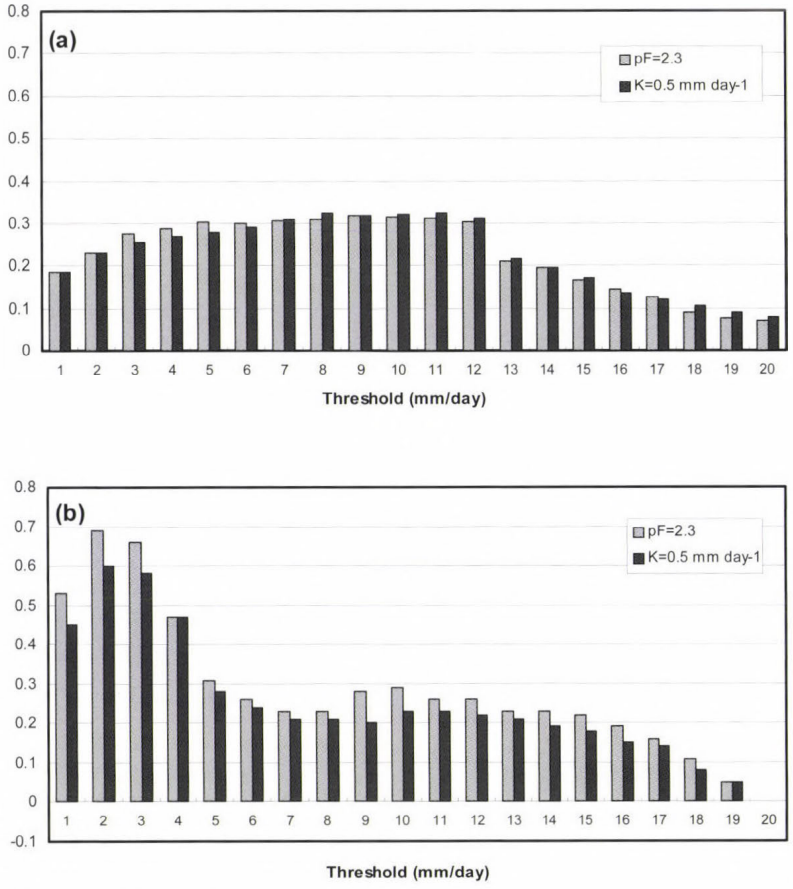

Fig. 1. Distribution of (a) nine-day mean values and (b) actual values on May 5, 2007 of the true skill statistics obtained using run 1 ($pF(\theta_f)$ = 2.3 and $pF(\theta_w)$ = 4.2) and run 2 ($K(\theta_f)$ = 0.5 mm day^{-1} and $pF(\theta_w)$ = 4.2) for different precipitation threshold limits.

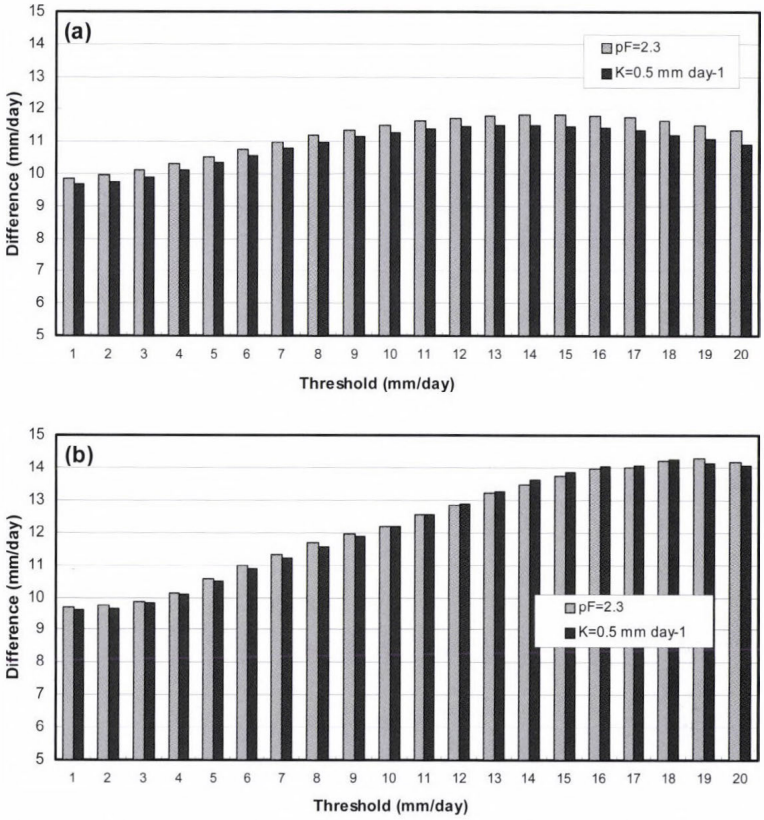

Fig. 2. Distribution of the of (a) nine-day mean values and (b) actual values on May 5, 2007 of the root mean square error obtained using run 1 ($pF(\theta_f) = 2.3$ and $pF(\theta_w) = 4.2$) and run 2 ($K(\theta_f) = 0.5$ mm day^{-1} and $pF(\theta_w) = 4.2$) for different precipitation threshold limits.

4.2. Sensitivity to θ_f parameterization

Comparing results of runs 1 and 2 (comparison 1), we can analyze the effect of θ_f parameterization upon precipitation field prediction. This is presented in *Fig. 1* for *TSS* and in *Fig. 2* for *RMSE* values. According to *Fig. 1*, the sensitivity (difference between the gray and dark columns) seems to be negligible. In average, the relative differences ($[TSS^{pF}–TSS^{K}]/TSS^{pF}$) are under 10 percent. However, according to significance test results, the obtained differences were significant on the 10% level on six from the nine days. That is, relative differences which seem to be small, can be significant. It is also obvious that there is no tendency in the distribution of the *TSS* values obtained by using runs 1 and 2. TSS^{pF} values were higher than TSS^{K} values on three from the six significant days. The sensitivity on a day, when the differences were significant

on the 10% level is presented in *Fig. 1b*. In some cases, for instance for threshold values of 9 and 10 mm day^{-1}, relative difference between the *TSS* values is about 20 percent. Though, it is obvious that these cases are rare. The sensitivity of *RMSE* to θ_f parameterization seems to be also small. In these cases no significance tests were performed.

4.3. Sensitivity to θ_w parameterization

Comparing results of runs 1 and 3 (comparison 2), we can analyze the effect of θ_w parameterization upon precipitation field prediction. Distribution of the nine-day mean values of the true skill statistics obtained using runs 1 and 3 for different precipitation threshold limits is presented in *Fig. 3a*.

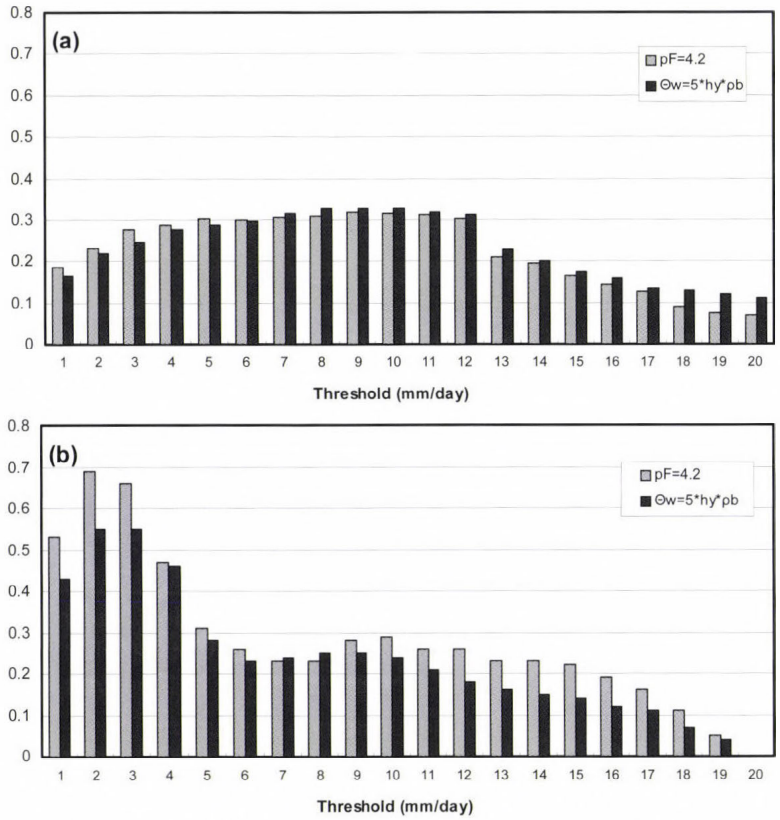

Fig. 3. Distribution of (a) nine-day mean values and (b) actual values on May 5, 2007 of the true skill statistics obtained using run 1 ($pF(\theta_f)$ = 2.3 and $pF(\theta_w)$ = 4.2) and run 3 ($pF(\theta_f)$ = 2.3 and θ_w estimated by *hy*) for different precipitation threshold limits.

As in the former case, the obtained relative differences ($[TSS^{pF}-TSS^{K}]/TSS^{pF}$) seem to be small (under or about 10 percent), but in some cases they were

especially large. For instance, for large threshold values (above 17 mm day^{-1}), relative differences amount 50 percent. According to significance test results, the obtained differences were significant on the 10% level on eight from the nine days, that is, on almost all days. TSS^{hy} values were higher than TSS^{pF} values on five from the eight significant days. The same distribution but obtained on May 5, 2007, when the differences between the *TSS* values were significant, is presented in *Fig. 3b*. In this case, there are large relative differences not only for large (about 30 percent) but also for small threshold values (about 15 percent). Distribution of the nine-day mean values of the *RMSE* for different precipitation threshold limits is presented in *Fig. 4a*. The obtained differences are very small. Distribution of the *RMSE* on May 5, 2007 is presented in *Fig. 4b*. Differences obtained in this case are obviously larger with respect to the differences obtained in *Fig. 4a*. As in the former case, these differences were not analyzed from the point of view of significance tests.

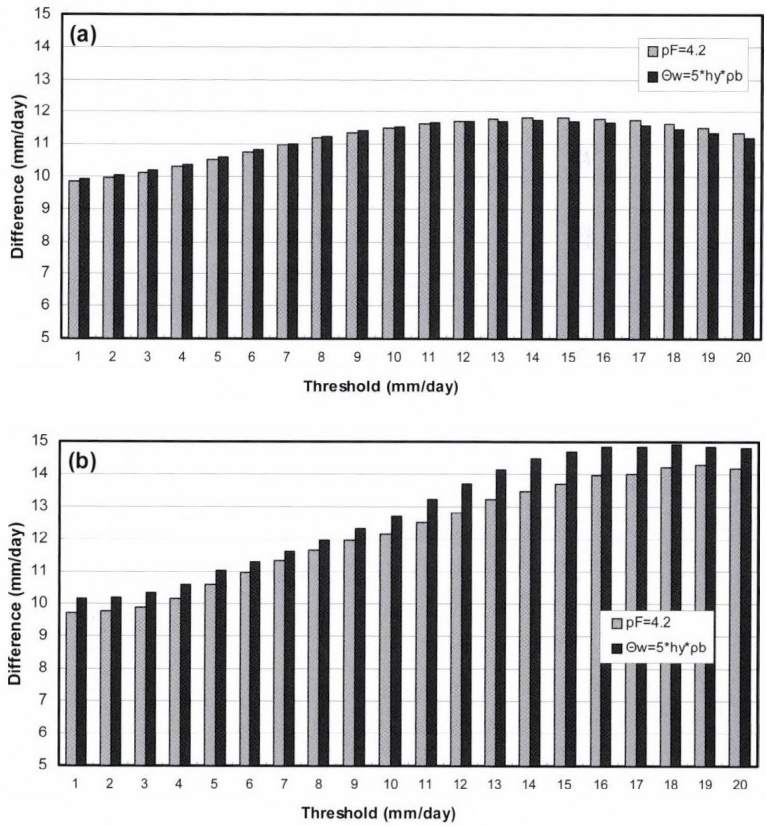

Fig. 4. Distribution of (a) nine-day mean values and (b) actual values on May 5, 2007 of the the root mean square error obtained using run 1 ($pF(\theta_f) = 2.3$ and $pF(\theta_w) = 4.2$) and run 3 ($pF(\theta_f) = 2.3$ and θ_w estimated by *hy*) for different precipitation threshold limits.

4.4. Significance tests applied to other skill measures

Since *TSS* differences were significant on the level of 10% in many cases (for θ_f in six, while for θ_w in eight from the nine days), we decided to performe significance tests for various skill measures. Differences on the level of 10 percent were evaluated for each day separately for in total nine skill measures. The skill measure used were as follows: *POD* = probability of detection ($POD = h/(h + m)$), *FAR* = false alarm ratio ($FAR = f/(h + f)$), *TSS* = true skill statistics, *PC* = proportion of correct hits and misses ($PC = (h + z)/n$), *CSI* = critical success index ($CSI = h/(h + f + m)$), *ORSS* = odds ratio skill score ($ORSS = (hz - fm)/(hz + fm)$), $CHI = \chi 2$-measures of association ($CHI = (hz - fm)^2/((h + f)(m + z)(h + m)(f + z))$, *CR* = correspondence ratio, and *HSS* = Heidke skill score ($HSS = 2(hz - fm)/((h + m)\cdot(m + z) + (h + f)\cdot(f + z))$.

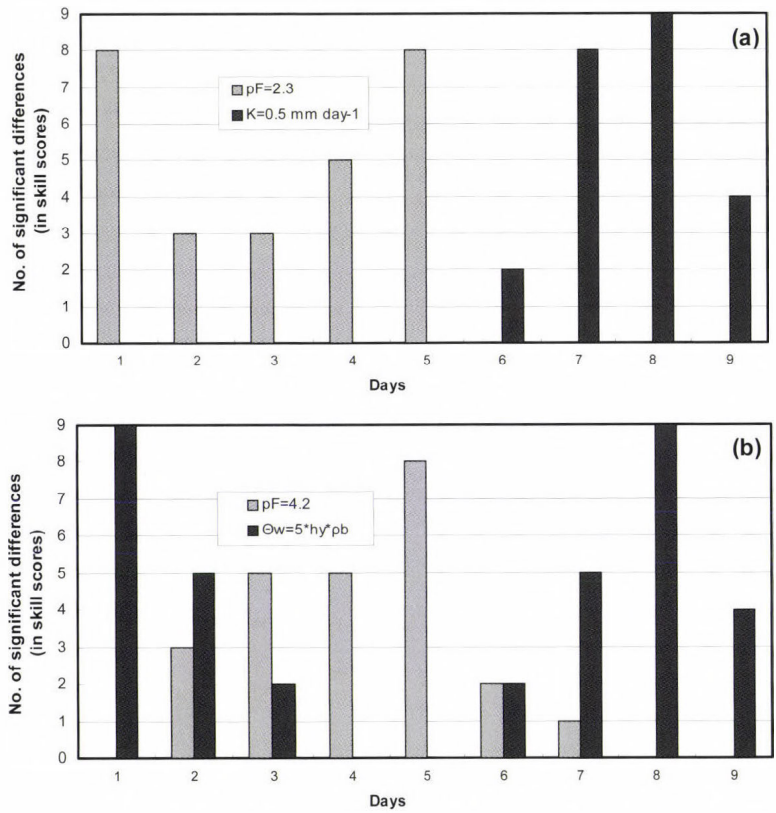

Fig. 5. Number of significant differences on the level of 10% between the skill scores (in total nine) obtained by using conditions (a) in run 1 and run 2 and (b) in run 1 and run 3 for each day separately. Grey column: simulated precipitation obtained by run 1 is closer to the observation, dark column: simulated precipitation obtained by run 2 is closer to the observation.

Number of significant cases for each day separately obtained analyzing the effect of the parameterization of θ_f is presented in *Fig. 5a*. All cases were significant on the eight day (this is August 10, 2007). In all nine cases, results obtained in run 2 were better with respect to the results obtained in run 1. On the first, fifth, and seventh days, the differences were in eight cases significant. Nevertheless, on the 1st and 5th days, the results obtained in run 1 were better than those obtained in run 2. Note that on the sixth day, the differences were only in two cases significant. The same distribution but for θ_w is presented in *Fig. 5b*. The number of significant differences is obviously higher than in the former θ_f case. Differences between all skill measures were significant on the first and the eighth days. The lowest number of the significant differences (in total four) can be observed on the 6th and 9th days. There is no tendency in the distribution of the number of significant cases obtained by using runs 1 and 3.

5. Conclusions

The impact of θ_f and θ_w parameterization upon convective precipitation fields was analyzed. The analysis was performed using simulation results of the Penn State – NCAR MM5 Modeling System obtained on nine days in 2006 and 2007. On all days, actual soil moisture content in the surface layer was higher than θ_w but lower than θ_f.

The considered domain covers the territory of Hungary. Convective precipitation fields were statistically analyzed in detail. First, the simulated and observed fields were compared. The observed fields were obtained from rain gage data applying a kriging interpolation technique. Agreement between the simulated and observed fields was estimated using categorical and continuous verification indices. Significance tests were done to estimate how large (important) or small the obtained differences are.

According to the results, MM5 simulates in an acceptable manner the formation of local convective precipitation field in Hungary. *TSS* values obtained are about 0.2–0.3 on average. We also showed that local convective precipitation is to some degree sensitive to the parameterizations of θ_f and θ_w. What does "to some degree" mean? It can be seen that on average, 20 percent relative differences in the θ_f ($[\theta_f^{pF} - \theta_f^{K}]/\theta_f^{pF}$) (see *Table 2*) caused on average about 5–10% relative differences in the *TSS* ($[TSS^{pF}–TSS^{K}]/TSS^{pF}$). However, in many cases these *TSS* differences were significant on the level of 10%. Similarly, on average, 50 percent relative differences in the θ_w ($[\theta_w^{pF} - \theta_f^{hy}]/\theta_f^{pF}$) (see *Table 2*) caused about 10–50 percent relative differences in the *TSS* ($[TSS^{pF}–TSS^{hy}]/TSS^{pF}$). These *TSS* differences were significant on the level of 10% on eight days. This latter result suggests that sensitivity to θ_w seems to be somewhat higher than sensitivity to θ_f.

Results obtained can be useful in quantifying of the strength of the soil moisture – precipitation feedback mechanisms. It should be mentioned that models used for scientific and operative purposes have completely different soil parameterizations, so different θ_f and θ_w calculation procedures. This study showed that uncertainties in the parameterization of θ_f and θ_w could considerably contribute to scatter of the simulation results (*Koster et al.*, 2004).

Acknowledgements—We thank the help of *K. Rajkai* who gave many remarkable suggestions related to soil physical aspects. The study is financially supported by the National Program for Research and Development (project number NKFP3-00022/2005).

References

Ács, F., 2002: On the relationship between transpiration and soil texture. *Időjárás 106*, 277-290.

Ács, F., 2003: On the relationship between the spatial variability of soil properties and transpiration. *Időjárás 107*, 257-272.

Ács, F., 2005: On transpiration and soil moisture content sensitivity to soil hydrophysical data. *Bound-Lay Meteorol 115*, 473-497.

Beljaars, A.C.M., Viterbo, P., Miller, M.J. and *Betts, A.K.*, 1996: The anomalous rainfall over the United States during July 1993: Sensitivity to land surface parameterization and soil-moisture anomalies. *Mon Weather Rev 124*, 362-383.

Betts, A.K., 2001: Biogeophysical impacts of land use on present-day climate near-surface temperature change and radiating forcing. *Atmos Sci Lett 2*, 39-51.

Betts, A.K. and *Viterbo, P.*, 2005: Land-surface, boundary layer, and cloud-field coupling over the south-western Amazon in ERA-40. *J Geophys Res.110*, p D14108, doi:10.1029/2004JD005702.

Campbell, G.S., 1974: A simple method for determining unsaturated conductivity from moisture retention data. *Soil Sci 117*, 311-314.

Charney, J.G., Stone P.H. and *Quirk, J.W.*, 1975: Drought in the Sahara: A biophysical feedback mechanism. *Science 187*, 434-435.

Chen, F. and *Dudhia, J.*, 2001: Coupling an advanced land surface-hydrology model with the Penn State – NCAR MM5 Modeling System. Part I: Model implementation and sensitivity. *Mon Weather Rev 129*, 569-585.

Clapp, R.B. and *Hornberger, G.M.*, 1978: Empirical equations for some hydraulic properties. *Water Resour Res 14*, 601-604.

Deardorff, J., 1978: Efficient prediction of ground surface temperature and moisture with inclusion of a layer of vegetation. *J Geophys Res 83*, 1889-1903.

Dudhia, J., 1993: A non-hydrostatic version of the Penn State-NCAR Mesoscale Model: Validation tests and simulation of an Atlantic cyclone and cold front. *Mon Weather Rev 121*, 1493-1513.

Filep, Gy. and *Ferencz, G.*, 1999: Recommendation for improving the accuracy of soil classification on the basis of particle composition (in Hungarian). *Agrokem Talajtan 48*, 305-317.

Fodor, N. and *Rajkai, K.*, 2005: Estimation of physical soil properties and their use in models (in Hungarian). *Agrokem Talajtan 54*, 25-40.

Grell, G., Dudhia, J. and *Stauffer, D.*, 1994: A description of the fifth generation Penn State/NCAR Mesoscale Model. *NCAR Tech. Note NCAR/TN-398+STR*, 117 pp.

Guo, Y., Dirmeyer, P.A., Koster, R.D., Sud, Y.C., Bonan, G., Oleson, K.W., Chan, E., Verseghy, D., Cox, P., Gordon, C.T., McGregor, J.L., Kanae, S., Kowalczyk, E., Lawrence, D., Liu, P., Mitchell, K., Malyshev, S., McAwaney, B., Oki, T., Yamada, T., Pitman, A., Taylor, C.M., Vasic, R. and *Xue, Y.*, 2006: GLACE: The global land-atmosphere coupling experiment. Part II: Analysis. *J Hydrometeor 7*, 611-625.

Horváth, Á., Ács, F., and *Geresdi, I.*, 2007: Sensitivity of severe convective storms to soil hydrophysical characteristics: A case study for April 18, 2005. *Időjárás 111*, 221-237.

Hurk, B.J. van den and *Blyth, E.*, 2008: WATCH/LoCo Workshop. *GEWEX NEWS 18*, 12-14.

Janjic, Z.J., 1990: The step-mountain coordinate–physical package. *Mon Weather Rev 118,* 1429-1443.

Janjic, Z.J., 1994: The step-mountain Eta coordinate model. Further developments of the convection, viscous sublayer and turbulent closure schemes. *Mon Weather Rev 112*, 927-945.

Mahrt, L. and *Pan, H.L.*, 1984: A two-layer model of soil hydrology. *Bound-Lay Meteorol 29*, 1-20.

Nemes, A., 2003: Multi-scale hydraulic pedotransfer functions for Hungarian soils. *Ph. D. Dissertation, Wageningen University*, ISBN 90-5808-804-9 143 pp.

Koster, D.R., Dirmeyer, P.A., Guo, Z., Bonan, G., Chan, E., Cox, P., Gordon, C.T., Kanae, S., Kowalczyk, A., Lawrence, D., Liu, P., Lu, C-H., Malyshev, S., McAveney, B., Mitchell, K., Mocko, D., Oki, T., Oleson, K., Pitman, A., Sud, Y.C., Taylor, C.M., Versegy, D., Vasic, R., Xue, Y., and Yamada, T., 2004: Regions of strong coupling between soil moisture and precipitation. *Science 305*, 1138-1140.

Oglesby, R.J. and *Ericson, D.J.*, 1989: Soil moisture and the persistence of North American drought. *J Climate 2*, 1362-1380.

Pan, H.L. and *Mahrt, L.*, 1987: Interaction between soil hydrology and boundary-layer developement. *Bound-Lay Meteorol 38*, 185-202.

Reisner, J., Rasmussen, R.M. and *Bruintjes, R.T.*, 1998: Explicit forecasting of supercooled liquid water in winter storms using the MM5 mesoscale model. *Q J Roy Meteor Soc 124*, 1071-1107.

Rubel, F., 1996: PIDCAP-Quick look precipitation atlas. *Österreichische Beitraege zu Meteorologie und Geophysik 15*, 97 pp.

Shukla, J. and *Mintz, Y.*, 1982: Influence of land-surface evapotranspiration on the earth's climate. *Science 215*, 1498-1501.

Seneviratne, S.I., Lüthi D., Litschi, M. and *Schär, C.*, 2006: Land-atmosphere coupling and climate change in Europa. *Nature 443*, 205-209.

Seneviratne, S.I., Koster, R.D., Guo, Z., Dirmeyer, P.A., Kowalczyk, E., Lawrence, D., Liu, P., Lu, C-H., Mocko, D., Oleson, K.W., Verseghy, D., 2006: Soil moisture memory in AGCM simulations: Analysis of Global Land-Atmosphere Coupling Experiment (GLACE) data. *J Hydrometeorology 7*, 1090-1112.

Stefanovits, P., Filep, Gy., Füleky, Gy., 1999: Soil science (in Hungarian), revised 4th edition. *Mezőgazda*, Budapest, pp. 472.

Sud, Y.C., Shukla, J. and *Mintz, Y.*, 1988: Influence of land-surface roughness on atmospheric circulation and rainfall: a sensitivity study with a general circulation model. *J Appl Meteorol 27*, 1036–1054.

Várallyay, Gy., 1973: Soil moisture potential and new apparatus for the determination of moisture retention curves in the low suction range (0-1 atmospheres). *Agrokem Talajtan 22*, 1-22.

Wolker, J. and *Rowntree, J.R.*, 1977: The effect of soil moisture on circulation and rainfall in a tropical model. *Q J Roy Meteorol Soc 103*, 29-46.

Xue, Y., 1997: Biosphere feedback on regional climate in tropical north Africa. *Q J Roy Meteorol Soc 123*, 1483-1515.

Yeh, T.-C., Wetherald, T. and *Manabe, S.*, 1984: The effect of soil moisture on the short-term climate and hydrology change – A numerical experiment. *Mon Weather Rev 112*, 474-490.

IDŐJÁRÁS

Quarterly Journal of the Hungarian Meteorological Service
Vol. 114, No. 1–2, January–June 2010, pp. 57–77

Validation of the dynamically adapted high-resolution wind forecasts for the wind power stations in Hungary

Gabriella Szépszó* and **András Horányi**

Hungarian Meteorological Service
P.O. Box 38, H-1525 Budapest, Hungary
E-mails: szepszo.g@met.hu; horanyi.a@met.hu

**Corresponding author*

(Manuscript received in final form March 15, 2010)

Abstract—In the recent years, the interest has been increasing regarding the more and more precise prediction of the low-level atmospheric wind characteristics over Hungary. At the Hungarian Meteorological Service this challenge had been completed with the application of the high-resolution dynamical adaptation originally developed in the framework of the ALADIN cooperation in the late 90s. The dynamical downscaling of the coarser wind fields is realized with the ALADIN meso-scale numerical weather prediction model by a half-hour model integration on 5 km horizontal and 15-level vertical resolution with simplified physical parameterization package. It is shown that this dynamical adaptation step improves the original 10-meter wind forecasts obtained with the 8 km operational version of the ALADIN model. The performance of the method was intensively verified with respect to the local observational data at 80 meters for a wind power station situated at the northwestern part of Hungary. The validation results indicate that the dynamically post-processed forecasts do not have systematic errors, however, the diurnal wind cycle is not properly simulated. In the seven-month evaluation period the low and high wind speeds are overrepresented, whereas the occurrences of intermediate velocities are underestimated. The results are rather satisfactory for the investigated location, however, ideas are also presented for further improvements of the wind predictions.

Key-words: numerical weather prediction, ALADIN limited area meso-scale model, dynamical adaptation, low-level wind, verification

1. Introduction

Precise wind forecasts for the near-surface are crucial for the wind power stations, since they are obliged to make a priori estimation of their daily energy production. For this purpose the only solution is provided by the application of

short-range numerical weather prediction (NWP) models. Nevertheless, the accurate wind information is desired in such detail, which is not ensured by today's typical operational high- (8–10 km) resolution weather predictions. Therefore, the operational forecasts need to be further enhanced by appropriate (dynamical) methods.

Increasing the spatial resolution of the limited area models (LAMs) seems to be a natural and simple way to improve the quality of the predictions. Nevertheless, the horizontal mesh cannot be always excessively refined without reconsideration of the physical parameterization and dynamical core of the NWP models. One obvious and essential change together with the resolution increase is the abandonment of the hydrostatic approximation. The most important phenomena to be more precisely or explicitly described by the non-hydrostatic models are the cloud-, microphysics, and micro-scale processes (e.g., convection), which play key role on the 2–5 km horizontal resolution. The complexity of this kind of models is significantly higher, as besides the vertical velocity their microphysical part is also extended with further prognostic variables associated with the different phases of water. Thanks to these enhancements, not only the precipitation-related processes are better simulated in the non-hydrostatic manner, but also the strong wind events accompanying some of the extreme weather situations.

Today, non-hydrostatic modeling is an area of intensive research and development of numerical weather prediction; however, its computational demands are still too high for its widespread applications. The dynamical adaptation (DADA) procedure (*Žagar* and *Rakovec*, 1999) presents a brilliant (simple and elegant) solution for the more accurate description of the small-scale wind characteristics of the atmosphere. The main advantages of the method are, that it does not require huge efforts on model developments (like for non-hydrostatic models or for the implementation of sophisticated physical parameterization schemes), and additionally, it can be realized with modest computational resources. From the practical point of view, the first step of the DADA method is the interpolation of the coarser-resolution forecast onto a finer-resolution grid (not bringing any new information into the forecast), which is followed by a short model integration on this very high resolution for the adaptation of the large-scale fields to the detailed surface characteristics. This model running takes only 30–45 minutes, while the wind is adapted to the new representation of the orography and possibly to other surface features (*Žagar* and *Rakovec*, 1999). This integration does not use the full, complex numerical model: only those processes are taken into account, which can affect the near-surface wind field and those ones are excluded, which would need more time to develop than the applied 30–45 minutes (for instance, the diabatic processes as cloud water vapor condensation, precipitation formation, or temperature changes due to radiation). The simplification concerns also the vertical levels: since the wind is influenced by the topography mainly in the lower part of the

atmosphere, the number of vertical layers is reduced in the stratosphere and upper troposphere. Further necessary precondition for the success of the method is the capability of the driving model to provide realistic forecasts for the target area, because DADA cannot cure the deficiencies of the original (large-scale) prediction, it only adds some fine-scale details developing due to the more precise surface conditions.

The dynamical adaptation method is a widely used efficient technique to improve the predicted wind field; its positive impacts are anticipated especially over terrains with complex topography (e.g., in mountains or at coastal regions), in case of strong wind events, and when the dynamical forces are determining the flow. Applicability of the dynamical adaptation in the prediction of extreme winds was investigated in the case studies described by *Ivatek-Sahdan* and *Tudor* (2004). They were studying two *bora* events, which usually evolve in winter due to the temperature gradient between the cold continental and mild sea surface at the eastern side of the Adriatic Sea and it is accompanied by strong wind speeds exceeding even 15 m/s in average. The dynamical adaptation procedure was applied on 2 km horizontal resolution for the original NWP products available on an 8 km grid. The "low-resolution" model was capable of predicting the start and end of the extreme events, however, their strengths were underestimated. DADA presented more realistic wind speeds, moreover, it was also shown, that neither the dynamical adaptation with the use of complete physical parameterization set nor the full model forecast on 2 km resolution could outperform it.

Combination of the method with a non-hydrostatic model was explored by *Alexandru* (2004). The 10 km resolution forecast for Romania was dynamically downscaled to 2.5 km, on the one hand, by the non-hydrostatic version of the ALADIN/Romania model, and on the other hand, with its hydrostatic version. The non-hydrostatic downscaling solution was not able to provide additional important details, which would justify its increased computational costs. In another investigation (*Vasiliu*, 2005), a thorough verification of the results produced by the hydrostatic setup was carried out for a 5-month period concentrating on two areas of interest: the Black Sea coast and a mountainous region of Romania. The improvement of the wind fields could be noticed over the mountain region, while at the coastal territory only minor advantages could be detected.

A new scope of the method was presented at the University of Vienna (*Beck et al.,* 2005), at the Hungarian Meteorological Service (HMS) (*Kertész et al.*, 2005), and in Ljubljana (*Žagar et al.*, 2005): dynamical downscaling of the ERA-40 re-analysis data (*Simmons* and *Gibson*, 2000) in order to produce high-resolution wind climatology over the Alpine region, Hungary, and Slovenia, respectively. The fact, that the coarse-resolution re-analysis dataset describes only the large-scale patterns of the flow, justified the relevance of the use of dynamical adaptation. Since the resolution difference between the initial global and the target domains was quite significant (125 km versus 12, 5, and 2.5 km,

respectively), the downscaling was designed in a hierarchical structure with two nested short-range ALADIN model integrations with increasing resolution. In the final step, the special dynamical adaptation configuration of the ALADIN model (i.e., DADA as described above) was applied to reach the desired wind climatology. The results were validated against observations (*Beck* and *Ahrens*, 2006; *Kertész et al.*, 2005; *Žagar et al.*, 2006), and the verification indicated that the dynamical downscaling is able to produce improved and more detailed wind climatology than the initial large-scale data.

In the last decade, the technique is applied at the Hungarian Meteorological Service in order to operationally produce precise wind fields for aviation weather forecasts and in the last few years for the wind power stations to their energy production estimates. From the point of view of the wind energy potential, the northwestern region of Hungary possesses the most advantageous climatological characteristics: this territory lies along the relatively strong and dominant northwesterly flow (*Kertész et al.*, 2005). Some favorable area can be also found over the eastern part of the country, where the northeasterly winds are typical. Until recently, in Hungary the dynamically adapted wind fields could be verified only against 10-meter wind observations, but since the end of 2008, a cooperation has been started with the wind power stations: they continuously provide their measurement data valid at the hub height of the power plant, which make a comprehensive verification of the simulated higher-level wind results possible. The novelty of the utilization of this new source of information is, that the model performance will be known not only on the levels of SYNOP measurements, but also at the heights, where the results are directly used. Therefore, the present study is dedicated to the validation of the dynamical adaptation method applied at HMS for the prediction of the low-level wind fields.

After this introduction, Section 2 describes the most important characteristics of the wind forecasts and observational dataset used as input information for the evaluation, and the employed verification method is also briefly presented. Section 3 is devoted to the thorough analysis of the results obtained by the application of upper-level observational data at Mosonszolnok-Levél. In Section 4, several open issues are addressed and discussed together with those major conclusions, which can be drawn based on the 7-month validation.

2. Methodology

2.1. High-resolution dynamical adaptation of wind forecasts

In the operational practice, the short-range weather forecasts of the Hungarian Meteorological Service are based on the ALADIN meso-scale numerical weather prediction model. ALADIN (*Horányi et al.*, 2006) is a spectral limited area model, where the horizontal meteorological fields are represented by full harmonic functions (2-dimensional Fourier decompositions). In vertical a hybrid

coordinate system is defined (*Simmons* and *Burridge*, 1981): terrain following at the lower model levels and pressure-type for the upper atmosphere. For the vertical equation of motion the model uses the hydrostatic assumption, its prognostic variables are the temperature, horizontal wind components, specific humidity on the model levels, and the surface pressure. Due to the combined semi-implicit and semi-Lagrangian schemes (*Temperton* and *Staniforth*, 1987) applied for the temporal integration, a very high computational efficiency can be realized: for instance, at 8 km horizontal resolution 5-minute integration time step can be used.

Presently, the ALADIN weather forecasts are produced operationally four times a day: at 00, 06, 12, and 18 UTC for 54-, 48-, 48-, and 36-hour periods, respectively. The integration domain covers mainly continental Europe with 8 km horizontal resolution and 49 vertical levels (see *Fig. 1* and *2*). The initial condition for the integration is provided by the 3-dimensional variational data assimilation procedure (*Bölöni*, 2006) developed for the ALADIN model. The time-dependent lateral boundary conditions in 3-hour frequency are ensured by the global NWP model of the European Centre for Medium-Range Weather Forecasts (ECMWF).

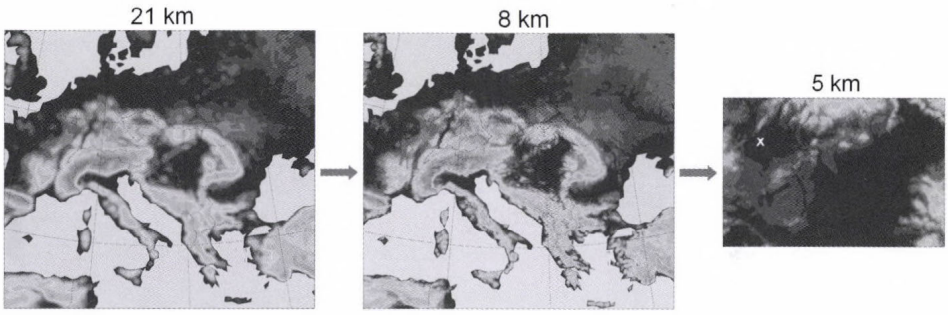

Fig. 1. Orography of the nested model integrations with increasing horizontal resolution: approximately 21 km for the global ECMWF grid (left; in the figure only the selected target integration domain can be seen), 8 km for the operational ALADIN forecast (middle), and 5 km over Hungary for the dynamical adaptation (right). The white "x" on the right represents the selected verification point, Mosonszolnok-Levél.

The raw wind predictions are dynamically refined in the planetary boundary layer, i.e., an additional dynamical adaptation step is performed on the operational model outputs. In practice, the original 8 km resolution information is interpolated onto a 5 km resolution grid (see *Fig. 1*), and the number of vertical layers is reduced in the upper atmosphere resulting in 15 model levels focusing on the planetary boundary layer (see *Fig. 2*). Using these fields as initial and lateral boundary conditions, a simplified model integration lasting 29 minutes (with 60-second time steps) is carried out applying DADA mentioned

in the introduction (*Žagar* and *Rakovec*, 1999). This short dynamical post-processing method adapts the near-surface wind to the more detailed topography taking the "large-scale" forcing from the operational ALADIN model. The final output fields are obtained through vertical interpolation or extrapolation on the desired height coordinates, which are defined at every 10 meters between 10 and 500 m. Vertical post-processing (*Yessad*, 2009) consists of either a linear interpolation for the layers positioned between two model levels or an extrapolation (with the application of logarithmic profile) for heights below the lowest model level (e.g., at 10 meters).

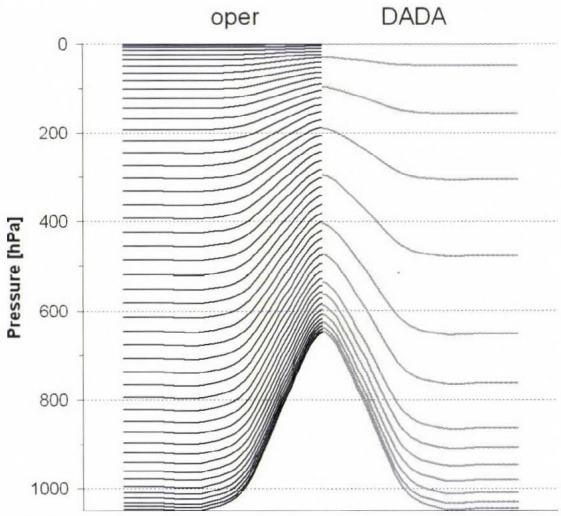

Fig. 2. Hybrid vertical coordinate levels used at the operational forecast ("oper", black curves on the left) and the dynamical adaptation ("DADA", gray curves on the right) with 49 and 15 levels, respectively.

2.2. Input data for the verification

The Hungarian Meteorological Service produces wind information operationally for the wind power plants based on its high-resolution dynamically adapted forecasts starting at 00 UTC and valid for 54 hours. The nearest grid point and height to the given power station is selected as the predicted value, therefore, the 5 km horizontal grid spacing applied at the final dynamical adaptation step allows 3.5 km precision, whereas in vertical the final levels at every 10 meters ensure 5-meter accuracy. The present wind forecast evaluation was carried out for the location of Mosonszolnok-Levél, which is situated in the northwestern part of Hungary at approximately 120-meter height above the sea level (see the white "x" in *Fig. 1*). This power station park stands in a relatively flat area in the gate of the northwesterly flow zone, which is a climatologically favorable

position from the aspect of wind energy production. In this location the wind speed and direction forecasts are provided at the hub-height of the power plants, i.e., at 80 meters above the surface. The forecasts are started from 00 UTC, however, they are used from 9 a.m. (in local time) onwards until 1 a.m. (also local time) of the 3rd forecast day. The output frequency of the forecasted wind data is 15 minutes, and the model data describe the instantaneous wind components of the flow in these time steps. From the observation side, the measurements were available at every 10 minutes for the period of April 19–November 17, 2008. The anemometer is located on an independent tower, at the same height as the hubs of power plants, i.e., in around 78 meters above the surface, and it provides the wind speed as an average over the preceding 10-minute period. It can be read from *Table 1*, that the ALADIN model precisely represents the elevation of the selected point, e.g., its altitude in the model is almost equal with its real height above the sea level.

Table 1. Main characteristics of the input wind datasets: provided wind information, temporal range of the forecasts (LT: in local time), temporal resolution of the produced data, height above the sea level and surface (respectively), and geographical location of the selected point

	Data	**Range**	**Frequency**	**Height**	**Coordinates**
Forecast	Instantaneous wind speed	40 hours from 9 a.m. LT	15 min	125 + 80 m	47.891°N; 17.166°E
Measurement	Mean wind speed (over the last 10 minutes)	-	10 min	124 + 78 m	47.887°N; 17.176°E

Since the data originating from two sources do not correspond to the same type of wind information (i.e., mean and instantaneous values), and moreover, they are available for different time intervals, their direct comparison is not possible. Therefore, the verification was realized on the basis of averages at every half an hour, which were calculated from the wind speed of two time steps in the forecast case and three measurements in the case of observational data. (For instance, for the evaluation at 10:30 UTC, the measurements at 10:10, 10:20, and 10:30 UTC, and the forecasts at 10:15 and 10:30 UTC were respectively averaged, then compared.)

2.3. Verification technique

Evaluation of the wind forecasts for Mosonszolnok-Levél was accomplished for the available seven-month period. On the one hand, the general flavor of the wind predictions during the verification interval is obtained by the unified assessment of all forecast ranges, and on the other hand, the quality of the simulated results is also investigated forecast range by forecast range,

separately. Considering all time steps together, different pairs of forecasts, measurements, and forecast errors are examined in scatter plot diagrams; empirical distribution and density functions were generated on the basis of the simulated and observed data; histograms were also prepared about the forecast errors in function of their signed magnitude. The mean systematic and root mean square (RMS) errors of the forecasts are calculated for all time steps separately and together, as well; the temporal evolution of absolute errors is analyzed for each time step; while the Taylor diagram is used only for selected forecast ranges in every 3 hours. Hereafter, most of the applied verification scores and tools are supposed to be well-known (*Nurmi*, 2003), only the main features of the Taylor diagram are briefly detailed.

The Taylor diagram (*Taylor*, 2001) provides useful information about how well the reference (measured) and the test (simulated) patterns (wind speeds) match each other in terms of their statistical correlation, root mean square (RMS) difference, and ratio of their variances. The geometric relationship between these three statistics allows to plot them into the same diagram. The two (reference and test) samples are represented by two points in the diagram. The radial distances from the origin to each point are proportional to the pattern standard deviation normalized by the observational variance, therefore, the reference point is positioned usually at value 1. The azimuthal position gives the correlation coefficient between the simulated and reference time series. Finally, the distance from the reference point (along concentric circles around it) measures the centered RMS difference between the two fields (as a consequence of the relationship between the three statistics). In the present verification the normalized Taylor diagram was constructed, i.e., the standard deviation of the simulations and the centered RMS difference were standardized with the variance of the observations. The more accurate and consistent the forecast is, the closer its point is positioned to the reference point.

3. Results

First of all, an obvious question is, whether the high- (5 km) resolution dynamical adaptation is able to improve the wind predictions produced on the 8 km operational resolution. For the correct evaluation of this issue, the operational forecasts and the dynamically adapted wind values should be systematically compared at 80-meter height for the 7-month verification period. However, in practice it would mean the necessity of the re-running the ALADIN model for the investigated period. Therefore, it was chosen to study the question by the validation of the 10-meter wind speed values with respect to two nearby observational points (Győr and Mosonmagyaróvár) for an "independent" 3-month period. The 10-meter wind speeds based on the operational 8 km forecasts and the dynamically adapted 5 km ones were assessed in terms of bias and RMS error (*Fig. 3*).

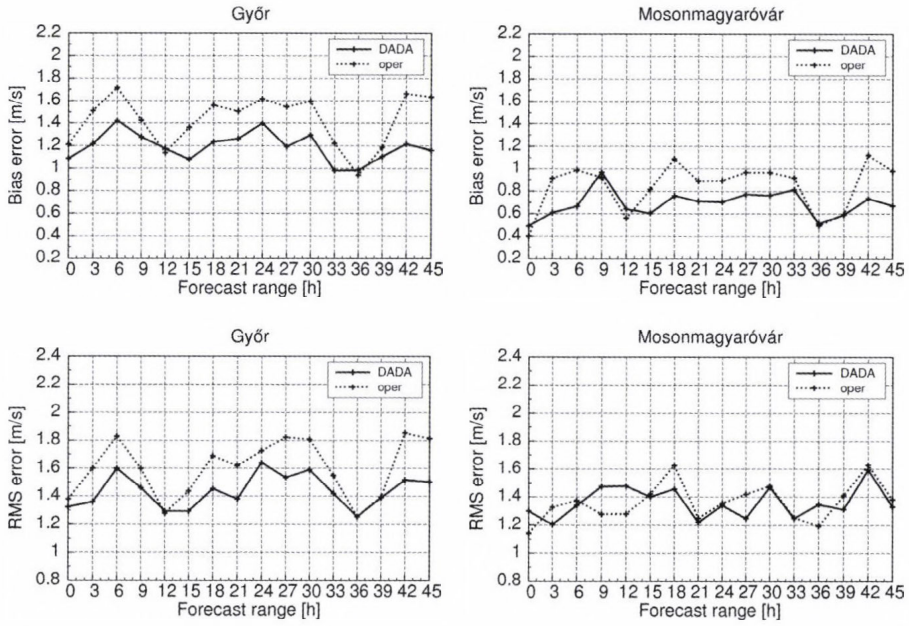

Fig. 3. Mean error (top) and root mean square error (bottom) of the operational ALADIN wind forecasts on 8 km horizontal resolution (dotted curve, "oper") and the 5 km resolution wind forecasts provided by the dynamical adaptation (solid curve, "DADA") for the different time steps (the time steps are considered from the analysis time at 00 UTC) with respect to two SYNOP stations close to Mosonszolnok-Levél: Győr and Mosonmagyaróvár. Verification period: December 1, 2008 – March 1, 2009; level: 10 m.

According to the 3-month verification, it can be generally concluded that the dynamical post-processing procedure improves the wind predictions. The results indicated, that the ALADIN 10-meter wind speed forecasts are hampered by a general overestimation (with 1.4 and 0.8 m/s in average for Győr and Mosonmagyaróvár, respectively), which cannot be fully cured by DADA (the corresponding bias values are 1.2 and 0.7 m/s), since the success of the dynamical adaptation process also depends on the quality of the "large-scale" constraints, which are provided by the 8 km resolution ALADIN forecasts. On the other hand, it is clear that in most time steps DADA outperformed the competing operational forecast in both error characteristics. It is remarked here, that there are some exceptions at the 12h and 36h ranges (i.e., at noon), when the operational results are characterized by identical bias and lower RMS errors than that of the dynamical adaptation (however, the differences between them are rather negligible). These relatively larger reductions in the added value of DADA compared to ALADIN might be associated with the fact, that there are several processes which cannot be more precisely described by this method. Such typical phenomenon is the convection being the most intensive at noon and early

afternoon: since DADA uses only part of the physical parameterization schemes excluding convection, therefore, it has no chance to enhance the results prescribed by the 8 km ALADIN version in cases where these processes have important impact on the wind field. Nevertheless, all this concludes that the application of additional dynamical adaptation on the operational forecasts is useful to provide more accurate 10-meter wind predictions over this territory. Certainly, this conclusion cannot be directly interpreted at higher levels, because the 10-meter wind is an extrapolated diagnosed quantity based on fitting the logarithmic wind profile, whereas the 80-meter wind is rather determined by the dynamics.

Henceforth, the evaluation is concentrating on the 80-meter height, where the wind forecasts and measurements are available for Mosonszolnok-Levél. First, a general overview is given about the main features of the predictions in terms of "lead time independent" indicators, and then the quality is separately investigated in each forecast step. The empirical distribution and density functions (*Figs. 4* and *5*), where the latter ones were constructed by dividing the wind speeds between 0 and 20 m/s into bins of 0.5 m/s for both the model and observational data, provide information about statistical properties of the observed and simulated wind climatologies. (Certainly these are not climatological characteristics in its classical sense, because they are valid only for the investigated period.) It has to be remarked that for the distribution functions the inverse ones are computed (where the relative frequencies of the wind speed occurrences are inverted at the y-axis), since by this visualization the model over- and underestimations, with respect to the observed quantities, can be seen more transparently.

Comparing the histograms and distribution functions for the observations and forecasts, some similarities and also a few differences can be assessed in the simulated and observed wind climatology at the location of Mosonszolnok-Levél:

- Both the measured and forecasted wind speeds cover the range between 0 and 16 m/s.
- The median value (denoted in *Fig. 5*) is similarly around 5 m/s (for the exact values see *Table 2*), i.e., the half of the wind speeds exceeds the 5 m/s threshold in both datasets.
- In the measurements the dominant wind category is between 2.5 and 3 m/s with approximately 7% of relative frequency, in addition, the occurrence of the wind between 2 and 6 m/s exceeds 6% for every bin. The predictions are rather hampered by frequency underestimation between 2 and 7 m/s, which is most characteristic in the 2–3 m/s bins. All this results that the prevailing forecasted wind speeds are in the 5–5.5 m/s category.
- It is also interesting to see the sharp change in the error sign (from occurrence overestimation to underestimation) at the 2 m/s threshold.

(This feature might query the quality of the observations, however, such conclusions are not considered for this short verification period.) The weaker wind speeds below 2 m/s are overrepresented in the simulated results, i.e., the probability of wind speeds from every bin between 0 and 2 m/s is higher in the forecasts than in the reality. Although the level of the overestimation can reach even 80%, the related absolute frequency values are rather small (especially in the category between 0 and 0.5 m/s).

- For the wind speeds above 8 m/s the ALADIN model gives a bit high relative occurrences (though the magnitudes of these errors are even smaller than it was indicated at the lower and intermediate bins).

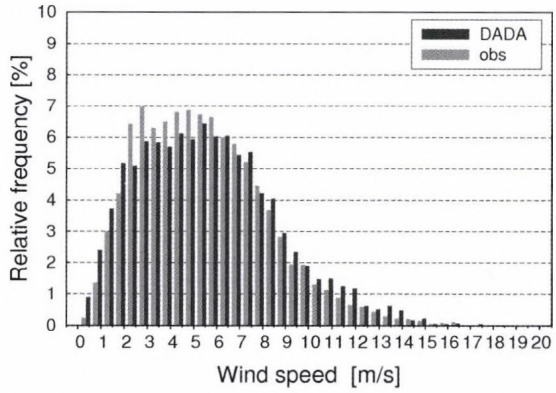

Fig. 4. Discrete density functions of the wind speeds for the model results (black) and the observations (gray). The range of wind speeds are divided into bins of 0.5 m/s. Verification period: April 19–November 17, 2008; location: Mosonszolnok-Levél; height: 80 m.

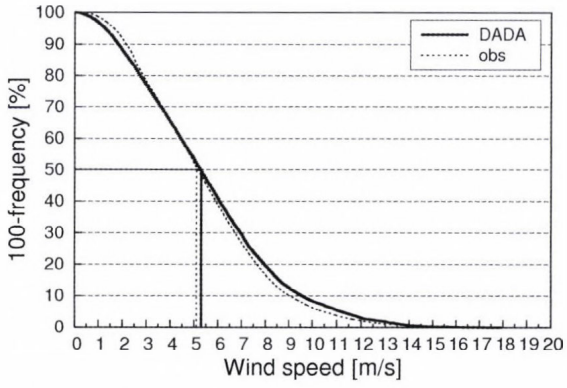

Fig. 5. Inverse empirical distribution functions of the wind speeds for the model results (solid curve) and the observations (dotted curve). Straight lines represent the corresponding median values. Verification period: April 19–November 17, 2008; location: Mosonszolnok-Levél; height: 80 m.

Table 2. Mean forecast errors and wind speed characteristics in the simulated and observed datasets (in m/s)

	DADA	Observation
Mean wind speed	5.5	5.4
Median value	5.3	5.1
Mean bias	0.1	-
Mean RMSE	2.2	-

The conclusions drawn on the basis of the empirical density and distribution functions (i.e., the frequency exaggeration of the lower and higher wind speeds and underestimation in the intermediate wind speed intervals) can be also identified in the scatter plot diagrams with several additional details. Looking at the diagram based on the forecast-observation pairs (first panel of *Fig. 6*), at the first glance it can be noticed that most points are situated rather symmetrically around the diagonal, which indicates that there are no systematic errors. This fact is also proved by the slight 0.1 m/s bias value calculated for the 80-meter level (see *Table 2*), and moreover, comparing it with the values for 10 meters, the performance of DADA is significantly improved with the altitude in terms of bias.

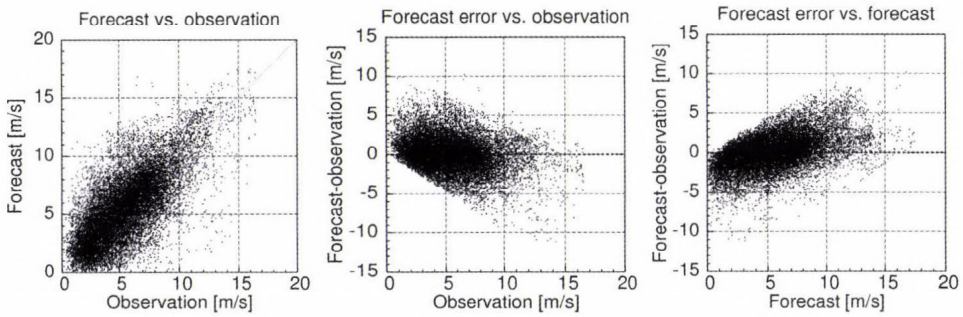

Fig. 6. Scatter plot diagrams (left: forecasts vs. observations, middle: forecast errors vs. observations, right: forecast errors vs. forecasts) for the 5 km resolution wind forecasts provided by the dynamical adaptation procedure. The plots were generated with the use of all time steps. Verification period: April 19–November 17, 2008; location: Mosonszolnok-Levél; height: 80 m.

Nevertheless, with a more careful look, also several asymmetric features can be found in *Fig. 6*. For the higher observed wind speeds (exceeding 10 m/s) the model tends to have underestimation, sometimes even with 5–10 m/s (the size of the error is naturally bounded above by the magnitude of the wind speed). This finding is confirmed by the similar diagram for the forecast errors as function of the observations (middle panel of *Fig. 6*), which additionally

shows that the weaker winds (between 0 and 5 m/s) are simulated too large by ALADIN. At the right panel of *Fig. 6* it is also clearly visible that the simulated wind speeds reaching 10 m/s often exceed the measured values. All this is not in contradiction with the conclusions drawn from the histograms and distribution functions (which do not compose pairs from the simulated and observed values): the model is able to predict stronger winds, though these cases are not always at their real occurrences. In other words: when strong winds happen, the model underestimates them, whereas the weaker observed winds are regularly overestimated.

Investigating the scatter plot diagrams in the different time steps (not shown), it can be concluded that wind speeds above 5 m/s are mainly underestimated by the model at around the 12- and 36-hour forecast ranges (at around noon time), and for the interval of 5 and 10 m/s the overestimation has maximum at the 18- and 42-hour forecast ranges (i.e., in the evenings). Based on these features it can be suspected, that the diurnal cycle of the wind speed is not well represented in the simulated results, e.g., it might be shifted with a few hours. This fact can be analyzed in detail in *Fig. 7*, where the mean observed and simulated wind speeds with respect to the forecast range are displayed. (Forecasts over the 47-hour range are neglected since the sample from these time steps was small due to the change from daylight-saving time to the normal one at the end of October.)

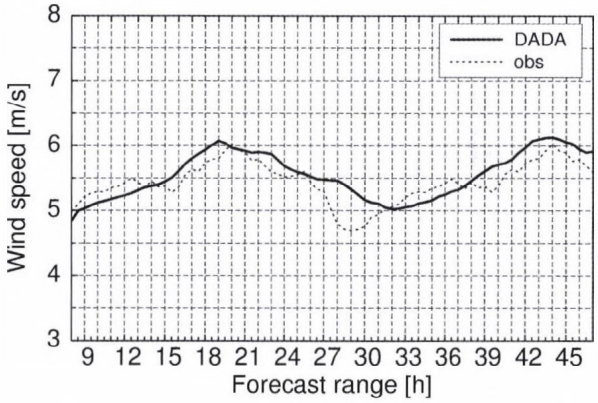

Fig. 7. The simulated (solid curve) and observed (dotted curve) mean wind speed for the different time steps (the time steps are calculated from the analysis time at 00 UTC). Verification period: April 19–November 17, 2008; location: Mosonszolnok-Levél; height: 80 m.

It can be easily seen that the displacement of the simulated values is not constant all along the forecast range. Overestimations occur from the afternoons to the mornings and underestimations from the mornings to the very early afternoons. It implies that the afternoon intensification of the wind speed starts

approximately one hour earlier in the model, therefore, the daily maxima are also reached one hour prior (at 19- and 43-hour forecast ranges instead of 20- and 44-hour ones). After getting the maximum, the wind weakening begins later and this process is slower in the simulations than in the reality resulting in a 3-hour delay of the minimum (at 32 hours forecast instead of its typical real occurrence at 29-hour range). Possible reasons behind the introduced error properties can be the insufficient parameterization of the convective processes as well as the weak description of the atmospheric stratification (however, these two factors are not completely independent from each other). Nevertheless, this hypothesis should be checked in the full ALADIN model at first, since as mentioned, DADA is unable to improve those processes which were insufficiently described by the "host" model. Inevitably, more experimentation would be needed to completely understand the physical background of this deficiency.

According to the systematic errors (*Fig. 8*), it can be seen, that in the wind speed forecasts the overestimation is somewhat more dominant than the underestimation resulting in a small (0.1 m/s) positive error for the complete verification period. This fact is supported by the empirical density function of the signed errors (*Fig. 9*), which indicates an almost symmetric pattern. It can be also seen, that the spectrum of the errors covers the range between –8.5 and 8.5 m/s (though there are only few cases with error exceeding 7 m/s), i.e., the negligible mean systematic error is resulted by the balance between the positive and negative differences, which compensate each other. During the two forecasting days, the main systematic behavior of the predictions depends on the actual time steps (*Fig. 8*): the interval between the 8 and 13 hours at the beginning of the forecast period and between the 32 and 37 hours (i.e., 24 hours later) are characterized by small underestimation. The intermediate periods are mostly exacerbated by overestimation, which reaches its maximum (0.7 m/s) at the 28.5-hour forecast range. Looking at the mean and root mean square differences between the simulated and observed wind speeds, it is remarkable, that the model errors do not grow by the forecast range (excluding the first few hours). In each investigated time step the magnitudes of the mean errors basically do not exceed 0.5 m/s; the only exception is the abovementioned maximum at around 28 hours.

Nevertheless, the fact that the mean systematic error is small does not suggest, that the prediction would have equal accuracy in every forecast range, additionally, the minor bias in given time step does not guarantee the perfect prediction, since the positive and negative errors might compensate each other during a longer period. The mean RMSE value is 2.2 m/s for the entire forecast range (*Table 2*). The temporal evolution of the root mean square differences (*Fig. 8*) reveals that the errors are larger (reaching even 2.5 m/s value) when the overestimation is dominant, whereas the model performance is better in the periods of underestimation (the RMSE value is approximately 1.7 m/s in the

8–12 hours and 32–36 hours ranges). One reason might be behind the lower level of accuracy at the overestimation: since the wind speed is always positive, it can be underestimated only with its magnitude (i.e., the size of the negative errors has upper bound), whereas in the case of overestimation, the errors have basically no bound. The ranges of 9 hours and 33 hours are characterized not only by the smallest RMSE values, but they are also in best correlation (approximately 0.85 according to the Taylor diagram at *Fig. 10*) with the observation time series.

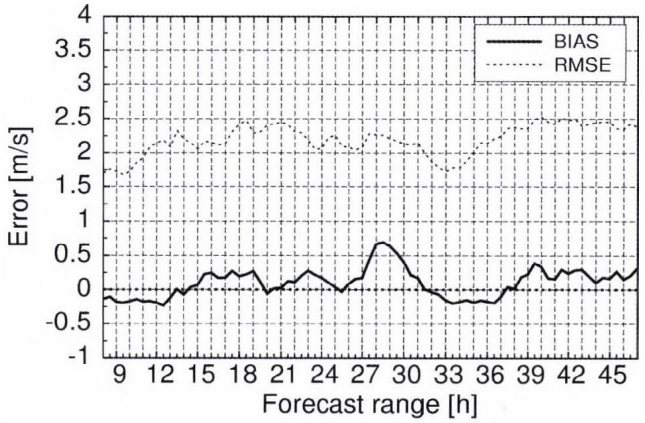

Fig. 8. Mean systematic error (solid curve) and root mean square error (dotted curve) for the different time steps (the time steps are calculated from the analysis time at 00 UTC). Verification period: April 19–November 17, 2008; location: Mosonszolnok-Levél; height: 80 m.

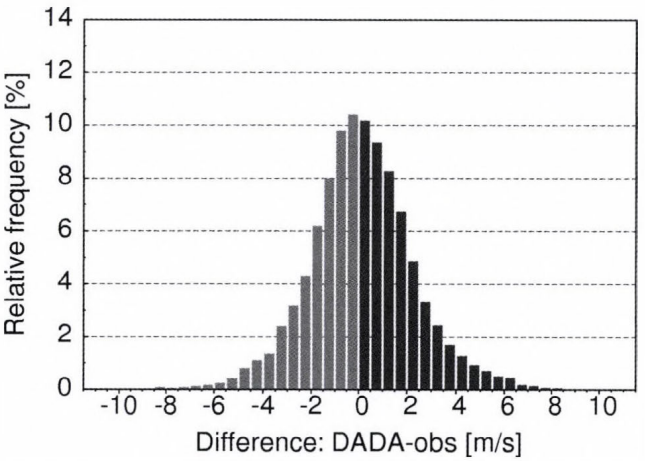

Fig. 9. Discrete density function for the signed model errors. Verification period: April 19–November 17, 2008; location: Mosonszolnok-Levél; height: 80 m.

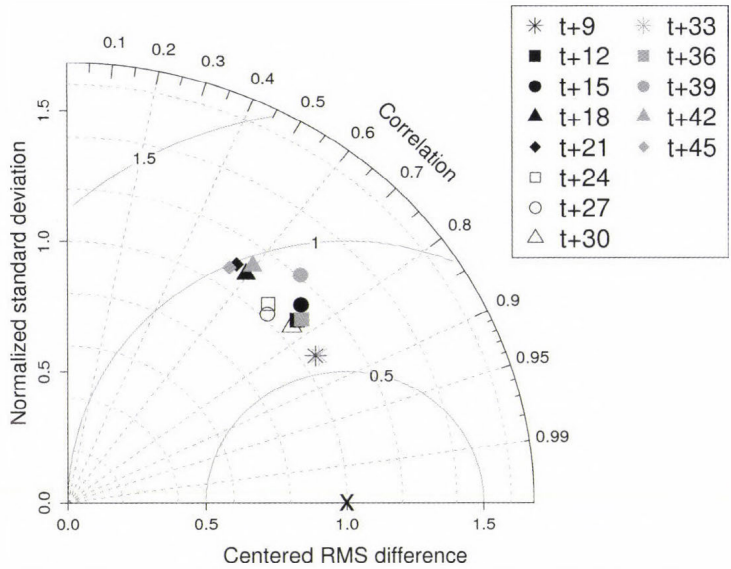

Fig. 10. Normalized Taylor diagram for the model results in different time steps. Verification period: April 19–November 17, 2008; location: Mosonszolnok-Levél; height: 80 m.

The temporal variation of the mean absolute error during the seven-month verification period was also examined for the different forecast ranges (only the 9- and 42-hour time steps are presented in *Fig. 11* as examples for the better and worse predictions). Rather large absolute simulation errors can be found in certain days: the deviations can reach even 6–8 m/s (although these errors occur quite seldom). Nonetheless, according to *Fig. 12* one can say, that the errors are under 1 m/s in around 40% of the cases, and the relative frequency of the errors exceeding 5.5 m/s does not reach 1%. The lowest absolute departures from the observations and the smallest error variability can be identified in the time step of 9 hours (*Fig. 11*), the errors mainly remain under 4 m/s all along the period. There are some forecast ranges when the larger errors are more frequent, for instance, the 42-hour step (right panel of *Fig. 11*) when the RMSE is also relatively high. Such dissimilarity between the 9 and 42 hours cannot be explained by the difference in the forecast ranges (i.e., the longer-range forecast is worse), because as mentioned earlier, the error patterns are rather uniform with respect to the lead time (*Figs. 8* and *10*). A more possible and plausible explanation might be again the imprecise description of the daily cycle in the model, which is also confirmed by the similar error characteristics for the 18-hour forecast range, i.e., in the evening one day before. In the Taylor diagram (*Fig. 10*), the points for the time steps of 18h, 21h, 42h, and 45h are positioned in a small group with somewhat negative properties: the predictions in these steps (i.e., in

the evenings) are correlated in a weakest way with the observational time series accompanied by around 0.55–0.6 values; at the same time, they are situated in the largest distance from the reference point bringing the highest RMSE values during the 2-day forecast range. Regarding the temporal evolution of the scores, at some particular time steps (e.g., at 12h, 30h, 36h, not shown) one can conclude some temporary error reduction at the end of summer and the beginning of autumn. These features might be attributed to the particular meteorological situations, nevertheless, it is hard to find any seasonal behavior in the simulation results due to the short investigation period. For more detailed examination of the seasonal characteristics, it would be worthwhile, on the one hand, to extend the verification length, and on the other hand, to perform some smoothing and/or temporal averaging on the data in order to remove its large variability.

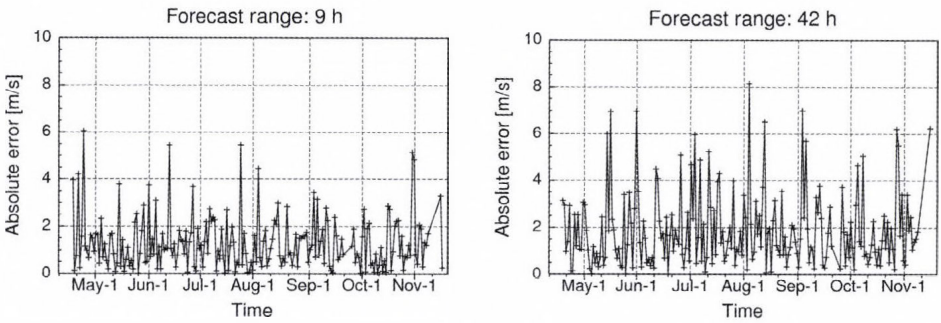

Fig. 11. Temporal evolution of the absolute error during the complete verification period in different forecast ranges (the time steps are calculated from the analysis time at 00 UTC): 9h on the left and 42h on the right. Verification period: April 19 – November 17, 2008; location: Mosonszolnok-Levél; height: 80 m.

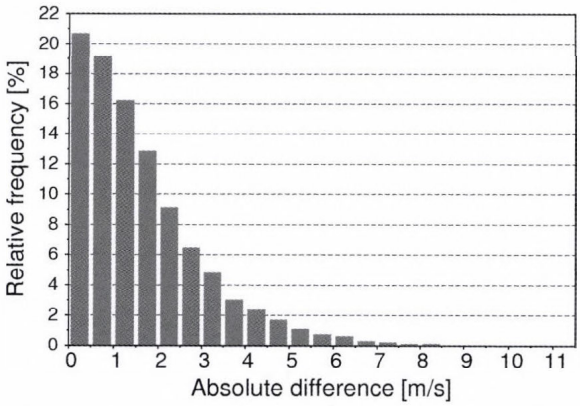

Fig. 12. Discrete empirical density function for the absolute errors. Verification period: April 19 – November 17, 2008; location: Mosonszolnok-Levél; height: 80 m.

4. Summary, conclusion, discussion, and future plans

In this article an overview was given about the applicability of the dynamical adaptation method originally developed by *Žagar* and *Rakovec* (1999) for wind power stations in Hungary. At the Hungarian Meteorological Service this special procedure is applied with the aim of improving operational wind predictions and providing more precise wind speed forecasts required by the wind power stations. The present paper is focusing on the validation results of the method: the dynamically adapted wind forecasts were compared and assessed with measurements at 80-meter height for a single location (namely Mosonszolnok-Levél) in a seven-month period. The selected point to be investigated in detail is situated at the northwestern part of Hungary, in approximately 120-meter height above the sea level. The anemometer stands in 78-meter height above the surface at a relatively strong wind tunnel, where the prevailing northwesterly flow streams over this flat area without barrier.

As far as the general quality of the operational forecasts is concerned, based on the verifications at two nearby SYNOP stations, it can be said that in the northwestern corner of Hungary the wind speeds are principally overestimated at the 10-meter height. The special dynamical downscaling improves the performance of the operational wind predictions, however, it cannot fully eliminate the positive bias. Regarding the main flavor of the fine-scale wind predictions at the higher 80-meter level for Mosonszolnok-Levél, it could be seen as follows:

- The wind speed forecasts during the 7 months are equally characterized by over- and underestimations resulting in almost no (0.1 m/s) systematic error;
- The intervals of 8–13 and 32–37 hours are characterized by small systematic underestimations, which are accompanied with relatively minor RMSE values;
- The intermediate periods are mostly exacerbated by overestimation and higher RMSE values;
- The errors do not have temporal evolution, i.e., they basically do not grow by the forecast range;
- Concerning the climatological features of the wind datasets, the low and high wind speeds (below 2 m/s and over 7 m/s, respectively) are over-represented in the model, whereas the occurrences of intermediate velocities are rather underestimated.

All this can be attributed to the fact, that basically DADA is unable to correctly represent the diurnal wind cycle. This weaker description of the daily velocity cycle might be associated with the deficiencies of the driving model, however, this statement should be thoroughly examined in the future. It would be worthwhile to further extend the investigations with the study of the seasonal behavior of the model (this certainly requires longer verification period),

additionally, the results should be scrutinized with respect to the wind direction, which could supply further hints regarding the strengths and weaknesses of the methodology in general and the ALADIN model in particular.

In spite of some identified deficiencies, the dynamical adaptation method provides not only an efficient, but also a reliable tool for the preparation of accurate wind predictions. At the same time, there are several further possibilities to "tune" the method in Hungary. The first "trivial" solution can be enhancing the spatial resolution of the target dynamical adaptation domain. The choice of 5 km horizontal grid spacing was motivated by that when the method was first tried, the topography was only available on this resolution, therefore, a further refinement of the applied grid would not make sense in the lack of more detailed surface description. Wind predictions are always valid at the gridpoint nearest to the given power plant, i.e., this resolution allows 3.5 km precision. It was indicated in *Table 1* that the orography on this resolution is relatively well described by the model in the investigated point: 125 versus 124 meters. Nevertheless, presently in the operational ALADIN model, an even finer topography is used, namely the GTOPO30 database (*Bliss* and *Olsen*, 1996) having 1 km resolution. The implementation of this detailed surface representation into the dynamical adaptation configuration can promise even better results. As far as the vertical resolution is concerned, the number of model levels could be still extended from the actually used 15 levels putting even more emphasis on the lower part of the atmosphere.

Regarding the Hungarian implementation of the dynamical adaptation procedure, another obvious concern is, whether the application of the half-hour model integrations for the operational outputs provided at every 15 minutes is correct from the aspect of temporal representativeness of the data. I.e., during this construction, the half-hour periods overlap each other, therefore, it is not evident on what time step the output of the DADA procedure can be considered (however, the same boundary conditions at the beginning and end of the short integration suppose that the forecast is valid for the initial time). Originally, the dynamical adaptation post-processing method was developed, when the model outputs were available only with 6- or maximum 1-hour frequency. But today the demands of the partners require the production of forecasts with denser temporal frequency.

One constraint of the method is that it is not able to attenuate the deficiencies of the applied initial and lateral boundary conditions, i.e., only the good-quality large-scale forcings can be improved by the dynamical adaptation procedure. On the other hand, even in case of correct driving fields, there are some small-scale phenomena that cannot be accounted by the larger-scale model, and the simplified dynamical adaptation is unable to additionally reflect them. In these processes other factors than the dynamic forcing are dominating (for instance, local thermal circulations or inversion situations), or for their accurate prediction the complete physical parameterization would have been needed on higher horizontal resolution (*Žagar* and *Rakovec*, 1999). Therefore, it is indispensable

to simultaneously develop the driving model, as well. In the last years, the operational ALADIN model applied at the Hungarian Meteorological Service has been undergoing continuous improvements and there are also some additional plans for enhancing the low-level wind forecasts of the model. The main realized and intended developments are briefly listed hereafter:

- The three-dimensional variational data assimilation scheme of ALADIN (*Bölöni*, 2006) were improved from the point of view of background error computations (*Bölöni* and *Horvath*, 2010) and the inclusion of new and emerging observations types into the assimilation process. The near-future activities focus on the increase of the data assimilation cycling frequency (to 3 hours) and also the computation of flow-dependent background errors with the establishment of an ensemble data assimilation system (*Adamcsek et al.*, 2010).
- The lateral boundary conditions of the ALADIN model were recently updated by the use of the ECMWF/IFS (Integrated Forecast System), which resulted in essential positive impact on the performance of the ALADIN model (*Bölöni et al.*, 2009).
- Wind forecasts can be further enhanced with the application of probabilistic information, which can be obtained by the operational ensemble prediction system of HMS. This short-range limited area ensemble system consists of downscaling the 11-member global ARPEGE-based ensemble of Météo France with the ALADIN meso-scale model (*Hágel*, 2010). Currently, experiments are ongoing for generation of local initial condition perturbations by ALADIN (with the method of singular vectors as employed also in ARPEGE).
- The latest developments are related to the installation of the non-hydrostatic AROME model in light of its near-future operational introduction at HMS (*Horányi et al.*, 2006). At the moment, the model is exploited quasi-operationally providing 36-hour forecast over a domain covering Hungary with 2.5 km horizontal and 60-level vertical resolution.

All these developments contributed and will contribute to the further enhancements of the operational version of the ALADIN model, and consequently, that of its wind predictions. Finally, it is mentioned here that some wind forecast improvements can be also assessed with the statistical post-processing of the raw wind prediction information, which can account for the elimination of systematic model errors. Nevertheless, in the future we are going to concentrate more on the dynamical refinements of the wind forecasts (as listed above) instead of the statistical approach.

Acknowledgements — The authors would like to express their special thanks to *Antal Balogh*, for his invaluable help in the establishment of the mutual beneficial cooperation with the power plant station at Mosonszolnok-Levél. This work was partly supported by the Hungarian National Office for Research and Technology (NKFP, grant No. 3A/0038/2002).

References

Adamcsek, E., Bölöni, G., Csomós, P., and *Horányi, A.,* 2010: The application of the Ensemble Transform Kalman Filter technique at the Hungarian Meteorological Service: Preliminary results. *Időjárás 114,* 21-37.

Alexandru, S., 2004: High-resolution dynamical adaptation of the wind forecast using the non-hydrostatic version of the ALADIN model. *ALADIN/ALATNET Newsletter 27,* 96-100.

Beck, A., Ahrens, B., and *Stadlbacher, K.,* 2005: Impact of nesting strategies in dynamical downscaling of reanalysis data. *Geophys Res Lett 31,* L19101, doi:10.1029/2004GL020115.

Beck, A. and *Ahrens, B.,* 2006: Third Interim Report to ECMWF Special Project – SPATAB01: Alpine regional downscaling of reanalysis data using the LAM ALADIN. Available at http://www.ecmwf.int/about/special_projects/finished_projects/beck_downscaling_reanalysis_data/report_2006.pdf.

Bliss, N.B. and *Olsen, L.M.,* 1996: Development of a 30-arc-second digital elevation model of South America. In *Pecora Thirteen, Human Interactions with the Environment – Perspectives from Space, Sioux Falls, South Dakota.*

Bölöni, G., 2006: Development of a variational data assimilation system for a limited area model at the Hungarian Meteorological Service. *Időjárás 110,* 309-328.

Bölöni, G. and *Horvath, K.,* 2010: Diagnosis and tuning of background error statistics in a variational data assimilation system. *Időjárás 114,* 1-19.

Bölöni, G., Kullmann, L., and *Horányi, A.,* 2009: Use of ECMWF lateral boundary conditions and surface assimilation for the operational ALADIN model in Hungary. *ECMWF Newsletter 119,* 29-35.

Hágel, E., 2010: The quasi-operational LAMEPS system of the Hungarian Meteorological Service. *Időjárás 114,* 121–133.

Horányi, A., Kertész, S., Kullmann, L., and *Radnóti, G.,* 2006: The ARPEGE/ALADIN mesoscale numerical modeling system and its application at the Hungarian Meteorological Service. *Időjárás 110,* 203-228.

Ivatek-Sahdan, S. and *Tudor, M.,* 2004: Use of high-resolution dynamical adaptation in operational suite and research impact studies. *Meteorol Z 13,* 99-108.

Kertész, S., Szépszó, G., Lábó, E., Radnóti, G., and *Horányi, A.,* 2005: Dynamical downscaling of the ECMWF ERA-40 re-analyses with the ALADIN model. *ALADIN/ALATNET Newsletter 28,* 78-83.

Nurmi, P., 2003: Recommendations on the verification of local weather forecasts. *Technical Memorandum 430,* European Centre for Medium-range Weather Forecasts, Reading, UK.

Simmons, A.J. and *Burridge, D.M.,* 1981: An energy and angular-momentum conserving vertical finite-difference scheme and hybrid vertical coordinates. *Mon Weather Rev 109,* 758-766.

Simmons, A.J. and *Gibson, J.K.,* 2000: The ERA-40 Project Plan. *ERA-40 Project Report Series 1.*

Taylor, K.E., 2001: Summarizing multiple aspects of model performance in single diagram. *J Geophys Res 106,* D7, 7183-7192.

Temperton, C. and *Staniforth, A.,* 1987: An efficient two-time-level semi-Lagrangian semi-implicit integration scheme. *Q J Roy Meteorol Soc 113,* 1025-1039.

Vasiliu, S., 2005: High-resolution dynamical adaptation of the ALADIN/Romania model's surface wind forecast. *Romanian Journal of Meteorology 7,* 29-40.

Yessad, K., 2009: Full-pos in the cycle 36 of ARPEGE/IFS. Technical documentation, Météo France. Available at http://www.cnrm.meteo.fr/gmapdoc/IMG/ps_ykfpos36.ps.

Žagar, M. and *Rakovec, J.,* 1999: Small-scale surface wind prediction using dynamic adaptation. *Tellus 51A,* 489-504.

Žagar, M., Žagar, N., Cedilnik, J., Gregorič, G., and *Rakovec, J.,* 2005: High-resolution wind climatology from ERA-40. *ALADIN/ALATNET Newsletter 28,* 101-104.

Žagar, N., Žagar, M., Cedilnik, J., Gregorič, G., and *Rakovec, J.,* 2006: Validation of mesoscale low-level winds obtained by dynamical downscaling of ERA40 over complex terrain. *Tellus 58A,* 445-455.

IDŐJÁRÁS

Quarterly Journal of the Hungarian Meteorological Service
Vol. 114, No. 1–2, January–June 2010, pp. 79–100

Impact of extreme rainfall and soil moisture on flash flood generation

Szabolcs Czigány*, Ervin Pirkhoffer, and **István Geresdi**

Department of Soil Sciences and Climatology, Institute of Environmental Sciences, Faculty of Sciences, University of Pécs
Ifjúság u. 6, H-7624 Pécs, Hungary; E-mail: szczigany@gamma.ttk.pte.hu

**Corresponding author*

(Manuscript received in final form January 28, 2010)

Abstract—Convective rainstorms frequently result in floods in small mountainous watersheds. This type of floods, called flash floods, may pose significant threat to lives and properties and present a particularly challenging natural phenomenon to predict with a sufficient lead time.

Our approach to predict flash floods is through runoff modeling. Hydrological models, however, require a plethora of input data. Some temporally variable data, such as precipitation intensity and soil moisture, significantly influence the calculated cumulative outflow and the forecasted peak discharge. In the present paper, the spatio-temporal behavior of soil moisture is studied with the means of time domain reflectrometry (TDR) technique and ArcGIS tools at 14 monitoring stations in an experimental watershed, SW Hungary. Based on field measurements, two minor discharge peak (MDP) events of the studied Sás Stream are simulated using the HEC Hydrologic Modeling System (HEC-HMS). Under the aforementioned environmental conditions, the largest flood event of 2008 on Sás Stream is simulated by a hindcast method. As no environmental data were available for this flood event, the majority of the parameters were estimated from monitored data and other data resources.

Soil moisture varies considerably in both space and time, but the variations among the measurement stations are predictable. Thus, we believe that from measurements at one location of the watershed, soil moisture can be estimated for the entire watershed.

Rainfall varies greatly, which constrains predictability. A possible solution to obtain the rainfall forecasts is the application of radar observation and meteorological models.

We found that HEC-HMS is suitable for model simulations as well as for the generation of a nationwide flash flood warning system. The HEC-HMS is only restrictedly applicable to reproduce flood events with low peak discharge as well as floods with multiple peaks. We also concluded that HEC-HMS exaggerates the impact of volumetric water content on flash flood generation.

Key-words: flash flood, hazard, soil moisture, monitoring, modeling, HEC-HMS

1. Introduction

In Hungary, weather phenomena often cause disasters (hail storms, floods, and mudflows) that subsequently generate considerable economic loss and may jeopardize human life. The most severe natural hazards in the country are associated with atmospheric convections and storms (*Horváth*, 2005). Intense upward convection triggers various phenomena ranging from small cumulus clouds to devastating supercells. Their devastation is further exacerbated by prediction challenges, as their magnitude and exact locality varies considerably in space. Convective processes develop rapidly and, with their associated features and consequences, may create tremendous damage and disastrous corollaries. Typical observed phenomena related to convective storms in hilly and mountainous regions are flash floods (*Horváth*, 1999).

According to the report of the Environmental Protection Agency of the European Union, floods generate the largest economic loss in Europe. The average annual economic loss caused by any type of natural hazards is estimated at 40 billion EUR: the Gard 2002 and the Aude 1999 flash flood events alone caused 1.2 and 3.3 billion EUR economic losses, respectively (*Lefrou et al.*, 2000; *Huet et al.*, 2003; *Gaume et al.*, 2009). Although the majority of the losses are caused by „conventional" large-river floods, over the past decades, floods more frequently occur on small streams located in small (10 to 100 km^2) mountainous watersheds. In Europe, lowland floods are rarely associated with fatalities; in contrast, often demand loss of life (*Gaume et al.*, 2009). Flash floods are generated 0.5 to 5 hours after an intense rainfall event and usually last for a few hours (in extreme cases up to a day). In certain cases, however, snowmelt may also contribute to the generation of flash floods, hence low-intensity rainfall, amid ideal environmental settings may also trigger flash floods (*Pirkhoffer et al.*, 2008). A third, recently more frequent type of flash flood occurs in heavily urbanized areas, where paved surfaces are impervious and, in general, runoff is affected by various human factors (*Gyenizse*, 2009). This latter type of floods is called urban floods or pluvial floods; however, some authors clearly differentiate them from typical flash floods (*Cobby et al.*, 2008).

Due to the geographical settings of western and northern Hungary, flash floods are frequent phenomena and have been reported several times over the past decades. However, prediction is rather challenging, due to the large spatial and temporal variability of the aforementioned convective rainfall events and the mosaical and heterogeneous pattern of topography, land use, and soil types. In addition, prediction uncertainty is very high due to the available rainfall forecasting methods, and the localized characteristics of the precipitation.

The majority of flash floods, at least in Hungary, occur between March and mid-October. Torrential, high-intensity precipitation caused significant economic loss in the hilly and low-mountain parts of Hungary. For example, the Által-ér in north-central Hungary inundated its valley following a 253 mm torrential

rainfall on June 4, 1953 (*Szilágyi*, 1954). On June 27, 1987, several houses and part of the railroad were washed away in the Bükkösd Valley (Mecsek Mountains, SW Hungary) when 71 to 88 mm rain fell during a 6-hour period (*Gyenizse* and *Vass*, 1998). In the latter case, the largest economic losses were reported from Hetvehely, a village that is located just upstream from the confluence of the Bükkösdi-víz and the Sás Streams. *Vass* (1998) concluded that, due to its rugged watershed topography, the Sás Stream is likely to be one of the major contributing and triggering factors for the extreme flash flood events of the trunk river. Perhaps the largest economic loss was associated with flash floods in Mátrakeresztes, when a flash flood inundated the valley of the Csörgő and Kövicses Streams on April 18, 2005 (*Horváth*, 2005). Economic loss was estimated to reach 1 billion HUF (approximately 5 million USD) there. The city of Kaposvár was flooded by the Kapos Stream on August 21, 2008 (*Hizsák*, 2005) when 105 mm rain fell in 3 hours. However, we need to emphasize that in terms of discharge, the flash floods of Hungary are not comparable to those documented for the Alps (e.g., *Ranzi et al.*, 2007), although in terms of general characteristics, behavior, and economic loss caused the Hungarian flood events bear a close resemblance with the Alpine floods.

Rainfall is considered to be the primary triggering factor for flash floods, but certain environmental temporally-variable boundary conditions, at least by many authors, are also considered to be crucial. These environmental factors include canopy cover (land use) and antecedent soil moisture content (e.g., *Cassardo et al.*, 2002; *Smith et al.*, 2002; *Le Lay* and *Saulnier*, 2007; *Jessup* and *DeGaetano*, 2008). Other authors, however, found little correlation between magnitude of runoff and land use or soil type (*Merz et al.*, 2006), or found peak discharge unaffected by antecedent soil moisture content (*Cras et al.*, 2007). Volumetric water content (hereafter VWC), on the other hand, not only affects runoff, but may also influence rainfall generation (*Cassardo et al.*, 2002).

These environmental factors affect the time of concentration, and indirectly the prediction time lead. Prediction time lead, in turn, will strongly influence the general character of analysis, prediction, prevention, and evacuation. To overcome the challenging prediction issues in unexplored and (quasi-) ungaged small watersheds, hydrological models may be an appropriate tool to forecast flash flood events in sufficient lead time (e.g., *Georgakakos*, 1986; *Ogden* and *Julien*, 2002; *Georgakakos*, 2002; *Javier et al.*, 2007). However, hydrological models of this type require a plethora of input data. In this case, not only the precipitation is essential as input data, but the model processes topographic data (digital elevation model, hereafter DEM), land use and land cover, and various soil properties, such as infiltration rate, topsoil thickness and soil moisture content.

To simulate selected flood events, we employed the HEC-Hydrologic Modeling System (hereafter HEC-HMS, developed in Davis, CA, United States) in the present study. Based on the available environmental data of a 6.7 km^2 watershed in SW Hungary, we verified the suitability of the HEC-HMS model

for small watersheds (and in the future, for the entire hilly and low-mountain areas of Hungary). Over the verification process, we numerically simulated two MDP events that occurred on the Sás Stream during fall, 2008. Subsequently, we aimed at numerically simulating a large flash flood event that occurred on June 4, 2008. As the watershed was ungaged at that time, i.e., neither on-the-spot precipitation data, nor VWC data were available for this particular event, our objective was to reconstruct both antecedent soil moisture content and changes in rainfall intensity during the precipitation event based on data of other nearby rain gages, radar observations, and available air temperature.

2. Materials and methods

2.1. General description of the study site

The study area is one of the headwater subbasins of the Sás Stream and is located in the NW part of the Mecsek Hills, SW Hungary and on the eastern edge of the Zselic Hills (*Fig. 1*). The watershed covers an area of 6.7 km^2 and belongs to the broader catchment of the Bükkösdi-víz. The watershed of the Sás Stream has a typical low mountain character with a steep V-shaped gorge in the headwaters of the watershed and is bordered with slopes generally exceeding 20°. The 14 monitoring stations are located on the smaller western watershed of the Sás Stream watershed, covering a mere 1.7 km^2. Based on the Corine Land Cover 2000 database, 90.6% of the watershed is covered with deciduous forest primarily of beech (*Fagus sylvatica*). The watershed exhibits frequent, but randomly distributed clearings (*Fig. 1*).

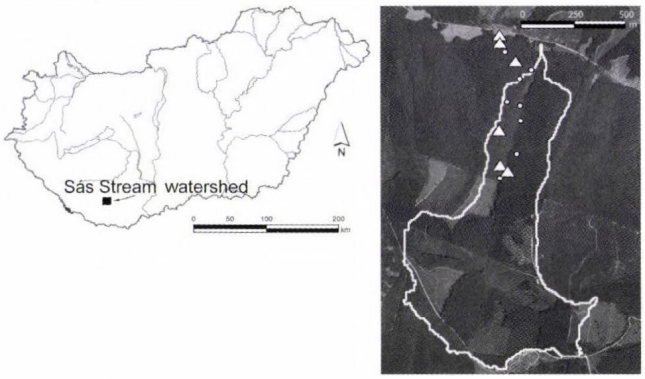

Fig. 1. Location of the studied watershed, soil moisture monitoring stations (dots and triangles), and combined soil moisture stations with rain gages (triangles)

Stream discharge ranged from 0.001752 m^3 s^{-1} to 0.9351 m^3 s^{-1} over 2008. Peak discharge was observed on June 4, at 22:00 CET. For simulation purposes,

during the period of our monitoring project (between September 5 and December 5, 2008), we selected two MDP events: the first one occurred on October 4 and a second on October 17.

2.2. Determination of soil physical type

In order to determine the soil physical type of the monitoring stations, topsoil samples were taken from 13 monitoring stations. One station located on the very edge of the alluvial plain was ignored. Soil samples were treated with 10% HCl and H_2O_2 in order to remove $CaCO_3$ and organic matter, respectively. Following the treatments, soil samples were diluted with DI water and subsequently were centrifuged at 3,000 rpm. After centrifugation, supernatant was decantated and were ovendried at 60 °C until a paste was obtained. Particle size was then determined with static light scattering method using a Fritsch Analysette 22 (Fritsch GmbH, Idar-Oberstein, Germany) instrument.

2.3. Monitoring of VWC

Due to the large input data demand of the selected HEC-HMS runoff model for the simulation of flash flood events, the measurement, quantification, and estimation of several environmental factors were essential. Owing to its geographical proximity, appropriate environmental settings, and its significant contribution to the floods of the trunk river, we selected the western watershed of the Sás Stream (left tributary of the Bükkösdi-víz, SW Hungary) for simulation purposes (*Fig. 1*). Here regular environmental monitoring was undertaken for the period of September 5, 2008 – January 5, 2009. During this period we regularly monitored VWC (θ_v) and canopy cover at 14 monitoring stations (*Fig. 1*). These two types of data, among many other ones, are crucial input for the HEC-HMS modeling software applied. As the output data of the HEC-HMS are highly sensitive to VWC, our measurements primarily focused on the determination of soil moisture content over the watershed. Another explanation to focus on VWC in the present study is its large spatial and temporal heterogeneity as well as its predominant role in flash flood generation.

Soil moisture content was measured with the time domain reflectrometry (TDR) technique. The applied TDR-300 instrument (Spectrum Inc., Planfield, Illinois, United States) was equipped with 20 cm long stainless steel rods. Soil moisture content was measured in a circle of 1.5 m radius at each monitoring station. At each station three repeated measurements were taken, and subsequently measured values were averaged. At the beginning of the measurement period, two plots of about 2 m by 1 m were created at each monitoring station, one plot covered with forest litter, while from the other plot forest litter was removed. However, as no significant variation in VWC was found among the two types of plots, litter-free measurements were then terminated. Measured data was then

plotted in ArcGIS 9.2 and interpolated with the inverse distance weighted function to determine the general trend of spatial soil moisture pattern. As the HEC-HMS model requires soil saturation (in percentage), measured volumetric water content values were converted to saturation percentage based on Eq. (1).

$$S=\varepsilon\cdot\theta_v\cdot 100, \tag{1}$$

where S is the saturation, ε is the porosity and θ_v is the VWC. This conversion requires the determination of soil bulk density and specific density, then, subsequently porosity is calculated as follows:

$$\varepsilon=1-\left(\frac{\rho_b}{\rho_s}\right), \tag{2}$$

where ρ_b is the bulk density and ρ_s is the specific density of soil. The average porosity of the collected soil samples was determined with a pycnometer, according to *Flint* and *Flint* (2002). We obtained an average porosity of 0.48 of 14 collected topsoil samples, thus, we received a conversion factor of 208 between VWC and saturation percentage. This soil porosity value was applied for the entire studied watershed, as well as all monitoring stations, as soil physical type does not vary significantly over the area of the watershed (*Table 1*).

Table 1. Particle size distribution of topsoils at 13 monitoring stations

Monitoring station ID	d_{mean} (μm)	Clay (%)	Silt (%)	Sand (%)	Physical soil type
2	19.479	10.29	88.18	1.53	silt
3	37.361	5.42	80.33	14.25	silty loam
4	30.156	6.66	83.65	9.69	silty loam
5	29.726	7.77	82.31	9.92	silty loam
6	31.58	6.72	82.44	10.84	silty loam
7	25.435	7.44	87.04	5.52	silty loam
8	29.12	8.25	81.37	10.38	silty loam
9	33.98	6.9	79.59	13.51	silty loam
10	29.429	6.85	83.79	9.36	silty loam
11	32.435	6.66	81.88	11.46	silty loam
12	36.368	4.71	82.21	13.08	silty loam
13	36.555	4.54	77.22	18.24	silty loam
14	27.205	8.3	85.32	6.38	silty loam

2.4. Employed precipitation data for the HEC-HMS model

Besides the VWC measurements at the 14 monitoring stations, between October 10, 2008 and October 17, 2008 daily rainfall measurements were carried out at 6

selected monitoring stations (out of the 14 stations used for VWC determination) using Hellmann type rain gages. The locations of the deployed rain gages are shown in *Fig. 1*.

To reconstruct rainfall intensities during the two MDP event, we used the following rainfall data observed at rain gages located in the relative proximity of the Sás Stream:

- Pécs, at University of Pécs, Ifjúság Street Campus, located at 46°04'40.47" N, 18°12'22.68" E (intermittent data between September 1 and December 5, both tipping bucket and Hellmann type rain gages).
- Central Pécs, located at 46°03'34.31" N, 18°13'39.35" E, daily cumulative precipitation data from June 15, Hellmann type rain gage.
- Orfű automated rain gage located at 46°08'23.77" N and 18°13'39.35" E, 10-minute cumulative rainfall data from September 22, 2008, tipping bucket rain gage.
- Hetvehely automated rain gage, located at 46°07'39.19" N and 18°02'04.22" E about 3 km west of the studied watershed, tipping bucket rain gage.
- Pogány automated meteorological station located at 45°59'41.22" N and 18°14'05.71" E, daily cumulative data, obtained from the publicly available website of the National Oceanic and Atmospheric Administration (NOAA) database, accessible at http://www.ncdc.noaa.gov.

2.5. Applied air temperature data

Air temperature data was obtained from two sources:

- Mean daily air temperature was obtained from the publicly available NOAA database, accessible at http://www.ncdc.noaa.gov.
- 1-minute and 10-minute air temperature data was observed at University of Pécs, Ifjúság Street Campus (exact location is the same as for the rain gage).

2.6. Applied stream discharge data

Water level data of 30-minute temporal resolution for the Sás Stream were measured in the central part of the Sás Stream watershed. Stream gage is located at 46°07'12.29" N and 18°04'07.05" E. Discharge data were received from the MecsekÉrc Ltd., a daughter company of the former Uranium Ore Mining Company.

2.7. Model setup

Runoff was calculated by the HEC Hydrologic Modeling System (HEC-HMS, developed in Davis, CA, United States) surface runoff model that calculates

stream discharge as a function of input precipitation and various environmental parameters. The HEC-HMS is designed to simulate the precipitation-runoff processes of dendritic watershed systems. It is designed to be applicable in a wide range of geographic areas for solving the widest possible range of problems. This includes large river basin water supply and flood hydrology, and small urban or natural watershed runoff (*US Army Corps of Engineers*, 2005).

For simulation purposes we selected the two afore mentioned MDP events. The reason for selecting these two, rather low-discharge floods, was sufficient data availability (10-minute rainfall, soil moisture, and canopy cover) for this period. The simulation of the selected two MDP events were extremely challenging as the peak discharge values only slightly exceeded the average baseflow, and the event observed on October 17, 2008 showed a fluctuating sawtooth-type, multi-peak pattern.

To set up the model, we employed the soil moisture accounting (SMA) module of HEC-HMS that determines the ratio of runoff and infiltration based on set parameters shown in *Table 2*. This method is a built-in function of the HEC-HMS.

Table 2. Value and quantification methods of the input environmental parameters of the October 4 and October 17 MDP events for the HEC-HMS model. Note, that not all the parameters of the SMA module are shown

Input parameter	**Value used for best simulation**	**Method of quantification**
Canopy saturation (%)	0	Estimated and measured leaf wetness
VWC ($m^3\ m^{-3}$)	0.269/0.2836/0.192[1,2]	Measured (TDR)
Soil saturation (%)	56/59/40[1]	Measured (TDR)
Canopy storage (mm)	2	Estimated, based on literature (e.g., *Gash et al.*, 1980)
Surface storage	2	Estimated from DEM
Maximum infiltration rate ($mm\ h^{-1}$)	26	Particle size distribution measured, then infiltration rate was based on literature
Soil thickness and water storing capacity (mm)	220	Based on field measurements and the AGROTOPO soil database

[1]June 4, 2008/October 4, 2008/October 17, 2008

[2]The reason for showing both VWC and water saturation is that the TDR measures in VWC, while HEC-HS requires water saturation as input data

To set the input hydraulic parameters, we employed the Clark Unit Hydrograph function. Here time of concentration was determined from the time

lag between the precipitation event and the peak discharge (*Fig. 2*). As this parameter highly depends on actual rainfall intensity, the time of concentration needs to be determined for each precipitation-discharge pair and adjusted according to the total contributing land area.

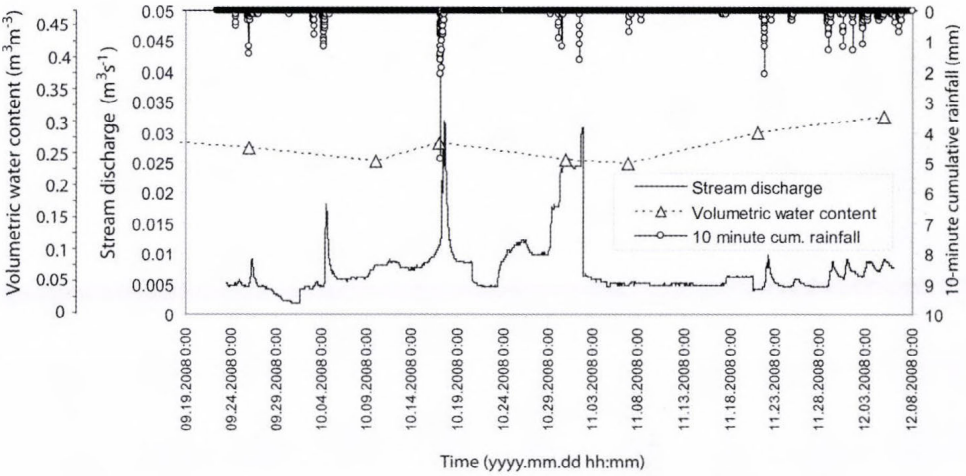

Fig. 2. Correlation between stream discharge of the Sás Stream, VWC and 10-minute cumulative rainfall (observed in Orfű) between September 5 and December 5, 2008.

3. Results

3.1. Input data acquisition

The smallest difference between the observed and simulated flow was found at SMA settings shown in *Table 2.* Parameterizations for each individual SMA are also shown in *Table 2.*

Input soil moisture, as it is indicated in *Table 1,* was obtained from the area-averaged TDR measurements (and temporal interpolation) in our study site. Over the period of measurement, VWC ranged between 0.148 $m^3 m^{-3}$ (September 5, 2008) and 0.324 $m^3 m^{-3}$ (December 5, 2008) (*Fig. 2*). At the measured porosity values, these volumetric water contents equal to 30.72% and 67.4% average water saturation, respectively. In general, topography (besides the slight impact of coarse rocky fragments) overwhelmingly impacted the spatial distribution of soil moisture content. Based on ArcGIS interpolation (using the inverse distance weighted function), highest soil moisture values were always detected at the perimeter of the alluvial plain (lowest elevation), while lower value were observed with increasing altitude (*Fig. 3*).

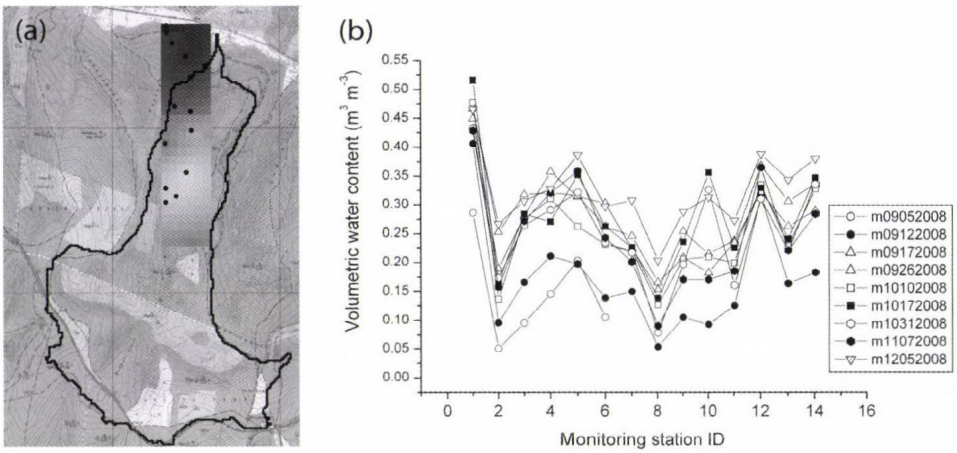

Fig. 3. Raster-based interpolation of VWC based on the October 17, 2008 TDR measurements. Darker pixels indicate higher soil moisture content.

Both mean and extreme soil moisture values varied greatly among the monitoring stations, but behaved spatially consistently over the small (1.7 km^2) watershed (*Fig. 3*). This observation was clearly exemplified during the September 26, 2008 precipitation event, when daily cumulative precipitation ranged between 13.6 and 14.6 mm over the 14 monitoring stations. Despite the relatively uniform spatial distribution of rainfall, VWC ranged between 0.166 and 0.455 m^3 m^{-3}.

Minimum measured values for the entire monitoring period were usually observed at monitoring station 8. At this point, shallow soil and frequent occurrence of coarse fragments are likely to be responsible for the low degree of saturation. On average, the second lowest soil moisture content was measured at monitoring station 2. Here, the low moisture content is explained by the dense rhizosphere where preferential flowpaths are responsible for the high initial infiltration rate. This was further confirmed by the authors' on-site dye experiment. Additionally, at monitoring station 2, topsoil has an extremely granular structure, which further enhances infiltration. Monitoring station 10 is located at the edge of a clearing, thus, long-term water balance is typically characterized with extreme VWC. However, the consistency of the spatial correlation of soil moisture content among the 14 monitoring stations is noteworthy and clearly shown in *Fig. 3*. Besides the changes of physical soil type, steeper slopes and decreasing soil depth may contribute to decreasing soil moisture at higher elevation.

Nonetheless, the literature-based strong impact of VWC on runoff (e.g., *Jessup* and *DeGaetano*, 2008) is not entirely reflected in the discharge/soil moisture content chart (*Fig. 2*). This low-degree correlation may be attributed to

the low temporal resolution of our soil moisture measurements (weekly and biweekly intervals), the rugged topography of the studied watershed (thus limited infiltration), and the dominant effect of temperature on evaporation rate. The timing of the soil moisture measurement is also crucial, most accurate values are obtained when the date of measurement immediately precedes the precipitation event.

Maximum infiltration rate, as input data for the hydrological model, was based on literature data (e.g., *Jury et al.*, 1991; *Hillel*, 1998) and the actual physical soil type (particle size distribution) collected from the uppermost soil horizons at each monitoring stations, with the exception of monitoring station 1 (located on the edge of the alluvial valley floor). Based on the particle size distribution, the topsoils of the studied catchment, with one exception, belong to the silty loam soil physical type (*Table 1*). Thus, based on literature, initial infiltration rate was set to 26 mm h^{-1}.

As clearly exemplified here by the identical soil physical types, soil type alone does not account for the varying water budget of soils. It needs to be emphasized, however, that our particle size measurement was applied for particles smaller than 300 μm. At higher elevation (monitoring stations 8 and 9) the increased frequency of coarse rocky fragments is detectable, assuming the presence of preferential flowpath at the edge of the coarse fragments, while the upper surface of this rock fragment may behave as an impervious surface.

3.2. Reconstruction of the October 4, 2008 rainfall event

To reconstruct the rainfall for the October 4, 2008 MDP event, we used three rainfall time series sources: (a) 10-minute cumulative rainfall series from the automated Orfű rain gage, (b) 10-minute cumulative rainfall series from the automated Hetvehely rain gage, (c) the authors on-site measurement by Hellmann-type rain gages, and (d) radar images.

Only a minor difference was detected among the six-station-averaged rainfall measured in the watershed of the Sás Stream (with a mean value of 15.2 mm, ranging between 14.6 and 16.7 mm), the Hetvehely rain gage (14.2 mm), and the Orfű automated rain gage (15.6 mm). To reconstruct the temporal fluctuation of rainfall intensities in 10-minute time intervals, we employed the data supplied by the Hetvehely rain gage. Intensity in general was low and relatively even for this event, reaching a maximum intensity of 1.2 mm h^{-1} between 7:50 and 8:00 A.M. (*Fig. 4c*). The 10-minute cumulative data series of the Hetvehely data was then multiplied by a factor of 0.934 (i.e., 14.2/15.2). By doing this, we obtained a temporal distribution identical to that of the Hetvehely rain gage, while the cumulative rainfall was equal to that measured in the watershed of the Sás Stream.

However, despite the non-convective character of the rainfall event, total cumulative rainfall differed largely within an area of about 10 km in radius.

Cumulative daily rainfall totaled 8.6 mm at the automated Pogány meteorological station, 12.3 mm in central Pécs, and 11.5 mm at the Ifjúság Street Campus of University of Pécs.

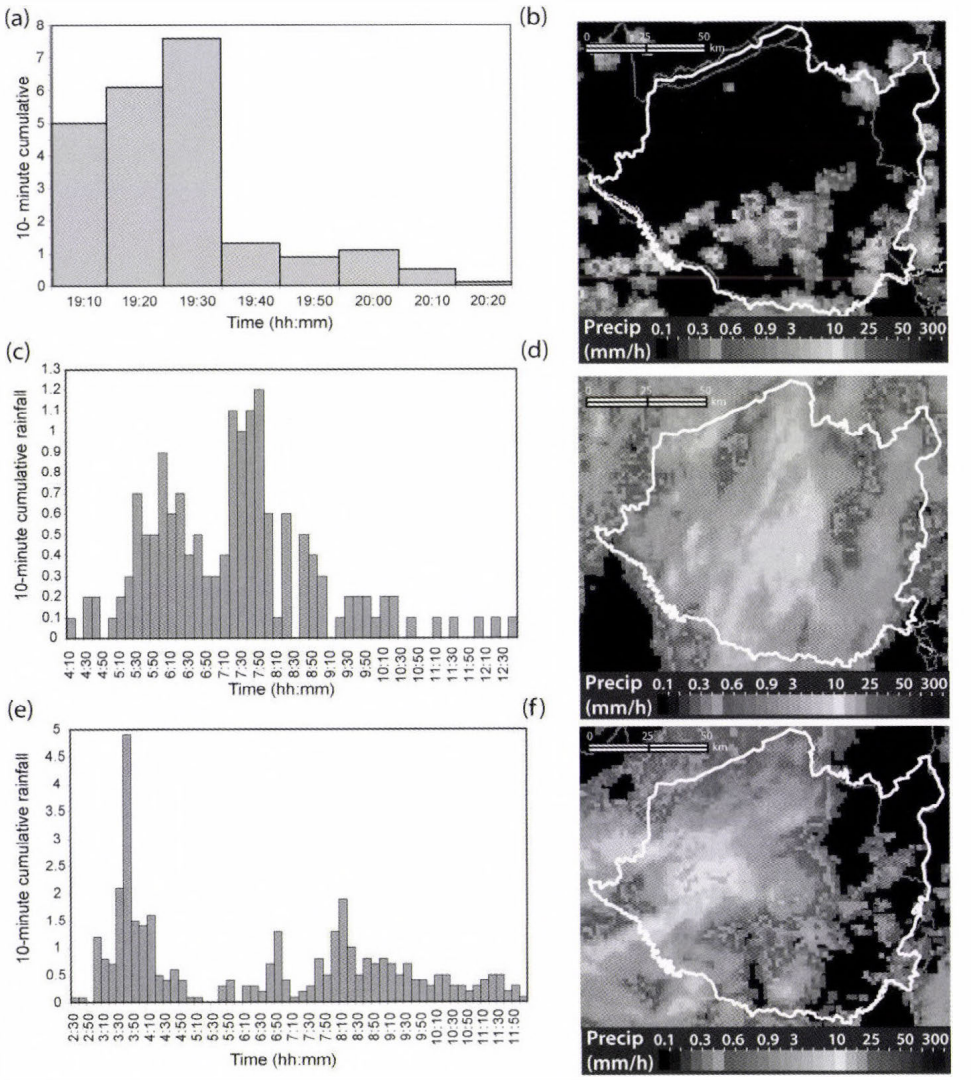

Fig. 4. (a) 10-minute cumulative rainfall observed in Hetvehely during June 4, 2008; (b) characteristic radar image taken during the June 4, 2008 rainfall event; (c) 10-minute cumulative rainfall observed in Hetvehely during October 4, 2008; (d) characteristic radar image taken during the October 4, 2008 rainfall event; (e) measured total daily rainfall values in Hetvehely (NOAA data) on October 17, 2008; (f) characteristic radar image taken on October 17, 2008.

Interpolated and estimated volumetric water content for October 4, 2008 was 0.260 $m^3 m^{-3}$ (54.1% water saturation). In the case of the latter event, the simulation best reproduced the observed hydrograph at 56% saturation. This difference is less than the measurement accuracy of the employed TDR instrument (± 0.01 $m^3 m^{-3}$). The measured average VWC of 0.282 $m^3 m^{-3}$ (58.6% water saturation) for October 17, 2008 was only slightly less than the 0.284 $m^3 m^{-3}$ (59%) used as input value in the HEC-HMS.

3.3. Reconstruction of the October 17 rainfall event

Similarly to the MDP event discussed in the previous section, to reconstruct the October 17, 2008 rainfall time series, we used three types of data: (a) 10-minute cumulative rainfall series from the automated Orfű rain gage, (b) 10-minute cumulative rainfall series from the automated Hetvehely rain gage, (c) the authors on-site measurement by Hellmann-type rain gages, and (d) radar images.

Our field rainfall measurements at six of the total of 14 monitoring stations resulted in 16.3 mm cumulative precipitation on average (ranging between 13.0 mm and 18.2 mm, depending on the location of the monitoring station), which is significantly less than that of measured by the Orfű rain gage located second closest to the study area in a distance of 6.70 km (36 mm). During most of the rainfall event, intensity was low, with the exception of a 10-minute period, when cumulative rainfall totaled 4.9 mm (*Fig. 4e*). At the Hetvehely rain gage, a cumulative rainfall of 24.7 mm was observed. This large difference in cumulative rainfall among the observation sites is attributed to the convective character of the rainfall event (indicated by the radar image in *Fig. 4f*), the rugged topography (orographic effects), and interception. However, the two automated rain gages are not covered by canopy, still it is unlikely, at least based on the available literature, that interception alone would account for that considerable difference (e.g., *Rutter et al.*, 1975; *Gash* and *Morton*, 1978; *Gash et al.*, 1980; *Klaassen et al.*, 1998, *Link et al.*, 2004). This latter statement is further confirmed by the authors' rainfall measurement on October 4, 2008, when a mere 0.4 mm difference in rainfall amounts was observed between the Sás Stream observation sites and the Orfű rain gage (see previous section 3.2). The radar based precipitation intensity, however, probably overestimated rainfall intensities, and care needs to be taken when radar data is used in rainfall forecast or prediction of flood levels.

As the model requires temporal changes of rainfall intensity during a given rainfall event, 10-minute rainfall intensities of the Hetvehely rain gage data (located closest to the studied area) were multiplied by a factor of 24.7/16.3 (i.e., 1.51) to obtain a cumulative value measured in the watershed, which were then employed in the model simulation runs. We note that the figure for cumulative daily rainfall we obtained on-site (i.e., in the Sás Valley) only slightly differed from that measured in central Pécs, at a distance of 15.05 km (16.0 mm), and

were somewhat higher than that observed in Pogány at a distance of 19.64 km (11.9 mm). For the period of October 6 – October 29 a total of 22.5 mm rainfall was measured at the Ifjúság Street Campus of University of Pécs (at a distance of 12.21 km).

Rainfall observations from the Pogány meterological station have been available since 1953 (longest record in Baranya County) and could be potentially used as input time series to simulate flash flood events on the adjacent streams. However, based on the poor correlation among the Orfű, Hetvehely, and Pogány daily precipitation data, we conclude that the 10-minute resolution Pogány precipitation data, mainly for convective precipitation, should be used with extreme caution for the estimation of total rainfall for the watershed of the Sás Stream. To overcome such difficulties, data of rain gages located closer to the studied streams should be used. The Orfű and Hetvehely rain gages, which were put to operation recently, may offer substitute solutions to aid the estimation of actual cumulative rainfall and precipitation intensities in the watersheds of the western Mecsek Hills.

The simulated results for the two MDP events, at least considering the shape of the curve, is similar to the observed hydrograph. The cumulative simulated outflow was considerably smaller than the total observed outflow in the case of the October 4, 2008 event (*Table 3*). However, in the case of the October 17, 2008 event, the simulated outflow exceeded the simulated value. Furthermore, the HEC-HMS was unable to reproduce the multi-peak pattern of the October 17, 2008 MDP event. In the latter case, the volume of the simulated cumulative outflow was 1.19 times larger than the observed one, while peak discharges hardly differed (*Table 3*). This large discrepancy is probably explained by (i) the extremely low peak discharge values, and (ii) the sawtooth pattern of the discharge peaks.

Table 3. Peak discharge and cumulative outflow values for the simulated and observed outflows of the October 4, 2008 and October 17, 2008 MDP events

	Peak discharge ($m^3 s^{-1}$)	**Cumulative outflow (1000 m^3)**	**Outflow difference compared to observed (%)**
Observed, October 4, 2008	0.02	1.23	
Simulated, October 4, 2008	0.02	0.73	– 40.65
Observed, October 17, 2008	0.03	1.56	
Simulated, October 17, 2008	0.03	1.85	+18.59

3.4. Simulation results of the June 4, 2008 flood event

To verify our results and settings obtained by the simulation of the October 4, 2008 and October 17, 2008 MDP events, we simulated the largest flood event on the Sás Stream in 2008. This flood event took place in the evening of June 4, 2008, when peak discharge reached 0.93 $m^3 s^{-1}$ as a result of a 22.6 mm rainfall (measured in Hetvehely) that reached its highest rainfall intensity between 19:20 and 19:30 (*Fig. 4a*). According to the radar images, the storm was located over the watershed of the Sás Stream between 18:45 and 20:00 CET. Since no rainfall data was available from the immediate vicinity of the watershed, it was essential to reconstruct the flood-generating rainfall based on precipitation data of other rain gages and radar images.

To reconstruct the total precipitation and rainfall intensity for June 4, 2008, we used the Hetvehely automated rain gage data and 15-minute resolution radar images obtained from the Hungarian Meteorological Services. The input precipitation data was aided by radar based rainfall intensities and timing (*Fig. 4*).

Environmental settings for the SMA loss method and the Clark Unit Hydrograph functions were identical to those used in the two MDP simulations, with the exception of soil moisture content.

As no measured soil moisture data is available for June 4, 2008, it was necessary to reconstruct the soil moisture content based on observed mean daily air temperature and field measurements on June 9 and June 10, 2008 and in June 2009. Air temperature is a suitable indicator of soil moisture changes, which fairly well reflects temporal changes of soil wetness. In our studied watershed, mean daily temperature measured in Pogány and VWC show a strong reverse correlation ($r^2 = 0.9629$), which further supports the suitability of air temperature for the estimation of the actual VWC. We partly estimated the soil moisture content based on the mean daily temperatures of NOAA for Pogány (*Fig. 5*).

Over this 15-day period, average air temperature was 18.2 °C. Based on the equation of the trendline in *Fig. 5*, the approximate VWC was only 0.210 $m^3 m^{-3}$, if the average temperature of the preceding 15-day (18.2) is applied. If soil moisture is calculated with the mean temperature of June 4, 2008 (17.9 °C), then the obtained VWC is 0.212 $m^3 m^{-3}$. The last two rainfall events prior to June 4, 2008 occurred on May 20 and May 21, 2008, with a cumulative rainfall of 22.1 and 10.2 mm. On June 9 and June 10, 2008, the average, however random (i.e., not at the monitoring stations) TDR measured VWC values in the Sás watershed reached 0.341 and 0.327 $m^3 m^{-3}$, respectively. The large VWC values measured on June 9 and June 10 are likely explained by daily rainfalls of 2.2 mm, 10.1 mm, 3.1 mm, 2.1 mm, and 1.5 mm (observed in Hetvehely) between June 5, 2008 and June 9, 2008, respectively. The average VWC for the same period in 2009 (measured on June 5) ranged between 0.17 and 0.45 $m^3 m^{-3}$ in the Sás watershed with a mean value of 0.28 $m^3 m^{-3}$.

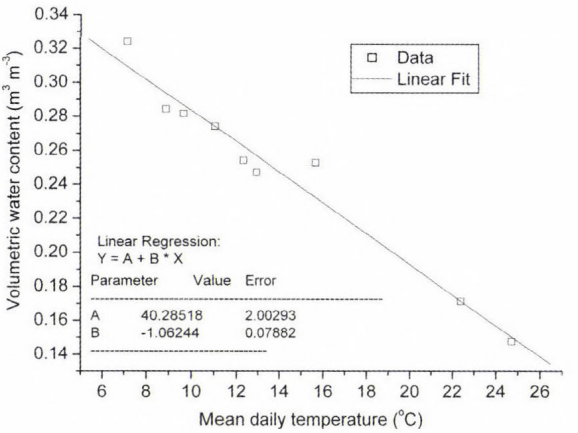

Fig. 5. Effect of mean daily temperature (observed in Pogány) on VWC between September 5, 2008 and December 5, 2008.

Based on the aforementioned environmental factors, we concluded that, preceding the rainfall event of June 4, 2008, the mean VWC of the Sás watershed ranged between about 0.150 and 0.300 $m^3 m^{-3}$ in the watershed of the Sás Stream. The exact average value was then determined by numerical simulation, using the HEC-HMS.

Table 4. Observed and simulated peak discharge and cumulative outflow values for the June 4, 2008 flash flood event at various VWC values

	Peak discharge ($m^3 s^{-1}$)	**Difference compared to observed (%)**	**Cumulative outflow (1000 m^3)**	**Difference compared to observed (%)**
Observed	0.93		7.79	
Simulated at a VWC of 0.168 $m^3 m^{-3}$	0.43	–53.76	3.80	–51.22
Simulated at a VWC of 0.192 $m^3 m^{-3}$	0.86	–7.52	7.60	–2.50
Simulated at a VWC of 0.216 $m^3 m^{-3}$	1.30	+39.78	11.40	+46.34

The best simulation results were obtained at a VWC of 0.192 $m^3 m^{-3}$ (40% water saturation). In this case the total volume of the observed outflow reached 7,100 m^3, while in the case of the simulated outflow it reached 7,600 m^3, when peak discharges were 0.93 $m^3 s^{-1}$ and 0.86 $m^3 s^{-1}$ for the observed and simulated outflows, respectively (*Table 4*). Due to the more regular shape of the June 4, 2008 flood event, the shape of the simulated curve was closer to the observed curve than in the cases of the MDP events (*Fig. 6c*). Similarly, in the case of the

June 4, 2008 flood event, the simulated and observed hydrographs bore a closer resemblance than in the case of the two simulated MDPs. This difference is likely caused by the irregular shape of the MDPs and the unsuitability of HEC-HMS to reproduce flash flood events of low peak discharge and cumulative outflow values.

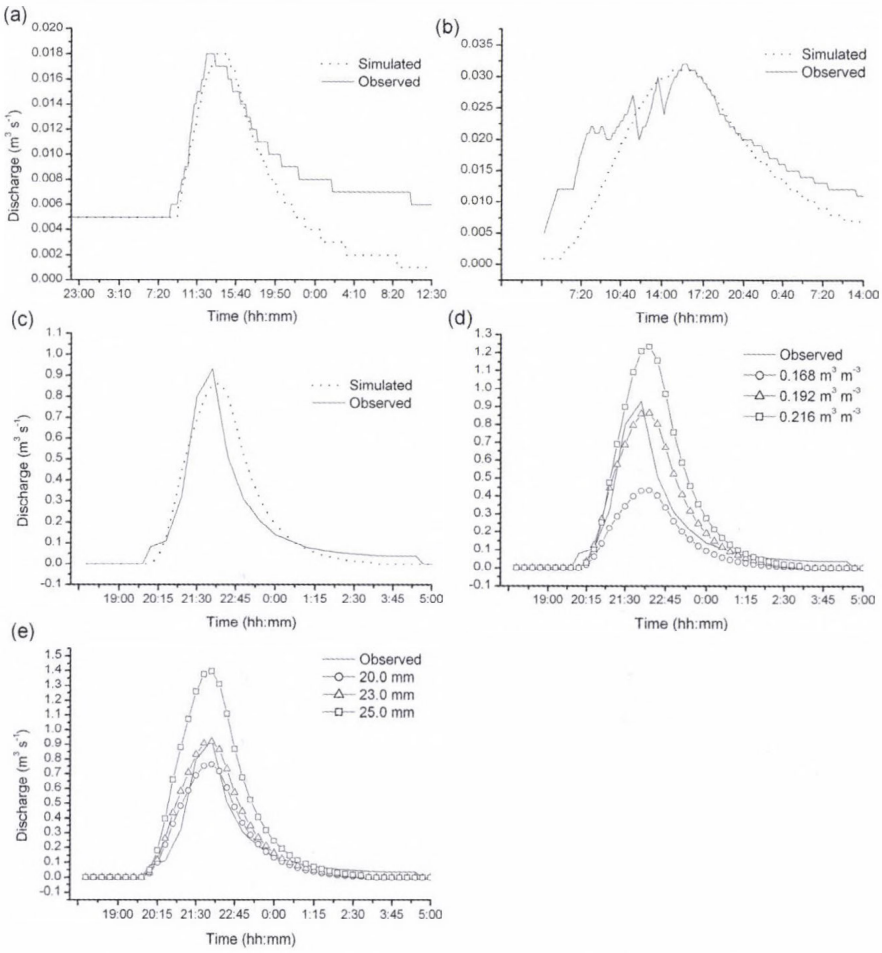

Fig. 6. Observed and simulated hydrographs of the flash flood event of the Sás Stream on (a) October 4, 2008, (b) October 17, 2008, and (c) June 4, 2008; (d) effect of various VWCs on modeled outflow generated by the HEC-HMS at a cumulative rainfall of 22.6 mm for the June 4, 2008 flood event; (e) effect of various cumulative rainfall on modeled outflow generated by the HEC-HMS at a VWC of 0.192 m^3 m^{-3} for the June 4, 2008 flood event.

When the input VWC was set to 0.168 m^3 m^{-3} (0.350% water saturation), simulated cumulative outflow was 51.22% less than the observed outflow (*Fig.*

6d and *Table 4*). Best fit was obtained at a VWC of 0.192 m^3 m^{-3} (45% water saturation) when the model underestimated the peak discharge by only 7.52%, while the cumulative outflow differed by only 2.5% from the observed outflow. At the best fit, however, cumulative outflow difference was less than in the case of the two MDP events. However, when input VWC was set to 0.216 m^3 m^{-3}, the model overestimated both peak discharge and cumulative outflow by 39.78% and 46.34%, respectively (*Table 4*).

Due to the lack of actual rainfall data on the Sás watershed (closest observation is about 3 km to the west), we also simulated the effect of various input precipitation for the June 4, 2008 event at a VWC of 0.192 m^3 m^{-3} (*Fig 6e* and *Table 5*). Best correlation between the observed and simulated output was obtained at 23 mm rainfall (i.e., 0.4 mm more than observed at the Hetvehely rain gage) if a VWC value of 0.192 m^3 m^{-3} was applied. In this case, observed and simulated peak discharge was almost identical (with a difference of only 1.07%), while the simulated cumulative outflow exceeded the observed value by 14.63% (*Table 5*). Both cumulative outflow (+46.34%) and peak discharge (+39.78%) greatly increased when a cumulative rainfall of 25 mm was applied in the model. Here we may conclude that the role of precipitation, similarly to VWC, is also exaggerated in the HEC-HMS.

Table 5. Observed and simulated peak discharge and cumulative outflow values for the June 4, 2008 flash flood event at various cumulative rainfall values at a VWC of 0.192 m^3 m^{-3}

	Peak discharge (m^3 s^{-1})	**Difference compared to observed (%)**	**Cumulative outflow (1000 m^3)**	**Difference compared to observed (%)**
Observed	0.93		7.79	
Simulated at a cumulative rainfall of 20 mm	0.76	–18.28	7.41	–5.12
Simulated at a cumulative rainfall of 23 mm	0.92	–1.07	8.93	+14.63
Simulated at a cumulative rainfall of 25 mm	1.40	+50.54	13.53	+73.68

4. Conclusions

4.1. Estimation of soil moisture

VWC as an input data for runoff models is hard to estimate, as it varies greatly in both space and time. However, VWC values vary with the measurement sites in the studied watershed in a predictable way. This consistent behavior is explained by the strong impact of soil properties and topography and the continuous

canopy cover. Thus, for a given, relatively small watershed, a measurement at one particular site would be sufficient for the estimation of soil moisture values at other sites of the watershed, once the relative differences have been measured and calibrated by either an on-site instrument or a single measurement taken by remote-sensing tools, and the measured value could be extrapolated to other parts of the watershed. We believe that regular on-site observations and (preferably automated) soil moisture measurements are essential on the most hazardous watersheds to provide VWC as input parameter for the real-time runoff models.

When regular soil moisture measurements are unavailable, temporal interpolation is required. To achieve appropriate temporal interpolation under forest cover, air temperature (mean daily) and cumulative rainfall time series have to be employed. In our case study, mean temperature showed a good correlation with daily VWC values. However, such correlations need to be developed site-specifically. Additionally, for non-forested portions of the watersheds, relative humidity and wind speed need also to be considered.

In summary, we believe that the accuracy of the estimation of the actual soil moisture content will increase by estimating the soil moisture loss to evaporation. Thus, comprehensive watershed-based meteorological and hydrological monitoring is desirable to reliably predict flood potential. Finally, we conclude that for studies of this type a numerical model need to be applied to generate real-time VWC values.

4.2. Uncertainty in rainfall estimation

Forecast of actual rainfall intensities and cumulative rainfall poses further challenges for the estimation of expected flood levels, as the applied model is highly sensitive to input cumulative precipitation data as well as rainfall intensity. As flash floods are primarily triggered by convective precipitation in orographically diverse areas, spatio-temporal variability in both cumulative precipitation and rainfall intensities may be considerable. To obtain more accurate rainfall prediction and lead time (at least 3 hours), meteorological models and/or radar-based prediction offer appropriate tools. Model predictions may be suitable to delineate the broader area of the potential precipitation event a few hours prior to the actual flood event. For the subsequent refinement of the location, radar observation can be applied. However, in radar observation a considerable error of the measurement of precipitation intensity is inherent.

The present-day radar observations in Hungary have a 2 km spatial and 15-minute temporal resolution. Considering the size of the individual watersheds in the hilly and low-mountain areas of Hungary, we may obtain a sufficient-resolution radar measurements for a given watershed. Estimation of the impact of rainfall is further complicated by rain-on-the-snow events (*Pirkhoffer et al.*, 2007;

Czigány et al., 2009). In summary, close collaboration between the radar data providing meteorological services and the flash flood warning system is necessary in order to obtain sufficient lead time for timely warning of the end users.

4.3. Suitability of HEC-HMS runoff model for numerical simulations

The HEC-HMS is a suitable tool to reproduce large flash flood events on small mountain streams. However, based on the present study, it is probable that both the VWC and rainfall exaggeratedly affect outflow values. Still, we believe that the HEC-HMS would be an appropriate means to determine and predict pronounced flood peaks, and could also be used to determine threshold runoff values, as well as the threshold cumulative precipitation that can trigger floods. We note, however, that when HEC-HMS is used to reproduce high-flow events, significant discrepancy between the simulated and observed values may occur. However, this difference decreases when peak discharge increases.

The applicability of the HEC-HMS model for the development of a nationwide vulnerability map is sufficient, however, in certain aspects, is limited. We believe that the approximate amount (or range) of threshold rainfall can be determined if environmental parameters are available with sufficient accuracy. However, as already pointed out, certain environmental factors may strongly vary in both space and time.

The HEC-HMS tends to be over-sensitive to soil moisture changes. Soil moisture is a highly variable and challenging input parameter for the HEC-HMS runoff model and often represents an average value for large and heterogeneous watersheds. Due to its considerable spatial heterogeneity, the input data may represent a broad range of soil moisture values. In the case of the HEC-HMS, for each watershed, regardless of their area, only a single soil moisture value is provided and, consequently, that does not reflect the above described spatial variance. Multiple model simulations are suitable tools to determine and reproduce field soil moisture values, but simulation errors may become large for future discharge predictions. Our findings suggest that potential discrepancies are further exaggerated by the HEC-HMS model and do not reflect flood level responses appropriately.

Additionally, hydrological models require the downscaling of watershed areas in order to use spatially homogenized input data, such as soil type or canopy cover. However, to approximate these environmental factors at this scale, databases (e.g., soil and land use data) of high resolution are essential. Simultaneously, radar data of at least 15-minute temporal resolution are required to properly model flash flood events. Based on radar predicted precipitation data, available hydrological models (e.g., HEC-HMS) are suitable to predict flood events on small hilly and low-mountain catchments in our study areas and are likely to be capable to form the foundation of a nationwide, flow chart based flash flood warning system.

Acknowledgements—This research was supported by the Jedlik Ányos Foundation (Grant No. NKFP3-00022/2005) and by the Bolyai János Research Scholarschip of the Hungarian Academy of Sciences. The authors are grateful to *Dénes Lóczy* for reviewing the entire manuscript, and to *Ákos Horváth, Gábor Horváth, Roland Vendégh, Gábor Földing, Emil Horváth*, and *Gábor Antal* for their help and contribution to the present work.

References

Cassardo, C., Balsamo, G.P., Cacciamani, C., Cesari, D., Paccagnella, T. and *Pelosini, R.*, 2002: Impact of soil surface moisture initialization on rainfall in a limited area model: a case study of the 1995 South Ticino flash flood. *Hydrol Process 16*, 1301-1317.

Cras, A., Marc, V., and *Travi, Y.*, 2007: Hydrological behaviour of sub-Mediterranean alpine headwater streams in a badlands environment. *J Hydrol 339*, 30-144.

Czigány, S., Pirkhoffer, E. and *Geresdi, I.*, 2009: Environmental impacts of flash floods in Hungary. In *Flood Risk Management: Research and Practice* (eds.: *P. Samuels, S. Huntington, W. Allsop,* and *J. Harrop*). Taylor and Francis Group, London, pp. 1439-1447.

Flint, A.L. and *Flint, L.A.*, 2002: Particle density. In *Methods of Soil Analysis Part 4 Physical Methods* (eds.: *J.H. Dane* and *G.C. Topp*). Soil Science Society of America Inc, Madison, WI.

Gash, J.H.C. and *Morton, A.J.*, 1978: An application of the Rutter model to the estimation of the interception loss from Thetford forest. *J Hydrol* 38, 49-58.

Gash, J.H.C., Wright, I.R. and *Lloyd, C.R.*, 1980: Comparative estimates of interception loss from three coniferous forests in Northern Gemany. *Agr Forest Meteorol* 79, 131-148.

Gaume, E., Bain, V., Bernardara, P., Newinger, O., Barbuc, M., Bateman, A., Blaškovičová, L., Blöschl, G., Borga, M., Dumitrescu, A., Daliakopoulos, I., Garcia, J., Irimescu, A., Kohnova, S., Koutroulis, A., Marchi, L., Matreata, S., Medina, V., Preciso, E., Sempere-Torres, D., Stancalie, G., Szolgay, J. Tsanis, I., Velasco, D., and *Viglione, A.*, 2009: A compilation of data on European flash floods. *J Hydrol 367*, 70-78.

Georgakakos, K.P., 1986: On the design of national, real-time warning systems with capability for site specific flash flood forecasts. *B Am Meteorol Soc 67*, 1233–1239.

Georgakakos, K.P., 2002: Hydrometeorlogical models for real time rainfall and flow forecasting. In *Mathematical Models of Small Watershed Hydrology and Application* (eds.: *V.P. Singh* and *D. Frevert*). Water Resources Publications, LLC, Highlands Ranch, Colorado, pp. 593-655.

Gruntfest, E. and *Ripps, A.*, 2000: Flash floods: Warning and mitigation efforts and prospects. In Floods (ed.: *D.J. Parker*). Vol. 1. Routledge, London, pp. 377-390.

Gyenizse, P., 2009: Geoinformatical studies in Pécs. Studies on physical and social factor affecting the urban development of Pécs. A case study (in Hungarian). *Geographia Pannonica Nova 7*, Publikon Kiadó, Pécs, p. 110.

Gyenizse, P. and *Vass, P.*, 1998: The impact of phyiscal environment on the formation and developemnt of the settlements of the Mecsek Hills (in Hungarian). *Földrajzi Értesítő XLVII*(2), 131-148.

Hillel, D., 1998: *Environmental Soil Physics*. Academic Press, San Diego, CA.

Hizsák, I., 2005: Flooding of the River Kapos (in Hungarian). A Dél-Dunántúli Környezetvédelmi és Vízügyi Igazgatóság, valamint a Dél-Dunántúli Környezetvédelmi, Természetvédelmi és Vízügyi Felügyelőség időszaki lapja, *2*, 6-8.

Horváth, E., 1999: Simulation of extreme hydrological events in unexplored small drainage basins (in Hungarian with English summary). *Vízügyi Közlemények 81*, 486-497.

Huet, Ph., Martin, X., Prime, J.-L., Foin, P., Laurain, Cl., and *Cannard, Ph.*, 2003: Retour d' expériences des crues de septembre 2002 dans les departments du Gard, de l'hérault, du Vaulcluse, des bouches du Rhone, de l'Ardéche et de la Drome. Inspection générale de l'Environnement. Paris, France, 124 p.

Javier, J.R.N., Smith, J.A., Meierdiercks, K.L., Baeck, M.L. and *Miller, A.J.*, 2007: Flash flood forecasting for small urban watersheds in the Baltimore metropolitan region. *Weather Forecast 22*, 1331-1344.

Jessup, S.M. and *DeGaetano, A.T.*, 2008: A statistical comparison of the properties of flash flooding and nonflooding precipitation events in portions of New York and Pennsylvania. *Weather Forecast 23*, 114-130.

Jury, W.A., Gardner, W.R. and *Gardner, W.H.*, 1991: *Soil Physics*, 5th edition. John Wiley and Sons Inc., New York.

Klaasen, W., Bosweld, F. and *de Water, E.*, 1998: Water storage and evaporation as constituents of rainfall interception. *J Hydrol 212/213*, 36-50.

Lefrou, Cl., Martin X., Labarthe, J-P., Varret, J., Maziére, B., Tordjman, R., and *Feunteun, R.*, 2000: Les crues des 11, 12 et 13 novembre 19999, dans les departments de l'Aude, l'Hérault, les Pyrennées Orientales et du Tarn (in French). Inspection générale de l'Environnement. Paris, France, 140 p.

Le Lay, M. and *Saulnier, G.M.*, 2007: Exploring the signature of climate and landscape spatial variabilities in flash flood events: Case of the 8-9 September 2002 Cevennes-Vivarais catastrophic event. *Geophys Res Lett 34*(13) Article No.: L13401.

Link, E.T., Unsworth, M. and *Marks, D.*, 2004: The dynamics of rainfall interception by a seasonal temperate rainforest. *Agr Forest Meteorol 124*, 171-191.

Merz, R., Bloschl, H. and *Parajka, J.*, 2006: Spatio-temporal variability of event runoff coefficients. *J Hydrol 331*, 591-604.

Ogden, F.L. and *Julien, P.Y.*, 2002: CASC2D: a two-dimensional, physically-based, Hortonian hydrologic model. In *Mathematical Models of Small Watershed Hydrology and Applications* (eds.: *V.P. Singh* and *D. Frevert*), pp. 69-112.

Pirkhoffer, E., Czigány, S. and *Geresdi, I.*, 2008: Modeling of flash flood events in a small low-mountain watershed in SW Hungary. In *Proceedings of the joint MAP D-PHASE Scientific Meeting COST 731 mid-term seminar*. Challenges in hydrometeorological forecasting in complex terrain (eds.: *A. Montani, P.P. Alberoni, A. Rossa, M.W. Rotach, A. Buzzi,* and *S. Daviolo*). http://www.smr.arpa.emr.it/dphase-cost/master_proceeding_final.pdf

Pirkhoffer, E., Czigány, S., Geresdi, I. and *Nagyváradi, L.*, 2007: Effect of topography and rainfall pattern on the occurence of flash floods in Hungary. Carpatho-Balkan-Dinaric Conference on Geomorphology, October 24-28, 2007, Pécs, Hungary (poster presentation).

Ranzi, R., Zappa, M. and *Bacchi, B.*, 2007: Hydrological aspects of the Mesoscale Alpine Programme: Findings from field experiments and simulations. *Q J R Meteor Soc 133*, 867-880.

Rutter, A.J., Kershaw, K.A., Robins, P.C. and *Morton, A.J.*, 1971: A predictive model of rainfall interception in forests, 1. Derivation of the model from observations in a plantation of Corsican pine. *Agr Meteorol 9*, 367-384.

Smith, J.A., Baeck, M.L., Morrison, J.E., Sturdevant-Rees, P., Turner-Gillespie, D.F. and *Bates, P.D.*, 2002: The regional hydrology of extreme floods in an urbanizing drainage basin. *J. Hydrometeor 3*, 267-289.

Szilágyi, J., 1954: Extreme flooding of the Által-ér and the Váli víz on June 9, 1953 (in Hungarian). *Vizügyi Közlemények 36*, 169-176.

US Army Corps of Engineers, 2005: *Hydrologic Modeling System HEC-HMS*. User's Manual Version 3.0.0.

Vass, P. 1997: Floods in the headwaters of the Bükkösd Stream (in Hungarian, English summary). In *Földrajzi tanulmányok a pécsi doktoriskolából* I. (eds.: *R. Tésits* and *J. Tóth*). Bornus Nyomda, Pécs, 261-285.

Internet sources

Horváth, Á., 2005: Meteorological aspects of the April 18, 2005 flood event of Mátrakeresztes in Hungarian) http://www.met.hu/pages/vihar 20050418.html, last accessed: April 29, 2008.

IDŐJÁRÁS

Quarterly Journal of the Hungarian Meteorological Service
Vol. 114, No. 1–2, January–June 2010, pp. 101–120

Simulation of accidental release using a coupled transport (TREX) and numerical weather prediction (ALADIN) model

Róbert Mészáros[1*], **Csilla Vincze**[1], and **István Lagzi**[2]

[1]*Department of Meteorology, Eötvös Loránd University*
P.O. Box 32, H-1518 Budapest, Hungary; E-mail: mrobi@nimbus.elte.hu

[2]*Department of Chemical and Biological Engineering, Northwestern University*
2145 Sheridan Road, Evanston, Illinois 60208, U.S.A.

[*]*Corresponding author*

(Manuscript received in final form March 18, 2010)

Abstract—A dispersion model-system called TREX (TRansport–EXchange) was developed at the Eötvös Loránd University (Budapest, Hungary) for modeling the transport and deposition processes of air pollutants originated from either continuous or accidental releases. In this study, a multi-layered, Eulerian version of the TREX model is presented that can simulate transport, transformation, and deposition processes of radionuclides or chemically toxic substances over Central Europe. The TREX model was coupled to the ALADIN mesoscale limited area numerical weather prediction model used by the Hungarian Meteorological Service to predict the path of nuclear contamination in the atmosphere. Two case studies – hypothetical accidents at the Paks Nuclear Power Plant (Paks NPP) – are presented to show how the coupled model can capture the dispersion of radionuclides from a single point source. Another effort of this study is to present a new method, a simple spatial semi-adaptive grid algorithm, which could be an effective tool for accelerating simulations. In this method, model calculations are performed only in the grid cells where concentrations in the previous time step are higher than a user defined threshold concentration. Reduction of the computational time depends on this threshold value, but decreases of more than 60% are found without decreasing the accuracy of the results. The efficiency of this method and a comparative analysis of model estimations with and without this method are also presented in this study.

Key-words: dispersion model, numerical weather prediction model, accidental release, semi-adaptive grid

1. Introduction

The potential for an accident in a nuclear power plant requires continuous developments of atmospheric dispersion models and widespread simulations of an accidental release of radionuclides with these models. Since the accident at the nuclear power plant in Chernobyl in 1986, an increasing demand is observable on the part of countries for construction of sophisticated dispersion models. On the basis of accurate model calculations, the decision makers have to make important arrangements, which can save human lives. In the last two decades, several accidental release models for different spatial and time scales have been developed. Some of these models are based completely or in part on the traditional Gaussian formulation. The DERMA (Danish Emergency Response Model of the Atmosphere) model uses a hybrid stochastic particle-puff diffusion description (*Sørensen et al.*, 1998, 2007). In the horizontal, a Gaussian distribution of the concentration is assumed for each puff. For puffs inside the boundary layer, an assumption of complete mixing is applied in the vertical, while for puffs above the boundary layer, a Gaussian distribution is used. The RIMPUFF (Risø Mesoscale PUFF) model (*Mikkelsen et al.*, 1997) was applied for example, in the study of *Gultureanu et al.* (2000). The Hungarian Meteorological Service has also adapted the RIMPUFF model for mesoscale simulations of a plume. The NAME model of the UK MET Office (the British Meteorological Service) and the Norwegian SNAP model apply Lagrangian description which simulates numerous particles that provide facility to take account of the effect of the fluctuation in the meteorological data (*Ryall* and *Maryon*, 1998; *Saltbones et al.*, 1998; *Bartnicki et al.*, 2003; *Jones et al.*, 2007). The Austrian emergency response modeling system, TAMOS (*Pechinger et al.*, 2001) is based on the Lagrangian particle dispersion model FLEXPART (*Stohl et al.*, 1998, 2005; *Srinivas et al.*, 2006) and the trajectory model FLEXTRA (*Baumann* and *Stohl*, 1997; *Stohl* and *Wotawa*, 1997). The Hungarian Meteorological Service has also adapted FLEXRTA/FLEXPART for calculating the long-range transport of particles from a nuclear power plant.

The Lagrangian models have the advantage that they can afford to use high spatial resolution, although they rely on the interpolation of meteorological data. Their potential disadvantages are that in some cases they neglect important physical processes and often experience problems when strongly diverging flows lead to uncertainties in long-range trajectories. In contrast to the Lagrangian approach, the Eulerian models use grid based methods and have the advantage that they may take into account fully 3D descriptions of the meteorological fields rather than single trajectories. An Eulerian dispersion model, MEDIA was joined to the emergency response system of the Hungarian Meteorological Service (*Ferenczi* and *Ihász*, 2003). However, Eulerian models show difficulty in resolving steep gradients, when fixed meshes are used. This causes particular problems for resolving dispersion from a single point source,

which creates very large gradients close to the point of release. For a coarse Eulerian mesh, the release is immediately averaged into a large area, which smears out the steep gradients and creates a large amount of numerical diffusion (*Lagzi et al.*, 2004). Therefore, in some cases a mixed approach is used. In these models (e.g.: DREAM – Danish Rimpuff and Eulerian Accidental release Model, or MATCH – Multiscale Atmospheric Transport and Chemistry model), close to the source, a Lagrangian description is used, while an Eulerian model calculates the long-range transport (*Langnera et al.*, 1998; *Brandt et al.*, 2000, 2002). The accidental release models are usually coupled with a nuclear decision-support system, e.g., the DERMA model has become interfaced with the Accident Reporting and Guidance Operational System – ARGOS (*Baklanov et al.*, 2006), or RIMPUFF was jointed to RODOS (Realtime Online DecisiOn Support) system (*Ehrhardt et al.*, 1997; *Mikkelsen et al.*, 1997).

The European real time modeling exercise RTMOD was developed to the comparison of long-range transport and dispersion models and support of decision making. It gathers the results of more than 20 models, and it provides not only one-to-one model comparison but ensemble dispersion forecasts (*Bellasio et al.*, 1999; *Galmarini et al.*, 2001, 2004).

Although several different kinds of dispersion models are available, further and continuous developments of simulation techniques are required. Based on the experience of our previous investigations (*Lagzi et al.*, 2001, 2004, 2006; *Lovas et al.*, 2006; *Mészáros et al.*, 2006; *Dombóvári et al.*, 2008), a newly developed Eulerian dispersion model is presented in this study. Model simulations and tests were carried out to estimate the long-range transport of radionuclides from a nuclear power plant (Paks NPP).

Dispersion simulations must have a high degree of accuracy and must be achieved faster than real time to use it for decision making strategy. There are several well defined methods and techniques to decrease the calculation time of the applications. One useful solution is the parallelization of source code and the application of the supercomputers, clusters, and grid systems to solve these tasks (*Dabdub* and *Seinfeld*, 1996; *Martin et al.*, 1999; *Larson* and *Nasstrom*, 2002; *Alexandrov et al.*, 2004; *Dimov et al.*, 2004; *Martín et al.*, 2004; *Ostromsky et al.*, 2005; *Singh et al.*, 2006). A new method for parallelization using newly developed video-card in CUDA environment is presented in *Molnár et al.* (2010). On the other hand, there are several numerical models, in which adaptive gridding techniques have been implemented (*Lagzi et al.*, 2004, 2006, 2009; *Zegeling* and *Kok*, 2004). The numerical algorithm automatically places a finer resolution grid in regions characterized by high spatial numerical errors. Therefore, the fine resolution grid follows the plume of the air pollutants.

In this study, a new semi-adaptive calculation method was introduced to reduce the CPU time for simulating dispersion processes. Using this simple algorithm, faster simulations are achievable due to decreasing of the active cells determined by a user-defined critical (or threshold) concentration. Numerical

simulations are performed only in these active cells, where the concentration of air pollutant in the previous time step exceeded the predefined level. The effectiveness of this method (how fast and precise the model) depends on this critical value. Very large critical concentration may cause uncertainty in the simulation, and very low critical concentration cannot call forth effective acceleration. However, the optimal choice of the critical value decreases the computational time without decreasing the quality of the results.

2. *The TREX-Euler model*

2.1. Model description

As a part of TREX model-system, developed at the Eötvös Loránd University, Hungary, the TREX-Euler is a multi-layered, Eulerian passive tracer dispersion model to describe transport and deposition of air pollutants over the Central European region. The model was developed in a flexible framework, and therefore, can simulate both single source accidental releases and photochemical air pollution. In this study we only focus on the dispersion of radionuclides from a nuclear power plant. All required meteorological data were obtained from the ALADIN mesoscale numerical weather prediction model (*Horányi et al.*, 1996, 2006). In the TREX-Euler model, horizontal dispersion of radionuclides is described within a regular Eulerian grid framework. The vertical mixing is parameterized using K-theory. Dry and wet deposition and also the transformation of radionuclides by nuclear decay are considered in each grid cell. The simulation of the dispersion is based on the following atmospheric diffusion equation:

$$\frac{\partial \mathbf{c}_i}{\partial t} = -\underline{\mathbf{V}}\nabla \mathbf{c}_i + \nabla \underline{\underline{\mathbf{K}}} \nabla \mathbf{c}_i - (k_{c\,i} + k_{d\,i} + k_{w\,i})\mathbf{c}_i + \mathbf{E}_i, \tag{1}$$

which describes the advection, diffusion, and source and sinks of the radionuclides. In the equation $\mathbf{c}_i$ is the concentration of the ith radionuclides, $\underline{\mathbf{V}}$ is the three-dimensional velocity vector, $\underline{\underline{\mathbf{K}}}$ is the tensor of turbulent diffusions coefficient, $k_{c\,i}$ is the coefficient of radioactive decay, $k_{d\,i}$ and $k_{w\,i}$ are the dry and wet deposition coefficients, and $\mathbf{E}_i$ is the emission of radionuclides, respectively.

This partial differential equation has been solved by 'method of lines' technique. The two main components of the method of lines are spatial discretization followed by time integration. A second-order central difference stencil and upwind approximation are used for spatial discretization of the turbulent diffusion and advection. The model uses the forward Euler method to solve the obtained original ordinary differential equations. However, this

method is robust only with the appropriately chosen grid spacing (Δx) and time step (Δt). An accidental release model must be precise and fast at the same time. It is difficult to achieve both, because the more accurate and complex the model is the more computational time is required. The accuracy and the CPU time depend on model algorithms and also on the spatial and time resolution. For example, a shorter time step increases the accuracy of solution, at the same time, the computational efficiency decreases. To preserve the stability of the solution, the following conditions must be realized between the Δx spatial resolution and Δt time step for advection and diffusion, respectively:

$$\frac{|\mathbf{V}|\Delta t}{\Delta x} \leq 1, \tag{2}$$

$$\frac{2K\Delta t}{\Delta x^2} \leq 1, \tag{3}$$

where $|\mathbf{V}|$ is the amplitude of wind velocity vector and K is the horizontal turbulent diffusion coefficient. The spatial resolution is same as the resolution of the meteorological data from the ALADIN model, therefore, the model calculation was discretized on an equidistant rectangular grid with resolution of 0.0375×0.025 degrees (~ 2.5 km × 2.5 km). For this spatial resolution the time step Δt was set to 10 s, which assures the stability of solution.

In the vertical direction the model contains 32 levels and the resolution increases exponentially with height. Each vertical level was determined with the barometric formula (assuming isothermal layers) in a hypothetical air column, where the surface pressure is equal to 1013.25 hPa. Up to 200 m above the surface, the column was divided into 12 levels with equidistant pressure difference (197 Pa in isothermal layers), up to 3000 m the layers were thicker with higher pressure difference (1514 Pa), and these two resolutions were joined together. Two additional levels were added to the bottom and the top of column to ensure the boundary conditions.

The horizontal turbulent diffusion coefficients (K_x and K_y) were considered with a constant value equal to 10^4 m^2 s^{-1} (*Brandt*, 1998). In regional scale, in the function of the wind speed, the effect of the advection on dispersion is one or two orders of magnitude higher than the effect of the horizontal turbulent diffusion. Vertical transport was parameterized using the K-theory. The vertical turbulent diffusion coefficient (K_z) at a given level z has spatial and temporal variation:

$$K_z = \frac{k u_* z}{\Phi_T}\left(1 - \frac{z}{H_{mix}}\right)^2, \tag{4}$$

where k is von Kármán's constant taken to be 0.41, u_* is the friction velocity, z is the height above the surface, Φ_T is the similarity function for heat, and H_{mix} is the height of the mixing layer. Similarity functions for stable and unstable stratifications were used after *Arya* (1988). The value of H_{mix} was obtained from ALADIN model. The friction velocity was calculated by the following equation:

$$u_* = \frac{ku}{\log\frac{z_{ref}}{z_0} - \Psi_m}, \tag{5}$$

where z_{ref}, u, z_0, and Ψ_m are the reference height, wind velocity at this height, roughness length, and integral form of universal stability correction functions for the momentum, respectively.

Universal function in stable stratification was estimated after *Businger et al.* (1971) in case of $z_{ref} / L \leq 0.5$, and an empirical relationship of *Holtslag* and *de Bruin* (1988) was used in other cases, where L is the Monin-Obukhov length. In case of unstable stratification, the stability function was based on *Paulson* (1970). The stratification of the layer was determined iteratively by the Monin-Obukhov length:

$$L = -\frac{Tu_*^3}{\frac{gk}{\rho c_p}H}, \tag{6}$$

where T is the air temperature at 2 m (data from ALADIN model), g is the acceleration of gravity, ρ is the air density, c_p is the specific heat at constant pressure, and H is the sensible heat flux. In this study, this latter term was calculated after *Brandt* (1998).

The vertical dispersion was calculated with a Lagrangian stochastic, random displacement method. In this method, the particles, which are in a cell, are divided into a number of groups or packages (10 packages in this study) with equal number of particles, and the 'packages' are moving together. The vertical displacement of a package l_n is calculated as follows:

$$l_n = R\sqrt{K_z(n)\Delta t}, \tag{7}$$

where R is a random number with normal distribution and $K_z(n)$ is the vertical turbulent diffusion coefficient at the nst level (z_n). During a time step, a particle package can move only into the adjacent cells (the direction of the movement depends on the sign of the l_n). The ith (i = 1 to 10 in this study) package from the level

z_n gets into the level z_{n+1} (upward) if $l_n(i)$ is positive and $l_n(i) > (z_{n+1} - z_n)/2$, and into the level z_{n-1} (downward) if $l_n(i)$ negative and $-l_n(i) > (z_n - z_{n-1})/2$. If the condition is not met, the ith package stays at the level z_n. From the top and bottom levels the vertical transport is one way.

During current model simulations, the dispersion of a radionuclide – ^{131}I – was considered. The emission was assumed to be from the Paks NPP (46°34'N, 18°51'E) as a point source. The radioactive decay and the change of activity of ^{131}I were simulated. Chemical reactions were not considered. However, the structure of the program allows simultaneous simulations of the dispersion of several hundred isotopes, taking into account all radioactive decays and reactions.

The deposition is handled as a first-order reaction, which decreases the amount of the radionuclide in the atmosphere. Dry deposition of radionuclides from the bottom layer is parameterized by a constant deposition coefficient (3×10^{-6} s^{-1} for ^{131}I) based on *Baklanov* and *Sørensen* (2001). The wet deposition velocity was parameterized using a simple scheme to calculate the wet deposition coefficient k_w based on the relative humidity RH with the following parameterization (*Pudykiewicz*, 1989, 1991; *Brandt*, 1998):

$$k_w = 0, \quad \text{if } RH < RH_t$$
$$k_w = 3.5\times10^{-5}\left(\frac{RH - RH_t}{RH_s - RH_t}\right), \quad \text{if } RH \geq RH_t, \tag{8}$$

where RH is the current relative humidity, RH_s is the saturation relative humidity (100%), and RH_t is a threshold value of relative humidity (80%); above which the wet deposition of radionuclides from the bottom layer occurs. The radioactive decay is calculated by a constant rate: $k_c = \log 2 / t_{1/2}$, where the radioactive half life ($t_{1/2}$) of ^{131}I is 6.948×10^5 s.

During the model computations, each process – horizontal spreading (advection and diffusion), vertical dispersion, source and sinks terms (deposition, radioactive decay, and emission processes) – are calculated separately using the operator-splitting approach. The model was coupled with the ALADIN mesoscale limited area numerical weather prediction model used by the Hungarian Meteorological Service.

2.2. The semi-adaptive method

In a previous investigation (*Lagzi et al.*, 2006), an adaptive grid model has been presented to describe the formation and transformation of air pollutants based on triangular unstructured grids. This technique is based on the calculation of

spatial error estimations. The algorithm can then choose to refine the grid in regions of high spatial error by comparison with a user defined tolerance for radionuclides. Therefore, depending on the numerical error, the spatial resolution was varied. In this study, another effective way is presented to reduce the CPU time of model calculations. The model applies a semi-adaptive method to perform faster simulations. In contrast to the adaptive method, in the newly introduced semi-adaptive method, the spatial resolution remains constant but a concentration test is applied to determine if model calculations are to be performed in particular grid cells.

The main concept of the semi-adaptive method is that the model calculation is performed only in the grid cells, where a predefined condition is met. This condition is that the concentrations in the grid point in the previous time step must be greater than a user defined critical concentration. By this method, the accuracy and the CPU time depend on the critical concentration and the simulation period. At the beginning of the simulation, immediately after the accidental release, the efficiency of the acceleration is higher, since model calculations are performed only in a few grid points. With the development of the plume, the efficiency of the method decreases as the number of affected grid points increases. Through the choice of the critical concentration, the CPU time and the error of the method can be adjusted. By increasing the critical concentration, the CPU time can be significantly decreased, however, the calculation error increases.

3. Results and discussion

3.1. Modeling accidental release

The features of the transport model and the efficiency of the semi-adaptive method are illustrated by two simulations of a hypothetical nuclear accident in the Paks Nuclear Power Plant, in the central part of Hungary (46°34'N, 18°51'E). During the simulations, ^{131}I isotope was emitted into the atmosphere from the point source to the given grid cell with the rate of 10^{10} cm^{-3} s^{-1} between 00 and 12 UTC on December 2, 2005 and March 24, 2006. Meteorological fields (wind speed, wind direction, temperature, relative humidity, cloudiness, and mixing layer height) were obtained from ALADIN weather prediction model. Simulations were performed for 48 hours after the hypothetical accidents. The modeled area covered the region around Hungary (10.85°–25.1°E, 41.3°–52°N) and contained 8640 grid cells on each 32 vertical levels.

Fig. 1 depicts the horizontal structures of the radioactive plume originating from the Paks Nuclear Power Plant at the emission level (120 m above the surface), 12, 24, 36, and 48 hours after a hypothetical accident on December 2, 2005. The plume structure is predominantly determined by the wind field. However, other meteorological parameters can also influence the dispersion

(e.g., vertical temperature gradient, planetary boundary layer height, etc.). During this simulation period, the Carpathian Basin was affected by a Mediterranean cyclone and a warm front caused rainy weather. The variable wind field caused the plume to spread in south, south-western direction in the first few hours of the simulation, but as the wind direction changed, the radioactive cloud had moved in eastern, north-eastern, and finally, northern direction. Due to this variable wind field, a wide region (including all of Hungary) was affected by the plume. However, as the concentration was highest after the release, when the plume had moved in southern direction, the highest cumulative dry deposition of ^{131}I to the surface appeared to the south of the point source (*Fig. 2a*). The cumulative wet deposition (*Fig. 2b*) was also significant, because more than 15 mm precipitation occurred in some parts of central Hungary during two days after the hypothetical accident. Highest wet deposition was found around the point source (the maximum was higher than 10^9 cm^{-2}), where the largest amount of precipitation was fallen during 48 hours.

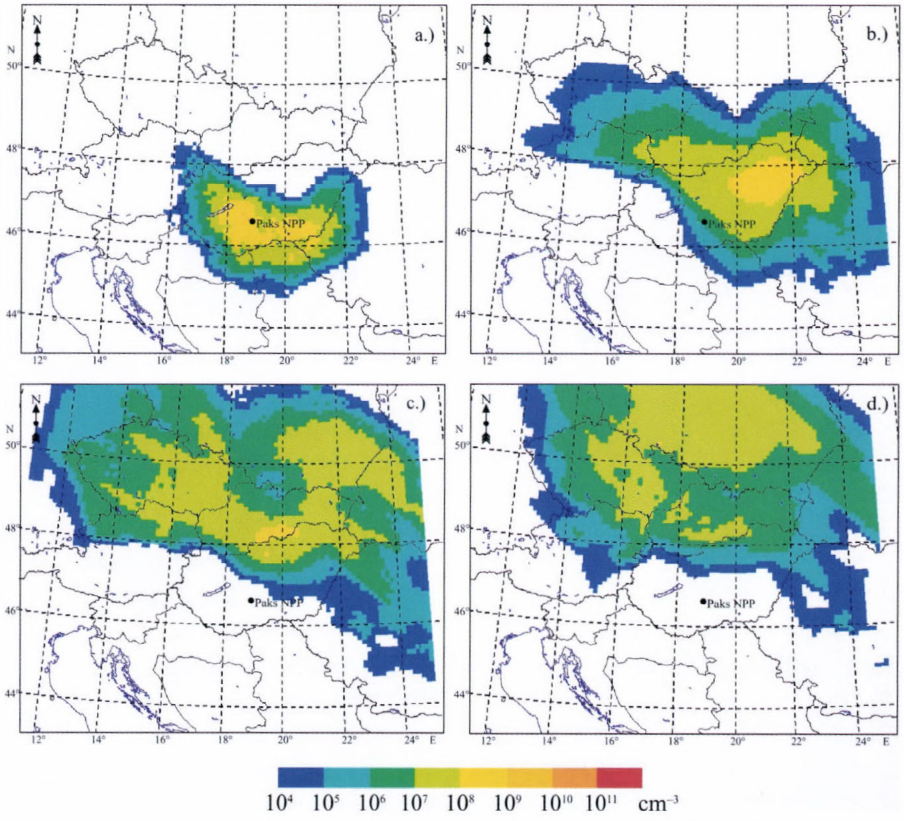

Fig. 1. Horizontal distribution map of ^{131}I concentration at 120 m above the surface, (a) 12, (b) 24, (c) 36, and (d) 48 hours after the hypothetical accident at 00 UTC, December 2, 2005.

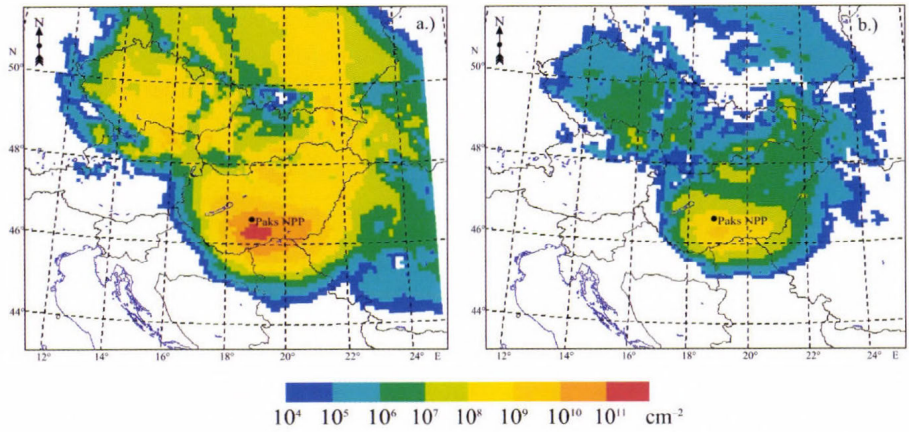

Fig. 2. Horizontal distribution map of cumulative (a) dry and (b) wet deposition of ^{131}I to the surface, 48 hours after the hypothetical accident at 00 UTC, December 2, 2005.

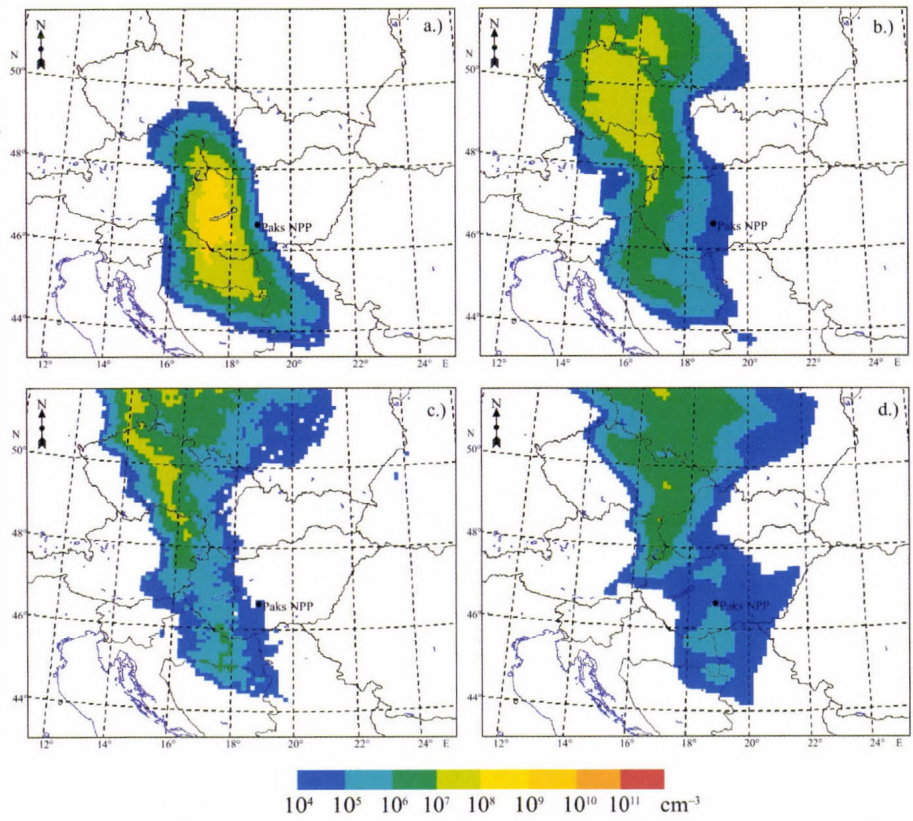

Fig. 3. Horizontal distribution map of ^{131}I concentration at 120 m above the surface, (a) 12, (b) 24, (c) 36, and (d) 48 hours after the hypothetical accident at 00 UTC, March 24, 2006.

During the period of the second simulation (March 24–25, 2006), an anticyclone was located over Central Europe, which caused sunny, dry weather. In the first 12 hours of the simulation, the plume was spread in a wide south-north belt, which had moved to the North and finally to the East (*Fig. 3*). Significant cumulative dry deposition was observed in south-northern axes (*Fig. 4a*), however, wet deposition (*Fig. 4b*) was very minor due to the dry weather conditions.

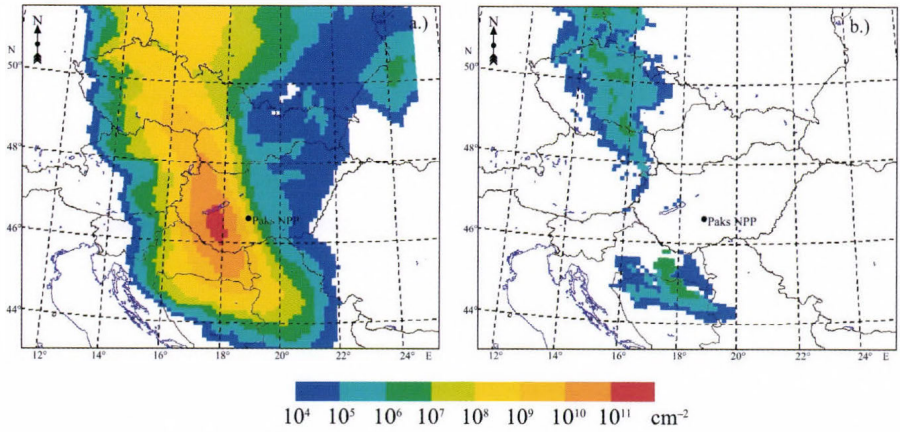

Fig. 4. Horizontal distribution map of cumulative (a) dry and (b) wet deposition of ^{131}I to the surface, 48 hours after the hypothetical accident at 00 UTC, March 24, 2006.

3.2. Efficiency of the semi-adaptive method

Efficiency of the semi-adaptive method is illustrated by running a set of simulations with the same meteorological and emission conditions used in the standard model runs described above, but during these simulations, the calculations have only been made on grid columns (on active cells), when the concentration of ^{131}I, at least at one grid cell in any of the 32 layers of a given grid column, exceeds a previously defined critical concentration. *Fig. 5* shows the number of active cells as a function of time, and critical concentrations. The higher the critical concentration is, the lower the number of active cells are. By increasing this critical concentration, higher acceleration can be achieved, since fewer calculations must be performed over the domain. In *Fig. 6*, the relative CPU time and the ratio of active cells can be seen as a function of the critical concentration for a 48-hour simulation (00 UTC, March 24, 2006 – 00 UTC, March 26, 2006). In case of relative CPU time, 1 refers to the CPU time of the simulation without the semi-adaptive method. The ratio of active cells is the maximum number of calculated horizontal grid cells during the whole simulation divided by the total number of horizontal grid cells 8640 (96×90). One can see that both the ratio of active cells and the relative CPU time

decreased with the increase of the critical concentration, but the size of the decreases are different. For lower critical concentrations (up to 10^7 cm^{-3}), the relative CPU time decreases rather than the maximum number of active cells during the simulation. The reason for this difference is that the number of active cells increases during the simulation. Accordingly, the acceleration is most effective after starting the simulation and decreases with time as the number of active cells increases.

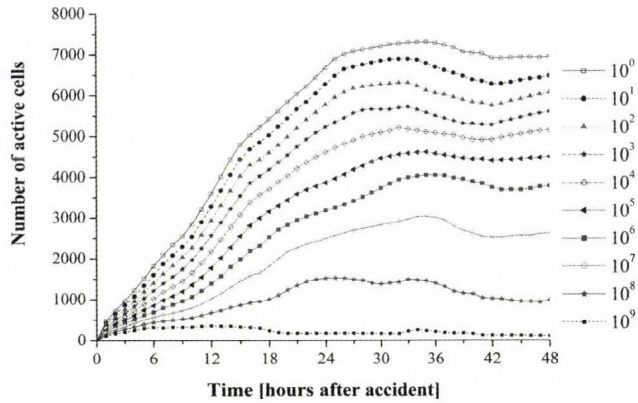

Fig. 5. Number of active cells during a 48-hour simulation after the hypothetical accident at 00 UTC, March 24, 2006 with different critical concentrations (in cm^{-3}).

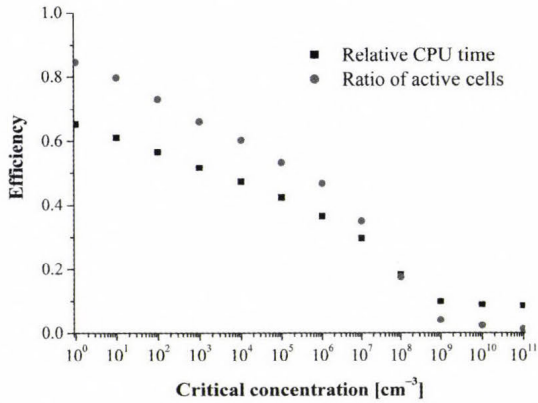

Fig. 6. Relative CPU time and ratio of active cells as a function of critical concentration. Test data: March 24–25, 2006.

In *Fig. 6*, the ratio of maximum number of active cells are presented, however, the relative CPU time corresponds to the whole period. In case of higher critical concentrations (from 10^9 cm^{-3}), with increase of the critical concentration the number of active cells slightly increases further, but it seems

that there is no further significant changes in the effective CPU time. This result suggests that there is a possible limit of the acceleration and any further increase of critical concentration will not increase the efficiency of the simulation. We should note that the CPU time also contains the time of unpacking, reading, and repacking of all meteorological datasets from the ALADIN model output files, and this time cannot be shortened by the semi-adaptive method.

The decrease of the simulation time of an accidental release model is crucially important and, at the same time, the method applied for the acceleration must be reliable. In *Fig. 7*, the horizontal distribution of the plume at the surface can be seen after 12 hours of a hypothetical accident using different critical concentrations. It appears that there is good agreement between maps with no critical concentration and lower critical concentrations (10^4–10^6 cm^{-3}). The polluted area and region with the highest concentrations can be captured similarly in all cases. However, some differences appear in the distribution, and these differences increase with increases in the critical value. For higher critical concentrations (10^7–10^9 cm^{-3}) the differences became significant, and only the most polluted area appears in the maps. Additionally, in some part of these regions, higher concentrations can be found as in case of standard model runs without the semi-adaptive method. Nevertheless, simulations using high critical concentrations can rapidly provide information about the direction of plume transport.

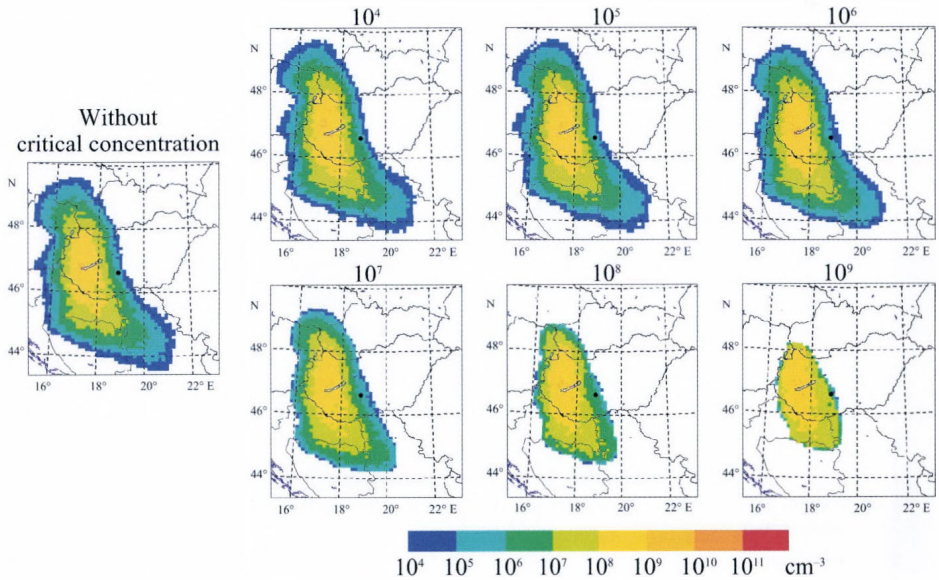

Fig. 7. Horizontal distribution map of ^{131}I concentration at the surface 12 hours after the hypothetical accident at 00 UTC, March 24, 2006 without and with different critical concentrations (in cm^{-3}). Same input meteorological and emission data were used in all cases. The black point denotes Paks NPP.

The differences depend not only on the choice of critical concentration but also on the simulation time. *Figs. 8a* and *b* present the relative differences of average and maximum concentrations of ^{131}I at the surface calculated without (c_1) and with (c_2) a critical concentration.

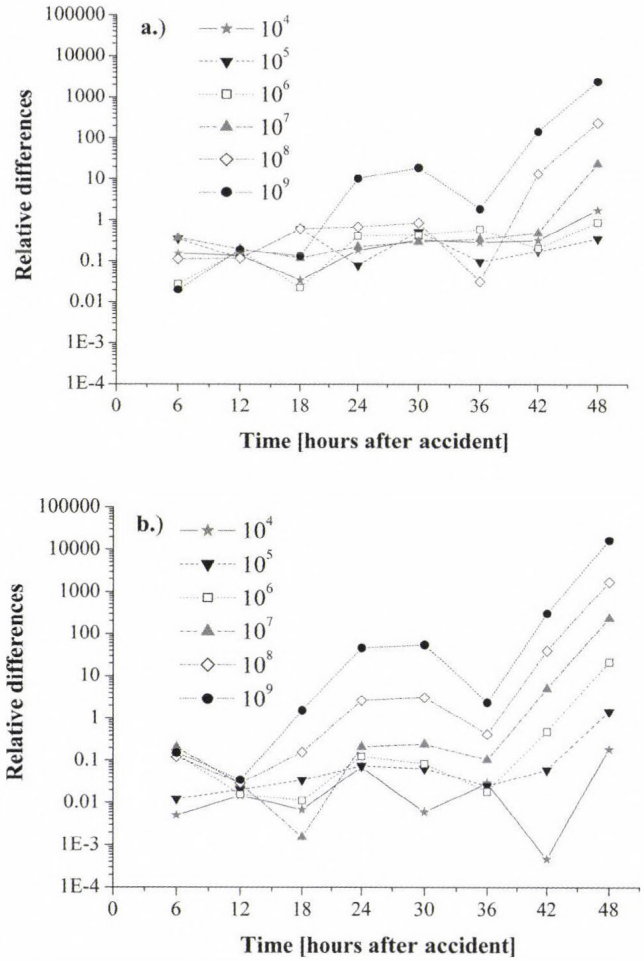

Fig. 8. (a) Relative differences of average ^{131}I concentration at the surface during a 48-hour simulation after the hypothetical accident at 00 UTC, March 24, 2006 in 6-hour time step. Values are calculated over the whole domain with and without semi-adaptive method with different critical concentrations (in cm^{-3}). (b) Same as Fig. 8a, but for maximum values.

The relative difference was calculated as $diff = |c_1 - c_2| / c_1$. Relative differences of average values (*Fig. 8a*) varied around 0.1 in general, but there are greater differences in case of 10^9 cm^{-3} critical concentration in the first

simulation day. From the 36th hour of the simulation, the differences became larger and the highest differences were found in case of higher critical concentrations. It is particularly noticeable, that differences decreased at 12 and 36 hours after the hypothetical accident (at 00 UTC). This is because of more turbulent conditions during daytime. Relative differences of maximum values (*Fig. 8b*) show greater variability. Nevertheless, if the critical concentration remains lower than 10^8 cm^{-3} till the 36th hour of the simulation, model estimation gives similar maximum values (the relative differences are small). It should be noted, that for a purpose of a shorter (for 12 hours) prediction of the maximum value, higher critical concentrations (10^8–10^9 cm^{-3}) should also provide appropriate results.

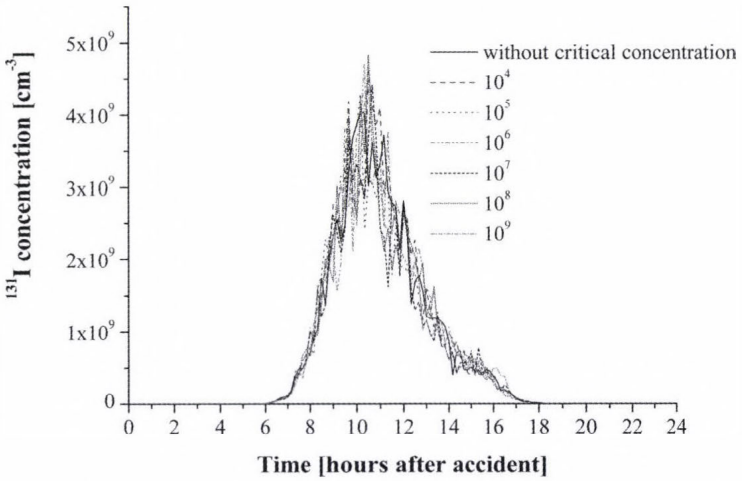

Fig. 9. Temporal variation of ^{131}I concentration at the surface over the city of Veszprém (47.1°N, 17.92°E) after the hypothetical accident at Paks NPP at 00 UTC, March 24, 2006. Values are calculated without and with different critical concentrations (in cm^{-3}).

The semi-adaptive method was also tested over given points. *Fig. 9* shows the temporal variations of ^{131}I concentration at the surface in Veszprém (47.1°N, 17.92°E, about 90 km to the NW direction of the point source) after a hypothetical accident in Paks NPP at 00 UTC, March 24, 2006, calculated with different critical concentrations. The plume passed over the city in the same interval, from 06 UTC to 18 UTC, and maximum concentrations appeared between 10 and 11 UTC in case of all different model runs with different critical concentrations. In the time series, about 20% variations on average can be found between values calculated with and without the semi-adaptive method. However, these differences are mainly caused by the stochastic calculation of the vertical transport term and not due to the different critical concentrations. This can be seen in *Fig. 10,* where two standard model runs without the semi-

adaptive method are compared. In spite of that in both cases the same meteorological and emission input fields were used, similar differences in concentration values can be seen similarly to *Fig. 9*, where model runs with different critical concentrations are presented. The differences between any two simulations should decrease with the use of more 'packages' in stochastic diffusion. These results also underline that the semi-adaptive method should be an effective way to accelerate the calculations.

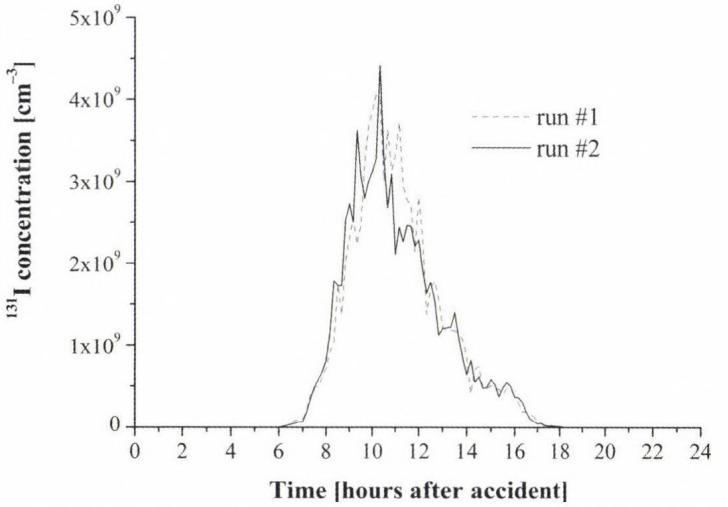

Fig. 10. Same as Fig. 9, but both time series were calculated without semi-adaptive method.

4. Conclusion

Modeling of the accidental release of radionuclides or highly toxic air pollutants requires fast and precise model estimations. In this study an Eulerian version of the TREX transport-exchange model is presented. We have also provided here a new method to accelerate the simulation, which is crucially important if a nuclear accident occurs, as we can gain time to prepare for the effects of the plume. With the semi-adaptive method, the efficiency of model simulations could be increased.

Two test simulations have been carried out for 48 hour periods. In case of each simulation, a hypothetical accident was assumed at the Paks Nuclear Power Plant, and the transport and deposition processes of ^{131}I have been estimated over a domain of $96 \times 90 \times 32$ grid cells. All meteorological fields for the simulations were obtained from the ALADIN numerical weather prediction model. Concentration fields, dry and wet deposition have been presented for two different meteorological conditions.

To apply the semi-adaptive method, the model simulations have been performed only on grid columns, where the concentration exceeds a predefined level in any of 32 layers in the column. The more efficient the method is, the most inactive cells are there, so the model became faster than without the semi-adaptive method, because less calculation is needed. The calculation time decreases with increasing critical concentration.

Based on our results, it seems that the semi-adaptive method could be an appropriate tool for accelerating the simulations. With high critical concentration, 10 times acceleration could be achieved compared to simulation without semi-adaptive method. However, there are some limits to this process. The higher the critical concentration is, the greater the differences are in the structure of the plume and in the estimated concentrations compared to the results obtained from normal simulation. The agreements between two cases are better in earlier part of simulation and generally decline with time, but more intense turbulence in daytime should be diminish the differences either during the latter part of simulation. Although high critical values (more than 10^7 cm^{-3} – compared to the emission rate used in this study) may cause large differences in simulated concentrations, it also should be usable for a fast, rough estimate for the direction of travel of the plume and the order of magnitude of the concentration. Determination of the critical concentration plays an important role of this method in decision support. It should be noted that further investigations should precede the implementation and any operational use of the semi-adaptive method in simulation of accidental release. Results of this study contribute to the further development of TREX dispersion model system.

Acknowledgements—The authors would like to thank *András Horányi* and *László Kullmann* for the ALADIN data. This research is supported by Hungarian Research Found (OTKA K68253, OTKA K81933 and OTKA K81975) and by SEE-GRID-SCI (SEE-GRID eInfrastructure for regional eScience) project, funded by the European Commission through the contract nr RI-211338.

References

Alexandrov, V.N., Owczarz, W., Thomson, P.G. and *Zlatev, Z.*, 2004: Parallel runs of a large air pollution model on a grid of Sun computers. *Math Comput Simulat 65,* 557-577.

Arya, S.P., 1988: Introduction to Micrometeorology. Academic Press, INC, San Diego. pp. 307.

Baklanov, A. and *Sørensen, J.H.*, 2001: Parameterisation of Radionuclide Deposition in Atmospheric Long-Range Transport Modelling. *Phys Chem Earth (B) 26*, 787-799.

Baklanov, A., Sørensen, J.H., Hoe, S.C. and *Amstrup, B.*, 2006: Urban meteorological modelling for nuclear emergency preparedness. *J Environ Radioactiv 85*, 154-170.

Bartnicki, J., Saltbones, J. and *Foss, A.*, 2003: Performance of the SNAP model in an ENSEMBLE exercise of simulating real-time dispersion from a nuclear accident. *Int J Environ Pollut 20*, 1-6, 22-32.

Baumann, K. and *Stohl, A.*, 1997: Validation of a long-range trajectory model using gas balloon tracks from the Gordon Bennett Cup 95. *J Appl Meteor 36*, 711-720.

Bellasio, R., Bianconi, R., Graziani, G. and *Mosca, S.*, 1999: RTMOD: an Internet based system to analyse the predictions of long-range atmospheric dispersion models. *Computers & Goesciences 25*, 819-833.

Brandt, J., 1998: Modelling transport, dispersion and deposition of passive tracers from accidental releases. PhD thesis. Ministry of Environment and Energy National Environmental Research institute and Ministry of Research and Information Technology Risø National Laboratory, Denmark, Roskilde. pp 307.

Brandt, J., Christensen, J.H., Frohn, L.M. and *Zlatev, Z.,* 2000: Numerical modelling of transport, dispersion, and deposition – validation against ETEX-1, ETEX-2 and Chernobyl. *Environ Model Softw 15,* 521-531.

Brandt, J., Christensen, J.H. and *Frohn, L.M.,* 2002: Modelling transport and deposition of caesium and iodine from the Chernobyl accident using the DREAM model. *Atmosph Chem and Phys,* 397-417.

Businger, J.A., Wyngaard, J.C., Izumi, Y. and *Bradley, E.F.,* 1971: Flux-profile relationships in the atmospheric surface layer. *J Atmos Sci 28,* 181-189.

Dabdub, D. and *Seinfeld, J.H.,* 1996: Parallel computation in atmospheric chemical modelling. *Parallel Comput 22,* 111-130.

Dimov, I., Georgiev, K., Ostromsky, T. and *Zlatev, Z.,* 2004: Computational challenges in the numerical treatment of large air pollution models. *Ecol Model 179,* 187-203.

Dombvári, P., Ranga, T., Nényei, Á., Bujtás, T., Kovács, T., Jobbágy, V., Vincze, Cs. and *Molnár, F.,* 2008: Új terjedésszámító szoftver fejlesztése és bevezetése a Paksi Atomerőműnél. (in Hungarian) *Sugárvédelem I. 1,* 30-36.

Ehrhardt, J., Brown, J., French, S., Kelly, G.N., Mikkelsen, T. and *Müller, H.,* 1997: RODOS: Decision-making support for off-site emergency managment after nuclear accidents. *Kerntechnik 62,* 122-128.

Ferenczi, Z. and *Ihász, I.,* 2003: Validation of the Eulerian dispersion model MEDIA at the Hungarian Meteorological Service. *Időjárás 107,* 115-132.

Galmarini, S., Bianconi, R., Bellasio, R. and *Graziani, G.,* 2001: Forecasting the consequences of accidental releases of radionuclides in the atmosphere from ensemble dispersion modelling. *J Environ Radioactiv 57,* 203-219.

Galmarini, S., Bianconi, R., Klug, W., Mikkelsen, T., Addis, R., Andronopoulos, S., Astrup, P., Baklanov, A., Bartniki, J., Bartzis, J.C., Bellasio, R., Bompay, F., Buckley, R., Bouzom, M., Champion, H., D'Amours, R., Davakis, E., Eleveld, H., Geertsema, G.T., Glaabl, H., Kollax, M., Ilvonen, M., Manning, A., Pechinger, U., Persson, C., Polreich, E., Potemski, S., Prodanova, M., Saltbones, J., Slaperj, H., Sofiev, M.A., Syrakov, D., Sørensen, J.H., Van der Auwera, L., Valkama, I. and *Zelazny, R.,* 2004: Ensemble dispersion forecasting – Part I: concept, approach and indicators. *Atmos Environ 38,* 4607-4617.

Gultureanu, D., Gultureanu, B., Mikkelsen, T., Thykier-Nielsen, S. and *Matenciuc, M.,* 2000: Air pollution studies for the Romanian nuclear power plant – Cernavoda based on the RIMPUFF dispersion model. *Air Pollution Modeling and Its Applications XIII Book Series: NATO challenges of modern society 13,* 779-780.

Holtslag, A.A.M. and *De Bruin, H.A.R.,* 1988: Applied Modeling of the Nighttime Surface Energy Balance over Land. *J Appl Meteorol 27,* 689-704.

Horányi, A., Ihász, I., and *Radnóti, G.,* 1996: ARPEGE/ALADIN: A numerical weather predicition model for Central-Europe with the participation of the Hungarian Meteorological Service. *Időjárás 100,* 277-300.

Horányi, A., Kertész, S., Kullmann, L. and *Radnóti, G.,* 2006: The ARPEGE/ALADIN mesoscale numerical modeling system and its application at the Hungarian Meteorological Service. *Időjárás 110,* 203-227.

Jones, A., Thomson, D., Hort, M. and *Devenish, B.,* 2007: The UK Met Office's next-generation atmospheric dispersion model, NAME III. *Air Pollution Modeling and Its Applications XVII Book Series: NATO challenges of modern society 17,* 580-589.

Lagzi, I., Tomlin, A.S., Turányi, T., Haszpra, L., Mészáros, R. and *Berzins, M.,* 2001: The simulation of photochemical smog episodes in Hungary and Central Europe using adaptive gridding models. *Lect Notes Comput Sc 2074,* Part II, 67-70.

Lagzi, I., Kármán, D., Tomlin, A.S., Turányi, T. and *Haszpra, L.,* 2004: Simulation of the dispersion of nuclear contamination using an adaptive Eulerian grid model. *J Environ Radioactiv 75,* 59-82.

Lagzi, I., Mészáros, R., Ács, F., Tomlin, A.S., Haszpra, L. and *Turányi, T.,* 2006: Description and

evaluation of a coupled Eulerian transport-exchange model: Part I: model development. *Időjárás 110,* 349-363.

Lagzi, I., Tomlin, A.S., Turányi, T. and *Haszpra, L.,* 2009: Modelling photochemical air pollutant formation in Hungary using an adaptive grid technique. *Int J Environ Pollut 36,* 44-58.

Langnera, J., Robertsona, L., Perssona, C. and *Ullerstiga, A.,* 1998: Validation of the operational emergency response model at the Swedish Meteorological and Hydrological Institute using data from etex and the chernobyl accident. *Atmos Environ 32,* 4325-4333.

Larson, D.J. and *Nasstrom, J.S.,* 2002: Shared- and distributed-memory parallelization of a Lagrangian atmospheric dispersion model. *Atmos Environ 36,* 1559-1564.

Lovas, R., Patvarczki, J., Kacsuk, P., Lagzi, I., Turányi, T., Kullmann, L., Haszpra, L., Mészáros, R., Horányi, A., Bencsura, A. and *Lendvay, Gy.,* 2006: Air pollution forecast on the HUNGRID infrastructure. In *Parallel Comput: Current & Future Issues of High-End Computing,* (eds.: *G.R. Joubert, W.E. Nagel, F.J. Peters, O.G. Plata, P. Tirado, E.L. Zapata*). *John von Neumann Institute for Computing Series, Vol. 33, Jülich, Germany,* 121-128, ISBN 3-00-017352-8.

Martin, M., Oberson, O., Chopard, B., Mueller, F. and *Clappier, A.,* 1999: Atmospheric pollution transport: the parallelization of a transport & chemistry code. *Atmos Environ 33,* 1853-1860.

Martín, M.J., Parada, M. and *Doallo, R.,* 2004: High performance air pollution simulation using OpenMP. *J. Supercomput 28,* 311-321.

Mészáros, R., Lagzi, I., Juhász, Á., Szinyei, D., Vincze, Cs., Horányi, A., Kullmann, L. and *Tomlin, A.S.,* 2006: Description and evaluation of a coupled Eulerian transport-exchange model: Part II: Sensitivity analysis and application. *Időjárás 110,* 365-377.

Mikkelsen, T., Thykier-Nielsen, S., Astrup, P., Santabarbara, J.M., Sørensen, J.H., Rasmussen, A., Robertson, L., Ullerstig, A., Deme, S., Martens, R., Bartzis, J.G. and *Pasler-Sauer, J.,* 1997: MET-RODOS: A comprehensive atmospheric dispersion module. *Radiat Prot Dosim 73,* 45-56.

Molnár, F. Jr., Szakály, T., Mészáros, R. and *Lagzi, I.,* 2010: Air pollution modelling using a Graphics Processing Unit with CUDA. *Comput Phys Commun 181,* 105-112.

Ostromsky, T., Dimov, I.T. and *Zlatev, Z.,* 2005: Parallel implementation and one year experiments with the Danish Eulerian Model. *Lect Notes Comput Sc 3401,* 440-447.

Paulson, C.A., 1970: The mathematical representation of wind speed and temperature profiles in the unstable atmospheric surface layer. *J Appl Meteorol 9,* 857-861.

Pechinger, U., Langer, M., Baumann, K. and *Petz, E.,* 2001: The austrian emergency response modelling system TAMOS. *Phys. Chem. Earth (B) 26,* 99-103.

Pudykiewicz, J., 1989: Simulation of the Chernobyl dispersion with a 3-D hemispheric tracer model. *Tellus 41B,* 391-412.

Pudykiewicz, J., 1991: Environmental prediction systems: Design, implementation aspects and operational experience with application to accidental releases. In *Air Pollution Modeling and Its Applications VIII. NATO challenges of modern society* (eds.: *H. van Dop* and *D.G Steyn*). *Vol. 15.* Plenum Press, New York and London, pp. 561-590.

Ryall, D.B. and *Maryon, R.H.,* 1998: Validation of the UK Met. Office's name model against the ETEX dataset. *Atmos. Environ. 32,* 4265-4276.

Saltbones, J., Foss, A. and *Bartnicki, J.,* 1998: Norwegian Meteorological Institute's real-time dispersion model SNAP (severe nuclear accident program): Runs for ETEX and ATMES II experiments with different meteorological input. *Atmos. Environ. 32,* 4277-4283.

Singh, D.E., Garcia, F. and *Carretero, J.,* 2006: Parallel I/O optimization for an air pollution model. *Parallel Comput: Current & Future Issues of High-End Computing. Proceedings of the International Conference ParCo 2005* (eds.: *G.R. Joubert, W.E. Nagel, F.J. Peters, O. Plata, P. Tirado, E. Zapata*), *33,* 523-530.

Sørensen, J.H., Rasmussen, A., Ellermann, T. and *Lyck, E.,* 1998. Mesoscale influense on long-range transport – evidence from ETEX modelling and observations. *Atmos Environ 32,* 4207-4217.

Sørensen, J.H., Baklanov, A. and *Hoe, S.,* 2007. The Danish emergency response model of the atmosphere (DERMA). *J Environ Radioactiv 96,* 122-129.

Srinivas, C.V., Venkatesan, R., Muralidharan, N.V., Das, S., Dass, H. and *Kumar, P.E.,* 2006: Operational mesoscale atmospheric dispersion prediction using a parallel computing cluster. *J Earth System Science 115,* 315-332.

Stohl, A. and *Wotawa, G.*, 1997: Validation of the Lagrangian particle model FLEXPART using ETEX data. ETEX syposium on long-range atmospheric transport, model verification and emergency response. *European Commission* EUR 17346,167-170.

Stohl, A., Hittenberger, M. and *Wotawa, G.*, 1998: Validation of the lagrangian particle dispersion model FLEXPART against large-scale tracer experiment data. *Atmos Environ 32*, 4245-4264.

Stohl, A., Forster, C., Frank, A., Seibert, P. and *Wotawa, G.*, 2005: Technical note: The Lagrangian particle dispersion model FLEXPART version 6.2. *Atmos Chem and Phys 5,* 2461-2474.

Zegeling, P.A. and *Kok, H.P.*, 2004: Adaptive moving mesh computations for reaction-diffusion systems. *J. Comput Appl Math 168,* 519-528.

IDŐJÁRÁS

Quarterly Journal of the Hungarian Meteorological Service
Vol. 114, No. 1–2, January–June 2010, pp. 121–133

The quasi-operational LAMEPS system of the Hungarian Meteorological Service

Edit Hágel

Hungarian Meteorological Service
P.O. Box 38, H-1525 Budapest, Hungary; E-mail: hagel.e@met.hu

(Manuscript received in final form February 11, 2010)

Abstract — Dynamical downscaling of the global ARPEGE based ensemble prediction system PEARP is running quasi-operationally at the Hungarian Meteorological Service since February 2008. For the downscaling of the PEARP members, the ALADIN limited area model is used with 12 km horizontal resolution. Both systems have 10+1 ensemble members (one control member that starts from the unperturbed analysis and 10 members which start from perturbed initial conditions). At present, both the initial and lateral boundary conditions of the ALADIN runs are provided by the PEARP ensemble members, however, it is planned to generate the initial condition perturbations locally at a later stage. In the article this quasi-operational short-range limited area ensemble prediction system, as well as its performance through verification results will be presented.

Key-words: numerical weather prediction, limited area forecasting, predictability, ensemble method, verification

1. Introduction

In order to predict the future state of the atmosphere, the use of mathematical models is required. Forecasts are made by solving a set of partial differential equations, the so-called primitive equations. These equations are nonlinear and, therefore, impossible to solve analytically. Because of the nonlinear nature of the equations, the solution is highly dependent on the accuracy of the initial conditions. The problem is that the true state of the atmosphere cannot be known exactly. The reason of this is that the number of the observations is limited (smaller than the degrees of freedom in the models), their distribution is uneven around the globe, there are inevitable observational errors, and also errors in the data assimilation techniques. As a result, there will always be some uncertainty in the initial conditions of the numerical weather prediction (NWP) models.

(One should not forget that the initial condition error is only one source of the possible forecast errors, there are errors in the models themselves. However, in the system described in the present article we only dealt with the initial condition errors.) Possible solution of the above mentioned problem is to run a set, or as usually called, an ensemble of forecasts, each starting from a slightly different initial condition, thus, they are equally likely realizations of the "true" atmospheric state. The advantage of this method is clear: the spread of the ensemble members can provide useful information on the predictability of the atmospheric state, and a probability value can be assigned to different weather events. In other words, not only the future state of the atmosphere can be forecasted, but one can also predict the uncertainty related to this forecast.

Since its first operational application in 1992 (see *Buizza et al.*, 1993; *Toth* and *Kalnay*, 1997), ensemble forecasting has become a widely used technique by many meteorological services around the world. Despite its obvious benefits, it was used only on global scales and in the medium-range for a long time. In the last couple of years, intensive research has started to apply the ensemble method in short-range limited area forecasting as well (see, e.g., *Montani et al.*, 2003; *Jensen et al.*, 2006; *García-Moya et al.*, 2007). Motivated by the results of these experiments, research started at the Hungarian Meteorological Service (HMS) with the final aim to establish an operational LAMEPS[1] system for the Central European area, and to see how it can improve the predictions of the existing global forecasting systems. It was decided to start the experiments with the dynamical downscaling of global ensemble forecasts. Two possible choices were considered: downscaling of ARPEGE[2] ensemble forecasts (see *Hágel* and *Horányi*, 2006, 2007 for a detailed description of the experiments) and downscaling of ECMWF[3] EPS[4] members (for further information on ECMWF EPS downscaling see *Szintai* and *Ihász* (2006)).

Since February 2008, a LAMEPS system is running in quasi-operational status at the HMS. The system is based on the dynamical downscaling of the ARPEGE (global) ensemble system, PEARP[5]. The aim of this article is to present this quasi-operational short-range limited area ensemble prediction system. The characteristics of the system are described in Section 2. Verification results are presented in Section 3, and finally, conclusions and future plans are outlined in Section 4.

1 LAMEPS: Limited Area Model Ensemble Prediction System
2 ARPEGE: Action de Recherche Petite Echelle Grande Echelle (i.e., Research Project on Small and Large Scales)
3 ECMWF: European Centre for Medium-Range Weather Forecasts
4 EPS: Ensemble Prediction System
5 PEARP: Prévision d'Ensemble ARPege

2. *Characteristics of the system*

The 11-member short-range limited area ensemble prediction system of HMS has been running every day, in quasi-operational status, since February 2008. It is run with the ALADIN[6] limited area model and it is driven by the members of the global PEARP system. PEARP is the operational global ensemble prediction system of Météo-France. The initial perturbations of this global system are created as a combination of singular vectors (targeted over four different areas) and evolved perturbations of the previous PEARP run. PEARP has 10 + 1 members (10 perturbed and the unperturbed control member) and it is run once a day starting from the 18 UTC analysis.

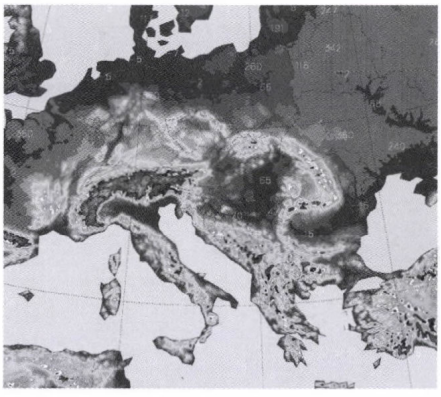

Fig. 1. The integration domain and the orography of the ALADIN LAMEPS system.

The members of the global PEARP system are downscaled at HMS with the limited area model ALADIN (for more information on the ALADIN model, see *Horányi et al.*, 2006). At present, no local data assimilation or generation of local perturbations are applied for the LAMEPS. Forecasts are made once a day starting from the 18 UTC data. In order to be able to use the outputs of the global model as initial and lateral boundary conditions, an interpolation is needed to the exact domain and resolution which is used for the model integration. Once the initial and lateral boundary conditions are in the proper format (resolution, domain, etc.), the integration of the model can start. The ALADIN ensemble system is running on a domain covering a large part of Continental Europe (*Fig. 1*) with a horizontal resolution of approximately 12 km. In the vertical 46 levels are used. Forecast length is 60 hours and the time step used for the integration is 450 seconds (7.5 minutes). Finally, post-processing is performed on the raw model outputs in order to support the application of the model results by forecasters or end-users. After performing post-processing to a

6 ALADIN: Aire Limitée Adaptation dynamique Développement International

latitude-longitude grid, the outputs of the LAMEPS system are mainly visualized using HAWK[7] which is used in the everyday work of forecasters to visualize the outputs of several NWP models (both deterministic and probabilistic), observations, radar and satellite data, etc. The available products from our LAMEPS system are the ensemble mean, the ensemble spread (computed around the mean), individual ensemble members, and probability fields for several parameters. The individual members can be visualized in the form of spaghetti diagrams. In addition, plume diagrams are also plotted for several parameters and selected Hungarian locations.

3. Verification results

Verification of the quasi-operational LAMEPS system was performed for almost nine months from March 10, 2008 to November 30, 2008 against the ECMWF analysis. Scores were computed for the whole period and also for the different seasons separately (only the results for the whole period are shown, not the separate seasons). The verified parameters were temperature, geopotential, and wind speed on several levels (500 hPa, 700 hPa, 850 hPa, 925 hPa, and 1000 hPa). The common LACE[8] verification package was used. This verification package was developed in collaboration with colleagues from other LACE countries (see *Hágel*, 2006; *Mladek*, 2006; *Kann*, 2007). For a detailed description of the verification methods, the reader is referred to *Jolliffe* and *Stephenson* (2003).

3.1. Comparing the error of the ensemble mean and the control member

As a first step, the error of the control member was compared with the error of the ensemble mean. Since the perturbations in the global PEARP system are symmetric around the unperturbed initial condition and have a small amplitude at initial time, the ensemble mean and the control forecast are almost identical in the early forecast ranges. As no local perturbations are added, the same behavior is assumed for the LAMEPS. The similarity of the ensemble mean and the control member means that their RMSE (root mean squared error) is also very similar. However, after the initial linear phase it is expected that the ensemble mean has lower RMSE values than the control forecast, since the averaging has the effect of filtering out the less predictable features and leaving only the more predictable ones, those that show agreement among the members of the ensemble.

For geopotential the RMSE of the control member and the RMSE of the ensemble mean were almost identical during the whole period. (*Fig. 2a* shows the results for 500 hPa.) For temperature (*Fig. 2b* shows the results for 500 hPa) and wind speed (see *Fig. 2c* for the scores on 1000 hPa) there was a difference

7 HAWK: Hungarian Advanced WorKstation (http://www.met.hu/nmo/hawk_en)
8 LACE: Limited Area modeling in Central Europe (www.rclace.eu)

between the ensemble mean and the control forecast already after the first 6 hours, with the ensemble mean having lower RMSE values. Results indicate that in the case of geopotential, the ensemble members remain centered around the control member during almost the whole forecast period, hence the RMSE of the ensemble mean and the control member are almost identical. For wind speed and temperature the ensemble mean and the control forecast start to differ from the early forecast ranges, which suggests that nonlinearity has a stronger effect on these parameters.

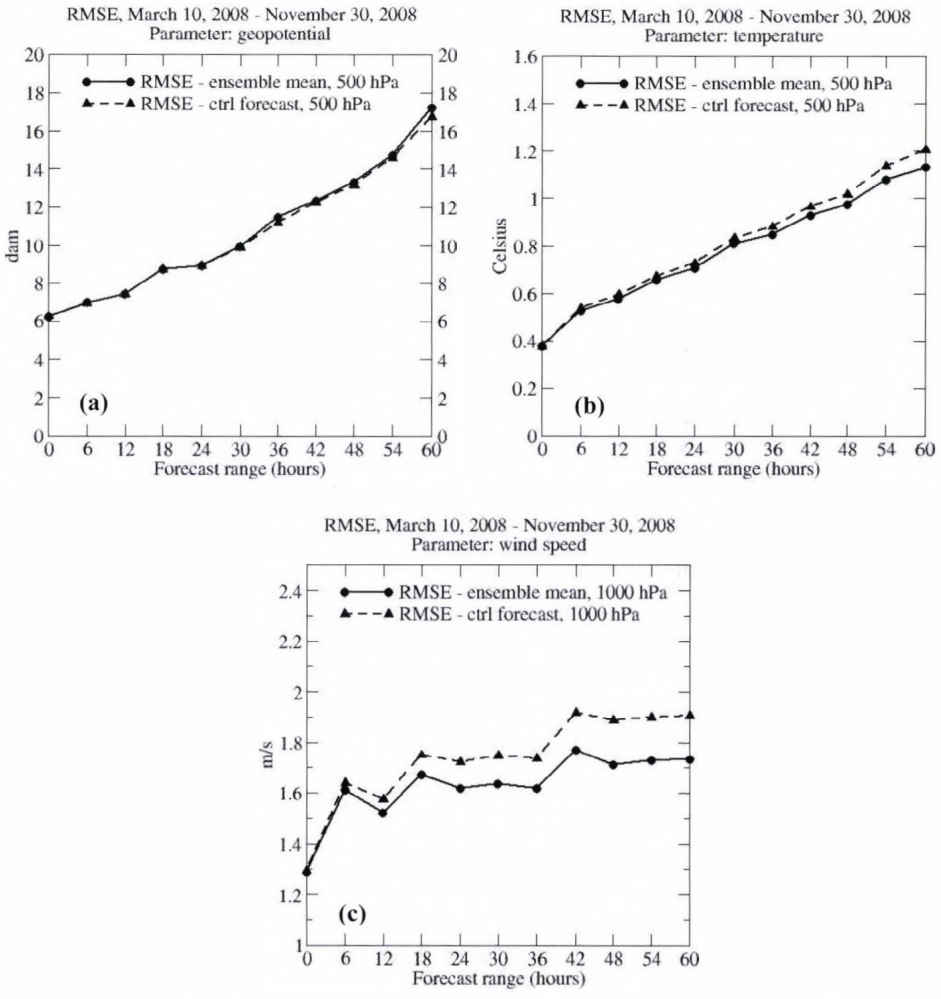

Fig. 2. RMSE of the ensemble mean and RMSE of the control member for (a) geopotential at 500 hPa, (b) temperature at 500 hPa, and (c) wind speed at 1000 hPa. The verification interval is March 10, 2008–November 30, 2008. Verification was performed against ECMWF analysis.

3.2. Spread-skill relationship, percentage of outliers

Another important feature of an ensemble system is the spread-skill relationship. The spread of the ensemble system (computed around the ensemble mean) should be in a good agreement with the forecast error (e.g., RMSE of the ensemble mean). In the case of large error, large spread is expected as a sign of high unpredictability. On the other hand, if the spread is small, it is expected that the situation has good predictability, therefore, the error should be small as well. If the spread is larger (smaller) than the error, then the system is said to be over- (under-) dispersive.

In *Fig. 3*, the spread-skill relationship is plotted for geopotential, temperature, and wind speed for two levels: 500 and 850 hPa. In all cases the system was found to be underdispersive, i.e., the spread was smaller than the RMSE of the ensemble mean.

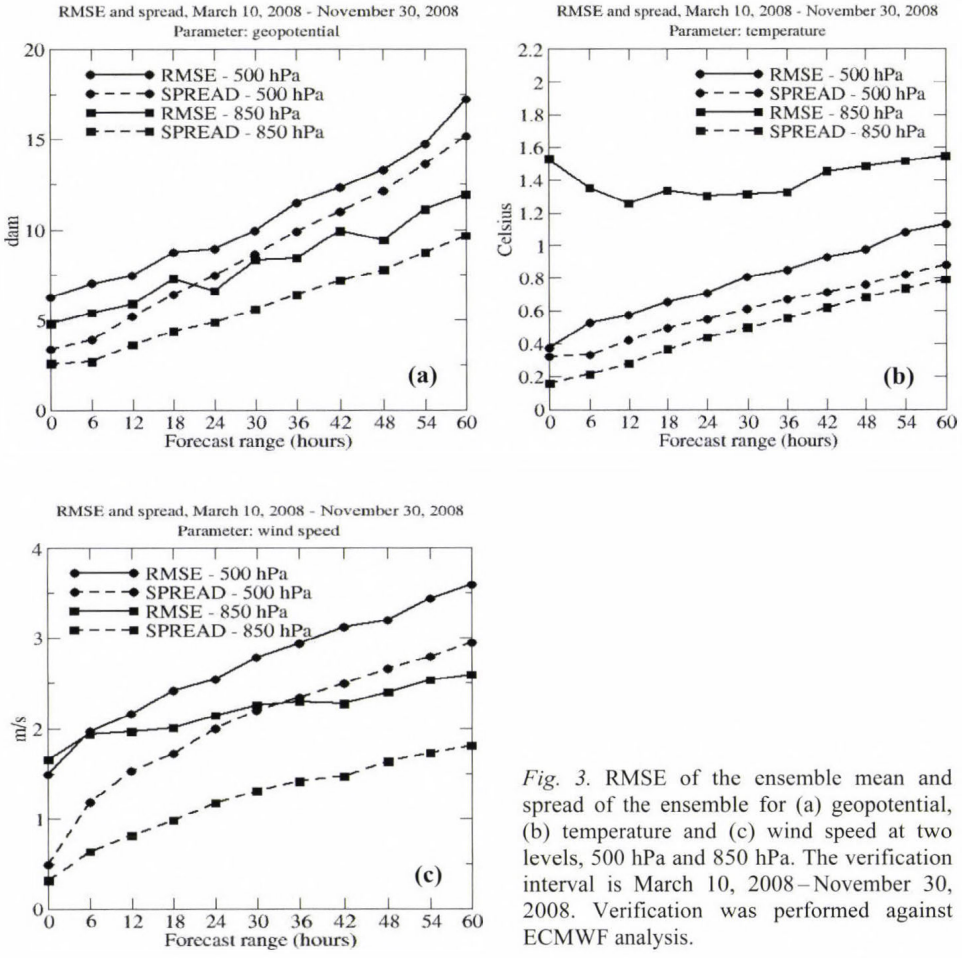

Fig. 3. RMSE of the ensemble mean and spread of the ensemble for (a) geopotential, (b) temperature and (c) wind speed at two levels, 500 hPa and 850 hPa. The verification interval is March 10, 2008–November 30, 2008. Verification was performed against ECMWF analysis.

Another way of analyzing the spread of an ensemble system is the use of percentage of outliers diagrams. These diagrams tell us how often the verifying analysis lies out of the interval defined by the (sorted) ensemble members. *Fig. 4* shows the percentage of outliers for geopotential, temperature, and wind speed at 500, 700, 850, 925, and 1000 hPa.

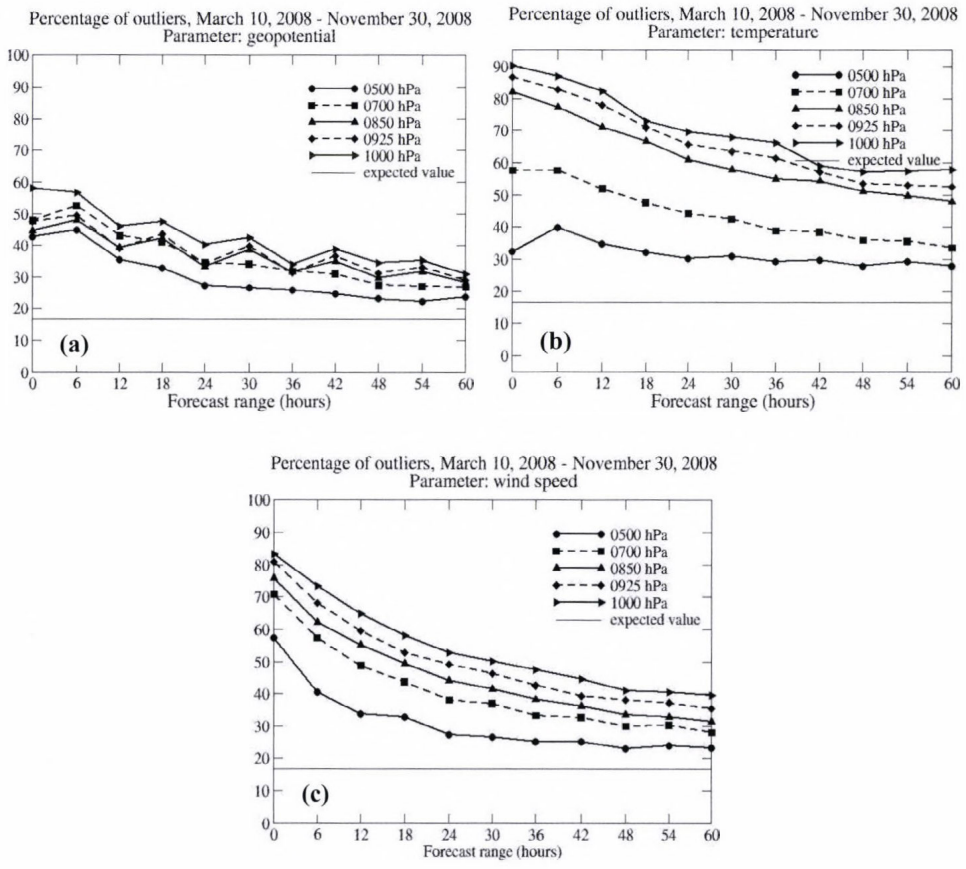

Fig. 4. Percentage of outliers diagrams for (a) geopotential (b) temperature, and (c) wind speed at 500 hPa, 700 hPa, 850 hPa, 925 hPa, and 1000 hPa. Values are in %. The verification interval is March 10, 2008 – November 30, 2008. Verification was performed against ECMWF analysis. The thin horizontal line is the expected value, i.e., $2 \cdot 100/(\text{ensemble members} + 1)$.

For all levels and parameters, the percentage of outliers was above the expected value. This means that the verifying analysis too often falls out of the interval defined be the (sorted) ensemble members, indicating that the spread of the ensemble is not sufficient. Both in case of the spread-skill relationship and the

percentage of outliers diagrams, best results were obtained for 500 hPa and got worse as going closer to the surface. This behavior might have several reasons, related to the perturbations used in the PEARP system:

- No perturbation of surface parameters, except for surface pressure.
- The maximum of the energy of the (global) singular vectors is located around 700 hPa and during their evolution the energy propagates upwards, rather than downwards.
- The uncertainties related to the physical parameterizations are not addressed at all during the singular vector computation.

This behavior (better results for higher levels) suggests that surface perturbations should also be included in the system. One can also conclude that even for 500 hPa, the spread of the ensemble is smaller than the RMSE of the ensemble mean, and the percentage of outliers is above the expected value. This indicates that local perturbations, targeted especially to the area of our interest would be needed to improve the quality of the system.

3.3. ROC and reliability diagrams

ROC[9] and ROC area diagrams represent the skill of the ensemble system compared to the use of climatological statistics. A ROC area of 1 represents a perfect system, while an area less than 0.5 means the forecasts have no skill compared to climatological data. Reliability diagrams are used to test the ability of the system to correctly forecast probabilities of a certain event. For that reason, forecast probabilities are plotted against conditional observed frequencies (with forecast probabilities on the x-axis and observed frequencies on the y-axis). For a perfect system the points lie along the diagonal.

ROC and reliability diagrams were plotted for wind speed only (for technical reasons), with thresholds 1, 2, 5, and 10 m/s on five levels (500, 700, 850, 925, and 1000 hPa). Comparison was made between (i) different thresholds, (ii) different forecast ranges, and (iii) different vertical levels. The comparison between the different thresholds reveals that results are better for higher wind speeds. For reliability diagrams, in the case of 1 m/s threshold, the system shows significant underestimation for low and middle probabilities and slight overestimation for high probabilities. For higher thresholds, the underestimation for low probabilities and overestimation for high probabilities remains, but the curves move significantly closer to the diagonal. (Fig. 6a shows examples for 1000 hPa and T+60 hours.) Similar results were obtained by analyzing the ROC diagrams (*Fig. 5a*): the ROC area was well above 0.5 for all thresholds, with more skillful forecasts for wind speeds larger than, e.g., 10 m/s than wind speeds exceeding 1 m/s.

9 ROC: Relative Operating Characteristics

The comparison between different forecast ranges shows that the system has similar skill throughout the whole forecast interval, however, results are somewhat worse in the early forecast ranges according to the reliability diagrams (this was more pronounced in autumn than during spring and summer). *Fig. 5b* and *Fig. 6b* show examples for 1000 hPa and 10 m/s as threshold.

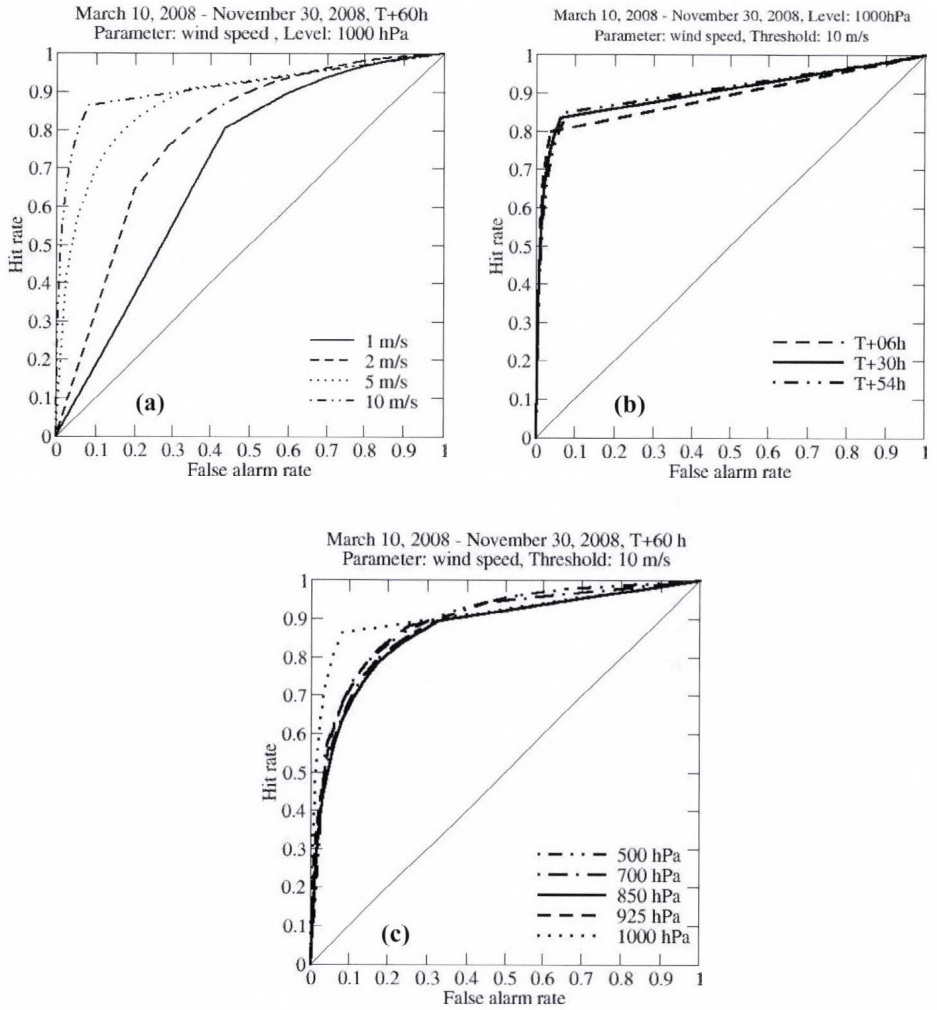

Fig. 5. ROC diagrams for wind speed. (a) Diagrams for thresholds 1 m/s, 2 m/s, 5 m/s, and 10 m/s at 1000 hPa and T+60 hours. (b) Diagrams for time range T+06 hours, T+30 hours, and T+54 hours at 1000 hPa and 10 m/s threshold. (c) Diagrams for 500 hPa, 700 hPa, 850 hPa, 925 hPa, and 1000 hPa at T+60 hours and 10 m/s threshold. The verification interval is March 10, 2008–November 30, 2008. Verification was performed against ECMWF analysis.

As regards the different vertical levels, ROC and reliability curves were plotted for different vertical levels as well. In terms of ROC, results are quite similar for all levels, the only exception is 1000 hPa where the shape of the curves was slightly different, but the ROC area was similar to the other levels. *Fig. 5c* shows examples for T+60 hours and 10 m/s as threshold. Reliability diagrams show that for low probabilities results are quite similar for all levels and show a very good reliability in case of higher thresholds. For high probabilities, differences are more significant and the curves lie somewhat farther from the diagonal with better results for higher levels. This is in agreement with the conclusions drawn from other verification measures. *Fig. 6c* shows examples for T+60 hours and a 10 m/s threshold.

3.4. Comparing the performance of the global and the limited area systems

When running limited area forecasts, it is always important to know whether the limited area model can improve the predictions of the global model or not. Verification results of the global and the limited area ensemble systems were compared to each other during the pre-operational experiments (*Hágel* and *Horányi*, 2006, 2007) for the period from January 15, 2005 to February 15, 2005. It can be said that by simply downscaling the global PEARP forecasts using the higher resolution ALADIN model, it is very difficult to achieve significant – overall – improvements. For some parameters and verification measures the limited area ensemble forecasts performed better, in other cases the global forecasts were more skillful. Also, in a couple of cases, the two models had nearly the same scores. Some aspects behind these results might be the relatively small resolution difference between the global and the limited area models (approximately 23 km and 12 km, respectively), or the too strong impact of the lateral boundary conditions.

As limited area models are running with a better horizontal resolution than their global counterparts, the representation of the orography is more realistic, which is very important in the case of, e.g., wind or precipitation forecasts. As a result of the increased resolution, limited area models can produce more reliable mesoscale structures. Therefore, it is important to run limited area models even if there is no significant – overall – improvement with respect to the global model providing the lateral boundary conditions.

In addition, one should not forget that it is a common phenomenon, that high resolution models might perform worse (on average, not for all individual cases) than the low resolution ones, when usual verification measures are applied. Although the increased resolution generally produces more realistic results, inevitable errors in timing and position can lead to larger RMSE values than for the smoother forecasts of the low resolution model. This is known as the *double penalty* problem. Therefore, the results presented above (i.e., no significant overall improvement by the limited area system) should be interpreted with care.

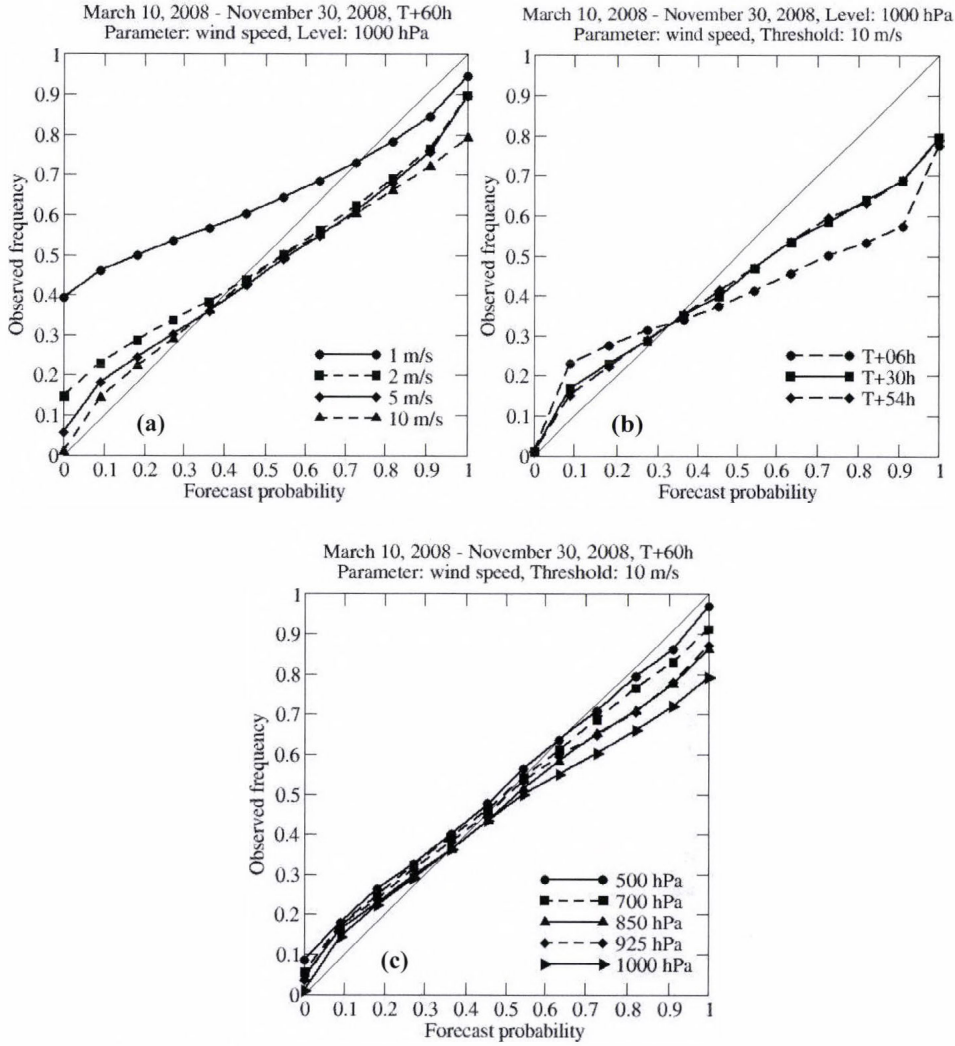

Fig. 6. Reliability diagrams for wind speed. (a) Diagrams for thresholds 1 m/s, 2 m/s, 5 m/s, and 10 m/s at 1000 hPa and T + 60 hours. (b) Diagrams for time range T + 06 hours, T + 30 hours, and T + 54 hours at 1000 hPa and 10 m/s threshold. (c) Diagrams for 500 hPa, 700 hPa, 850 hPa, 925 hPa, and 1000 hPa at T + 60 hours and 10 m/s threshold. The verification interval is March 10, 2008 – November 30, 2008. Verification was performed against ECMWF analysis.

4. Conclusions

In February 2008, a short-range limited area ensemble prediction system – based on the ALADIN model – was put into operations at HMS in order to gain experience not only from case studies and test periods, but on a day-to-day, real-

time basis. At present, the only operationally feasible solution is the direct downscaling of the PEARP members, therefore, this method is applied. Verification results of almost nine months (from March 10, 2008 to November 30, 2008) were analyzed using several verification measures for different parameters. As an overall conclusion it can be said, that the system behaved very similar in all three seasons (only the overall scores were shown). In spite of the problems with the spread-skill relationship (especially observed at lower levels and the surface), there are cases when the ensemble members show large spread, indicating the high uncertainty of the situation. In such cases the LAMEPS is definitely a useful complement of the operational deterministic ALADIN run. Results have shown that better scores are obtained for higher levels. The possible reasons of this behavior were described in Section 3. However, it is important to have skillful prediction of surface parameters as well. It would also be desirable to compute perturbations that are targeted for the area of our interest (Central Europe, particularly Hungary), in order to improve the spread-skill relationship and the quality of the forecasts as well. For these reasons it was decided to focus on the evaluation of local perturbations. Experiments have started to compute singular vectors with the ALADIN model (see *Hágel*, 2008). The aim of these experiments is to generate perturbations from the ALADIN singular vectors, and use them to perturb locally the initial conditions of the LAMEPS system. Perturbation of surface fields is also an important issue to be solved. A possible solution could be the method applied in the LAEF[10] system. Thus, the quasi-operational LAMEPS system of HMS is going to be developed and improved continuously, using the results of the ongoing researches.

Acknowledgments—The author wishes to thank to the team of Météo-France for making possible the operational use of the PEARP members as initial and lateral boundary conditions. The support and help of the members of the NWP group of the Hungarian Meteorological Service is also very much appreciated.

References

Buizza, R., Tribbia, J., Molteni, F. and *Palmer, T.*, 1993: Computation of optimal unstable structures for a numerical weather prediction model. *Tellus 45A*, 388-407.

García-Moya, J.A., Callado, A., Santos, C., Santos-Munoz, D. and *Simarro, J.*, 2007: El sistema de predicción por conjuntos para el corto plazo del INM. *AME Boletín 16*, 22-27.

Hágel, E., 2006: Report on work in Vienna on the common verification package (available at www.rclace.eu).

Hágel, E. and *Horányi, A.*, 2006: The development of a limited area ensemble prediction system at the Hungarian Meteorological Service: Sensitivity experiments using global singular vectors, preliminary results. *Időjárás 110*, 229-252.

Hágel, E. and *Horányi, A.*, 2007: The ARPEGE/ALADIN limited area ensemble prediction system: The impact of global targeted singular vectors. *Meteorol Z 16*, 653-663.

10 LAEF: Limited Area Ensemble Forecasting

Hágel, E., 2008: Singular vector experiments at the Hungarian Meteorological Service. *ALADIN Newsletter 33*, 52-59.

Horányi, A., Kertész, S., Kullmann, L., and *Radnóti, G.*, 2006: The ARPEGE/ALADIN mesoscale numerical modeling system and its application at the Hungarian Meteorological Service. *Időjárás 110*, 203-227.

Jensen, M.H., Frogner, I-L., Iversen, T. and *Vignes, O.*, 2006: Limited area ensemble forecasting in Norway using targeted EPS. *ECMWF Newsletter 107*, 23-29.

Jolliffe, I.T. and *Stephenson, D.B.* (eds.), 2003: *Forecast Verification: A Practitioner's Guide in Atmospheric Science.* Wiley.

Kann, A., 2007: Work on the Common Verification Package for the evaluation of ensemble forecasts (available at www.rclace.eu).

Mladek, R., 2006: Work on the Common Verification Package for the evaluation of ensemble forecasts (available at www.rclace.eu).

Montani, A., Capaldo, M., Cesari, D., Marsigli, C., Modigliani, U., Nerozzi, F., Paccagnella, T., Patruno, P. and *Tibaldi, S.*, 2003: Operational limited-area ensemble forecasts based on the 'Lokal Modell'. *ECMWF Newsletter 98*, 2-7.

Szintai, B. and *Ihász, I.*, 2006: The dynamical downscaling of ECMWF EPS products with the ALADIN mesoscale limited area model: Preliminary evaluation. *Időjárás 110*, 253-277.

Toth, Z., Kalnay, E., 1997: Ensemble Forecasting at NCEP and the Breeding Method. *Mon Weather Rev 125*, 3297-3319.

IDŐJÁRÁS

Quarterly Journal of the Hungarian Meteorological Service
Vol. 114, No. 1–2, January–June 2010, pp. 135–148

Fine scale simulation of turbulent flows in urban canopy layers

Miklós Balogh* and **Gergely Kristóf**

Department of Fluid Mechanics, Budapest University of Technology and Economics
Bertalan Lajos u. 4-6, H-1111 Budapest, Hungary
E-mails: baloghm@ara.bme.hu; kristof@ara.bme.hu

**Corresponding author*

(Manuscript received in final form October 22, 2009)

Abstract—The analysis of turbulent flows in urban areas is part of our research for simulating meso- and microscale atmospheric flows, since it is of great significance with respect to civil design and environmental protection. The application of general purpose computational fluid dynamics (CFD) solvers for the examination of smaller scale atmospheric phenomena, such as urban flows, has many advantages due to their flexible use on arbitrary meshes with complex geometries. A CFD solver has been adapted to atmospheric applications by using a purpose developed transformation method along with some volume sources active in the transport equations. In this way, the effects of the thermal stratification, adiabatic temperature variation, compressibility, and the Coriolis force were taken into account. Our present work is aimed at the development of a simulation methodology and software components for solving urban ventilation problems with special respect to the modeling of urban canopy layers. An advantage of the CFD based modeling technique is that the mesh size could change continuously in the computational domain according to the location of the building arrays, the road-system, and the examination area. This paper presents the modeling concept and its functionality in practice.

Key-words: CFD, urban canopy, turbulent flows, distributed drag force approach, two-equation model

1. Introduction

The detailed description of turbulence in the atmospheric boundary layer (ABL) is essential with regard to the dispersion and heat transfer processes, both within and above urban canopies. The realization of the accurate description is very difficult due to the complex structure of an urban canopy layer, which is a varied

system of bluff obstacles including trees and buildings. The examination of the urban climate, including the ventilation of the city, is possible by using statistical methods, such as roughness parameter mapping (*Gál* and *Unger*, 2009) or using dynamical methods. Though the detailed numerical simulation of flows in an urban canopy layer is possible by using CFD techniques, the higher numerical cost of the spatial discretization of the complex geometries makes this unrealizable in practice for very large domains. Finding the balance between the numerical cost and reasonable results is very important with regard to the civic design and environmental protection.

A potential technique, which keeps the balance, and furthermore, conforms to the variation of surface coverage, could be a hybrid method, such as a combination of the explicit and implicit description of the flow properties in an urban canopy. For simulating turbulent flows in the mostly exposed areas (e.g., some parts of the downtown area) where we need the most detailed results, the explicit modeling of the buildings could be used, and in the other parts of the examination area, the distributed drag force approach (*Green*, 1992; *Liu et al.*, 1996), as an implicit technique, could be applied with much lower numerical costs, although resulting in a lower resolution.

The efficient modeling of the flows in the atmospheric boundary layer, including turbulence, is feasible by solving the unsteady or steady state Reynolds-Averaged Navier-Stokes (URANS and RANS) equation due to the relatively low computational cost and reasonable accuracy. One of the most common turbulence model used in microscale investigations is the $k-\varepsilon$ two-equation model both for unsteady (URANS) and steady (RANS) simulations (*Hargreaves* and *Wright*, 2007). The main goal of this study is to develop an efficient hybrid method for simulating turbulent urban flows with CFD techniques.

2. *Application of a general purpose CFD solver for atmospheric simulations*

The use of a general purpose CFD solver adapted to atmospheric applications (*Kristóf et al.*, 2009) based on the realizable $k-\varepsilon$ model (*Shih et al.*, 1995) could be efficient for simulating urban ventilation and heat island problems in practice. The most common solvers are not capable of handling all of the physical processes in the arbitrarily stratified atmosphere, hence a mathematical transformation has been developed (*Kristóf et al.*, 2009). These are implemented in the ANSYS-FLUENT simulation system as a user defined function package, and validated with well documented laboratory experiments, analytical solutions, and widely accepted numerical results. This function package has been extended with functions for taking into account other important physical effects in connection with geophysical use, such as Coriolis force effects validated by analytical solutions. The results of the simulations of non-

hydrostatic phenomena, such as a descending cold air bubble, laboratory scale gravity waves, as well as urban heat island circulation agree well with references. The implemented physical processes, along with the distributed drag force approach, allow for the simulation of non-hydrostatic atmospheric flows in an urban environment. The present study focuses on modeling the impact of the obstacle arrays in the urban canopy layer, although, the examination of heat island phenomena is also in progress.

3. Distributed drag force approach

Recently, the application of CFD techniques is increasing in the field of micrometeorology, thus the knowledge of the flow structure and turbulence in an urban canopy layer is rapidly developing as well. Many scientists are working on the development of a distributed drag force approach, both for vegetated canopies (e.g., *Green*, 1992; *Liu et al.*, 1996) and for building arrays (*Lien* and *Yee*, 2004, 2005; *Lien et al.*, 2004, 2005; *Carissimo* and *MacDonald*, 2002). Therefore, it already has a solid theoretical background. This approach has already been used in practice for the urbanization of weather prediction models (*Hamdi* and *Masson*, 2008) to implicitly take into account the effect of buildings.

The essence of the drag force approach is an additional drag term in the momentum equation and two other terms in the transport equation of the turbulent kinetic energy (k) and the turbulent dissipation rate (ε). The drag term of the momentum equation is composed of the viscous and the form drags, while the value of the viscous component is much lower than the form component. Therefore, the former could be neglected. With this simplification, the source term of the momentum equation has a general form of

$$S_i = -\rho C_d A_i U u_i , \tag{1}$$

where ρ is the air density, C_d is the drag coefficient, A_i is the frontal area per unit volume normal to the ith direction, U is the velocity magnitude, and u_i is the velocity component in the ith direction. The unit of the momentum source is $\mathrm{N\,m^{-3}\,s^{-1}}$.

In the case of vegetated canopies, the obstacles (e.g., branches and leafs) convert the kinetic energy of the flow into wake turbulences with a smaller length scale than the shear-generated turbulence. Therefore, the canopy yields a net turbulent kinetic energy loss (*Green et al.*, 1995) instead of enhancing the wake production. This could be modeled with a source term in the following form,

$$S_k = \rho C_d A_f \left[\beta_p U^3 - \beta_d U k\right], \tag{2}$$

where A_f is the total frontal area per unit volume, k is the turbulent kinetic energy, β_p constant is a fraction of the mean flow kinetic energy produce k, and β_d is an empirical constant for short-circuiting the turbulent cascade (*Green*, 1992). The unit of the turbulent kinetic energy source is $\mathrm{kg\,m^{-3}\,s^{-1}}$.

The simplest model of the turbulent dissipation rate source term is based on the Kolgomorov's relation, which yields

$$S_\varepsilon = C_{\varepsilon 4} \frac{\varepsilon}{k} S_k \,. \tag{3}$$

The units for the turbulent dissipation rate source are $\mathrm{kg\,m^{-4}\,s^{-1}}$. In Eq. (3), ε is the turbulent dissipation rate and $C_{\varepsilon 4}$ is a constant. This relation was improved by *Liu et al.* (1996) providing a better fit to wind tunnel data. Accordingly, an alternative model could be defined as a more general form, which reads

$$S_\varepsilon = \rho C_d A_f \left[C_{\varepsilon 4} \beta_p \frac{\varepsilon}{k} U^3 - C_{\varepsilon 5} \beta_d U \varepsilon \right]. \tag{4}$$

In Eq. (4), the new constant $C_{\varepsilon 5}$ defines the mixing length anisotropy, if it is not equal to $C_{\varepsilon 4}$. Otherwise, the alternative model of Eq. (4) turns into the simpler Eq. (3) as noticed by *Sanz* (2003). It should be mentioned, that the source term of the turbulent dissipation rate is required in those microscale simulations that are based on two-equation turbulence models. In mesoscale models these terms can be neglected (*Otte et al.*, 2004). The coefficients in Eqs. (2)–(4) depend on the type of the turbulence model applied and the characteristics of the canopy layer. The relations between these constants and the constants of the k–ε model, together with the characteristics of the vegetated canopy were suggested by *Sanz* (2003) and were analyzed by *Katul et al.* (2004) and *Sanz* and *Katul* (2007).

In the present studies, the source terms of the momentum, turbulent kinetic energy, and turbulent dissipation rate were modeled in the above presented forms, applying the alternative model for describing S_ε. In vegetated areas, the properties of the drag terms were based on the works of *Balczó et al.* (2009), while in building arrays, the drag coefficient C_d was calculated as a function based on the volumetric porosity of the obstacle arrays (Appendix A) applied by *Coirier* and *Kim* (2006) in a similar application.

The goal of our method is to provide a mesh which follows the outlines of open areas, such as streets, squares, and open fields. The drag source terms should not be applied in these areas if the local mesh resolution is sufficiently high, thus explicit modeling is possible. Therefore, the impacts of these

cavities can be taken into consideration, although this strongly depends on mesh resolution.

4. An example on modeling turbulent flows in an urban canopy layer

In this section, we introduce a typical and practical application of CFD techniques in modeling turbulent atmospheric flows in urban areas. In this case study, the examination area is the 11th district of Budapest (the capital of Hungary), where a diversified landscape could be found, ranging from rural to downtown areas. Since this region is also surrounded by diversified regions, the examination area was extended with a relaxation zone for simplifying the setup of the lateral boundary conditions (Appendix B). In this way, the dimensions of the examination area in the x, y, and z directions were 9155, 7150, and 1800 m, respectively, while the computational domain extended by the relaxation zone (*Fig. 1*) is twice the original.

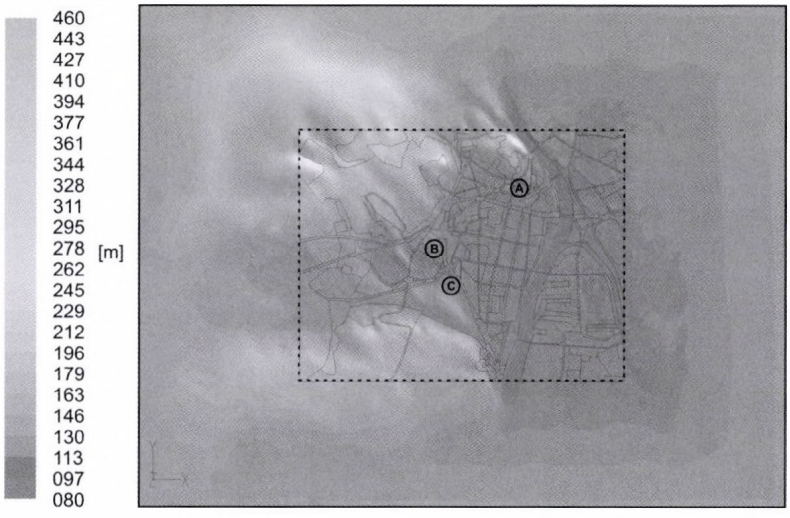

Fig. 1. Top view of the computational domain colored by the elevation. The similar surface coverage regions are highlighted (fine solid lines) in the examination area (thick dashed line), which is extended with the relaxation zone (thick solid line). The circles denote the sampling points of different canopy profiles used later.

The geometrical setup of the computational domain was based on the SRTM (Shuttle Radar Topography Mission) elevation database and a raster graphical map. It contains surface coverage and building cluster data in a simplified, type dependent form. The elevation data could be used after a coordinate transformation from WGS84 to a Cartesian frame of reference, namely the Uniform National Projection system (Hungarian abbreviation:

EOV). Nevertheless, the surface coverage data needed a pre-processing procedure for efficient use in modeling. As a result of these, the properties of the canopy layer such as the canopy layer height, the frontal area and solid fraction of the obstacles are available at each region of the computational domain. Since the domain contains several regions, we only introduce some typical parameters of urban type canopies (*Table 1*).

Table 1. Typical values of the total canopy height H, the solid fraction λ_f, and the frontal area per unit volume A_f in the urban type canopy, from different parts of the examination area

	Suburban (sample C)	**Block of flats (sample B)**	**Downtown (sample A)**
H [m]	7	20	15
λ_f [-]	0.3	0.4	0.6
A_f [$m^2 m^{-3}$]	0.55	0.63	0.77

Due to the finite volume method used in our simulation system, the spatial discretization of the domain, based on the computational mesh, is a system of wedge cells. This mesh was generated from the elevation data and the polygons are bounding the areas with the same type of surface coverage. The cells are triangular wedges with vertical orientation and their lateral edge length is varying between 8 and 160 meters in the examination area, growing up to 1000 meters in the relaxation zone, with a cell growth rate 1.3. For open fields, such as wider streets, parks, and the Danube River, the mesh size is the minimum possible. Therefore, the impact of these could be described at a higher resolution, as it can be seen in *Fig. 2*.

Vertically, the cells are ordered in layers and their height is increasing from 3 to 530 meters with the distance from the ground surface. The layers follow the terrain near the ground and become flat when approaching the upper boundary.

At the inlet boundaries the velocity components, turbulent kinetic energy, and dissipation rate were defined as pre-calculated profiles shown in *Fig. 3*. These were calculated by a one-dimensional, steady-state, realizable $k-\varepsilon$ model with the reference surface coverage conditions.

The wind climate in the district could be examined by averaging the results of the simulations executed for different boundary conditions. In the present example, eight runs were performed with different boundary conditions for the primary wind directions heaving the same velocity magnitude at 10 meters, which was 3 m s^{-1}. The simulations were steady state runs, while both the non-hydrostatic and Coriolis force effects were neglected. Therefore, only the source terms of the porous drag model and the non-reflective diffusion were enabled. The solver was used with second order upwind schemes for the spatial

discretization of the momentum equation, the turbulent kinetic energy and turbulent dissipation rate transport equations, and a second order scheme for the pressure equation. For better numerical stability, the SIMPLE pressure-velocity coupling was used, along with the node based Green-Gauss gradient scheme. With these settings, the simulations for the eight wind directions took only six hours using a Quad-Core computer.

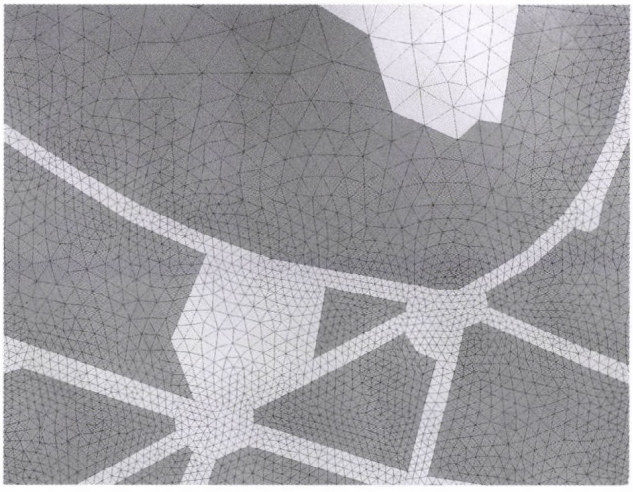

Fig. 2. The structure of the computational mesh of the downtown area of the 11th district, where the shaded areas show the building arrays, and the white ones denote uncovered areas such as streets, squares, and open fields, together with vegetated areas.

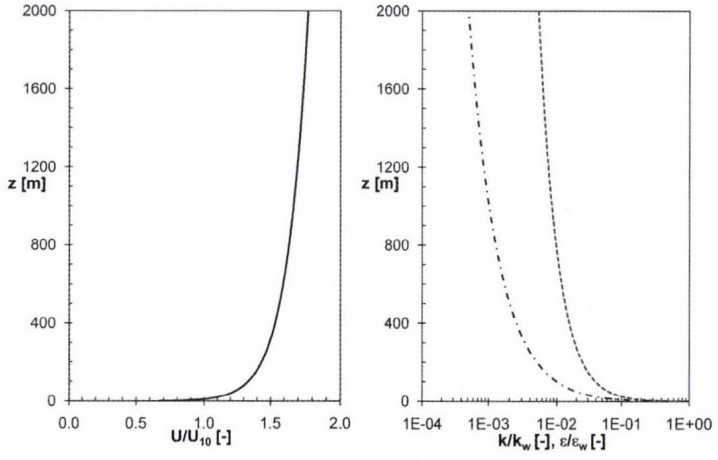

Fig. 3. Vertical profiles at the inlet boundaries, where the velocity magnitude (black) is scaled by the reference value at 10 meters above the ground. The turbulent kinetic energy (dashed) and dissipation rate (dashed-dotted) are normalized by the values next to the wall.

5. Results

Vertical profiles of the weighted average of the velocity magnitude and the turbulent shear stress, plotted along lines selected from different canopy regions from sampling points A, B, and C in *Fig. 1*, are verified using analytical canopy profiles. The analytical canopy profiles were published by *Finnigan* and *Belcher* (2004), calculating the velocity as

$$U(z)=\begin{cases}\dfrac{u_\tau}{\kappa}\ln\left(\dfrac{z-H+d}{z_0}\right), & \text{if } z>H \\ U_H e^{\beta(z-H)/l_m}, & \text{if } z\le H\end{cases}, \tag{5}$$

and the shear stress as

$$\tau(z)=l_m{}^2\left[\frac{dU}{dz}\right]^2, \tag{6}$$

where $U(z)$ and $\tau(z)$ are the velocity and the shear stress magnitudes, u_τ is the friction velocity, κ is the von Kármán constant, z is the height above the ground, H is the height of the canopy, U_H is the velocity magnitude at the top of the canopy, d is the displacement height, z_0 is the roughness height, l_m is the mixing length, and β is a constant of the profile. Note that u_τ, z_0, d, and l_m are functions of the canopy density. These fall within the range of the analytical results, for low and high canopy densities (*Fig. 4*), although some differences could be found in the shape of the profiles farther on the ground surface. The reason of these differences could be that the analytical profiles were calculated for flat surface, while our simulations were applied on complex terrain.

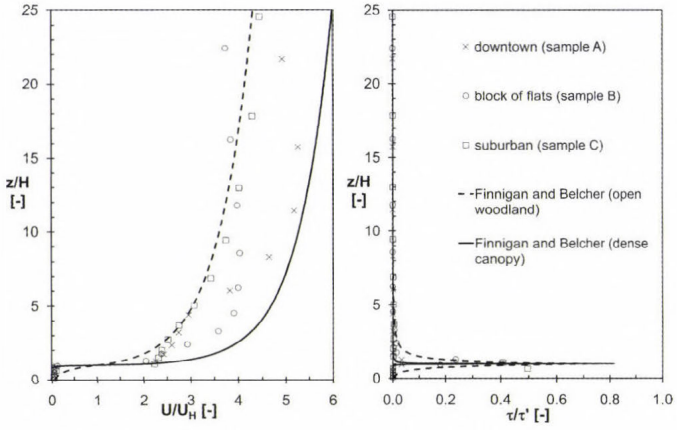

Fig. 4. Normalized velocity and shear stress profiles as a function of the height scale z/H, where U_H is the velocity at the top of the canopy and $\tau'=\rho u_\tau^2$. Sampling points A, B, and C can be seen in *Fig. 1*.

The averaged flow fields, which characterize the different regions of the district concerning the ventilation, are calculated from the results of the different cases weighted by the probability of the case dependent wind direction, both for the velocity magnitude and turbulent quantities. The average velocity magnitude as a quantitative parameter predicts the ventilation of the different regions, while the turbulent intensity contains useful information about the turbulent fluctuations. These were plotted at different heights above the ground, namely at 10 and 30 meters. The velocity and turbulent intensity fields are also scaled by the reference values of those calculated from the inlet profiles taking into consideration the local elevation. Since the inlet profiles are defined for an undisturbed free flow over a smooth surface, the scaled fields express the impact of the topography of the examination area and the topology of the canopy layer.

Fig. 5. Distribution of the velocity magnitudes scaled by reference values (inlet profiles) in the examination area, at 10 meters above the ground.

Near the surface, as shown in *Fig. 5*, over open areas, such as streets, squares, parks, and over the Danube River, the velocity magnitudes are significantly higher than the reference values due to the horizontal displacement of dense regions where the flow is moderated by obstacles. Moving away from the surface, the velocity is increasing as an effect of the canopy reducing blocking, although above the canopy layer height, the impact of the drag is still realizable (*Fig. 6*).

The scaled turbulence intensity has a local minimum near the surface (*Fig. 7*), since the reference turbulence intensity has the maximum next to the wall. The reference profiles were calculated with free flow conditions, thus, only

the wall has an impact on its turbulent properties. At 30 meters above the ground, shown in *Fig. 8*, the turbulence develops at the boundaries of the blocks, mainly where the canopy properties change suddenly. This effect is stronger on those side of the canopy blocks where the gradient of the porous drag has a high positive value in the streamwise direction of the locally dominant wind.

Fig. 6. Distribution of the velocity magnitudes scaled by reference values (inlet profiles) in the examination area, at 30 meters above the ground.

Fig. 7. Distribution of the turbulent intensity scaled by reference values (inlet profiles) in the examination area, at 10 meters above the ground.

Fig. 8. Distribution of the turbulent intensity scaled by reference values (inlet profiles) in the examination area, at 30 meters above the ground.

6. Conclusions and further developments

After the implementation of the distributed drag force parameterization, a practical application was executed, which demonstrates the capabilities of the CFD based approach in fields of the urban climatology and pollution control. The source term of the parameterization was applied within the areas where obstacles were found, thus, the impacts of the street canyons could also be considered. The properties of the canopy layer were also changed according to their type. The averaged results of the simulation were verified with analytical canopy profiles in representative points and good qualitative agreement has been found.

The results of the current study are useful for the further development in modeling stratified canopy layers, including the effects of the heat island phenomena and thermal convection. The realization of this requires the adaptation of the parameterization schemes modeling heat transfer and storage in the urban canopy layer (e.g., *Vu et al.*, 2002) with higher resolution.

Acknowledgements—This research was supported by the Hungarian Scientific Research Fund (Hungarian abbreviation: OTKA, grant No. T049573), and the wind climate examination supported by the Local Government of the 11th district of Budapest. The author would like to express special thanks for the data and information regarding the district, given free run by the Local Government.

Appendix A: Calculation of the drag coefficient

For the simplification of the drag coefficient C_d, it was calculated as a function of the volumetric porosity of the obstacle array applied by *Coirier* and *Kim* (2006) in a similar application. After adapting this function to our model, the drag coefficient could be defined in the following way

$$C_d = \begin{cases} \dfrac{\min(\Delta z, H - z_c + 0.5\Delta z)}{[1-\lambda_t]\Delta z}, & \text{if } z_c - 0.5\Delta z \le H \\ 0, & \text{if } z_c - 0.5\Delta z > H \end{cases}, \tag{A1}$$

where λ_t is the total solid volume per unit volume composed by the volume of the buildings and the vegetation, H is the canopy height, z_c is the height of the cell centroid above the ground, and Δz is the height of the cell.

Appendix B: Simplified specification of the boundary conditions

Both the elevation and surface coverage data were relaxed in the space to their reference values along the relaxation zone from the edge of the examination area to the lateral boundaries with the use of a dumping function Eq. (6). The reference value for the elevation was its spatial average at the lateral sides of the domain, while for the specification of the relaxed surface coverage parameters, the properties of the open grassland were used as a reference. For this reason, identical vertical profiles could be defined at every inlet boundary, calculated with the reference surface coverage properties.

$$\sigma(r) = \frac{1+\cos r}{2}, \quad r \in [0, \pi]. \tag{B1}$$

The dumping coefficient $\sigma(r)$ is a function of the normalized distance from the closest lateral boundary r. In the relaxation zone, the elevation and the characteristics of the canopy continuously approach a reference value defined on the boundary by Eq. (7).

$$\phi(r) = \sigma(r)\phi_{ref} + [1-\sigma(r)]\phi, \tag{B2}$$

where ϕ and ϕ_{ref} are the values of the relaxed parameter at the nearest part of the examination area and at the lateral boundary, respectively. The realization of the non-reflective boundary conditions could also be obtained by using

additional source terms (*Bodony*, 2006) in the relaxation zone as an analogy of Eq. (7), which is, written in a general form, is

$$S_r(r,\phi) = -\frac{\sigma(r)}{\Delta t}\left[\rho\phi - \rho_{ref}\phi_{ref}\right], \tag{B3}$$

where S_r is the non-reflective diffusion source term, Δt is the time-step size, ρ and ϕ are the current, ρ_{ref} and φ_{ref} are the reference values of the fluid density and the field variable of the transport equation, respectively. The field variable is the velocity in the source term of the momentum equation, the enthalpy in the energy equation, and φ equals 1 in the continuity equation. Note that in steady simulations, the value of the time-step size could be replaced by a time scale, while in incompressible cases ρ is equal to ρ_{ref}.

References

Balczó, M., Gromke, C., Ruck, B., 2009: Numerical modelling of flow and pollutant dispersion in street canyons with tree planning. *Meteorol Z 18*, 197-206.

Bodony, D.J., 2006: Analysis of sponge zones for computational fluid mechanics. *J Comput Phys 212*, 681–702.

Carissimo, B., Macdonald, R.W., 2002: A porosity/drag approach for the modeling of flow and dispersion in the urban canopy. In *Air Pollution Modeling and Its Application XV*. Springer, pp. 385-393.

Coirier, W.J., Kim, S., 2006: CFD modeling for urban area contaminant transport and dispersion: Model description and data requirements. *6th Symposium on the Urban Environment*. Atlanta, *GA. Amer Meteor Soc.*

Finnigan, J.J. and *Belcher, S.E.*, 2004: Flow over a hill covered plant canopy. *Q J Roy Meteor Soc130*, 1-29.

Gál, T., Unger, J., 2009: Detection of ventilation path using high-resolution roughness parameter mapping in a large urban area. *Build Environ 44*(1), 198-206

Green, S.R., 1992: Modelling turbulent air flow in a stand of widely-spaced trees. *PHOENICS Journal of Computational Fluid Dynamics and Its Applications 23*, 294–312.

Green, S.R., Grace, J., Hutchings, N.J., 1995: Observations of turbulent air flow in three stands of widely spaced Sitka spruce. *Agr Forest Meteorol 74*, 205-225.

Hamdi, R., Masson, V., 2008: Inclusion of a drag approach in the Town Energy Balance (TEB) Scheme: Offline 1-D evaluation in a street canyon. *J Appl Meteorol Clim 47*, 2627-2644.

Hargreaves, D.M., Wright, N.G., 2007: On the use of the $k-\varepsilon$ model in commercial CFD software to model the neutral atmospheric boundary layer. *J Wind Eng Ind Aerod 95*, 355–369.

Katul, G.G., Mahrt, L., Poggi, D., and *Sanz, C.*, 2004: One and two equation models for canopy turbulence. *Bound-Lay Meteorol 113*, 81–109.

Kristóf, G., Rácz, N., Balogh, M., 2009: Adaptation of pressure based CFD solvers for mesoscale atmospheric problems. *Bound-Lay Meteorol 131*, 85-103.

Otte, T.L., Lacser, A., Dupont, S., and *Ching, J.K.S.*, 2004: Implementation of an urban canopy parameterization in a mesoscale meteorological model. *J Appl Meteorol 43*, 1648-1665.

Lien, F-S., Yee, E., 2004: Numerical modelling of the turbulent flow developing within and over a 3-d building array, part I: A high-resolution Reynolds-averaged Navier-Stokes approach. *Bound-Lay Meteorol 112*, 427–466.

Lien, F-S., Yee, E., 2005: Numerical modelling of the turbulent flow developing within and over a 3-d building array, part III: A distributed drag force approach, its implementation and application. *Bound-Lay Meteorol 114,* 287–313.

Lien, F-S., Yee, E., Cheng, Y., 2004: Simulation of mean flow and turbulence over a 2d building array using high-resolution CFD and a distributed drag force approach. *J Wind Eng Ind Aerod 92,* 117-158.

Lien, F-S., Yee, E., Wilson, J.D., 2005: Numerical modelling of the turbulent flow developing within and over a 3-d building array, part II: A mathematical foundation for a distributed drag force approach. *Bound-Lay Meteorol 114,* 245–285.

Liu, Z., Chen, J.M., Black, T.A., and *Novak, M.D.*, 1996: $E-\varepsilon$ modelling of turbulent air flow downwind of a model forest edge. *Bound-Lay Meteorol 77*, 21–44.

Sanz, C., 2003: A note on $k-\varepsilon$ modelling of vegetation canopy air-flows. *Bound-Lay Meteorol 108*, 191–197.

Sanz, C., Katul, G.G., 2007: Dual length scale two-equation modelling of the canopy turbulent kinetic energy wake budget. *C. R. Mecanique 335,* 685–690.

Shih, T.-H., Liou, W.W., Shabbir, A., Yang, Z., and *Zhu, J.*, 1995: A new $k-\varepsilon$ Eddy-viscosity model for high Reynolds number turbulent flows – Model development and validation. *Comput Fluids 24*, 227-238.

Vu, T.C., Ashie, Y., and *Asaeda, T.*, 2002: A $k-\varepsilon$ turbulence closure model for the atmospheric boundary layer including urban canopy. *Bound-Lay Meteorol 102*, 459–490.

In memoriam: Dezső Dévényi (1948–2009)

By now, we all know the stubborn facts: on November 26 *Dezső Dévényi* suddenly passed away of a heart attack in Boulder, Colorado. Maybe we are over the first shock, but it is still impossible to understand and comprehend that Dezső is not among us any more, and surely we are unable to account how much Hungarian and international meteorology lost with his death.

Dezső was born in Keszthely, attended the Eötvös Loránd University in Budapest, and he received his MSc degree in meteorology and teacher of mathematics/physics in 1973. During his entire career his scientific interest was devoted to the mathematical problems of meteorology. His basic interest towards atmospheric data assimilation (the statistical aspects at that time) started in the mid-70s, when he had several visits to the Soviet Union (in Leningrad, now St. Petersburg), and he had the opportunity to meet and work with *Lev Gandin*, the father of atmospheric optimal interpolation. This interaction probably determined his later scientific interest within meteorology, which was numerical weather prediction and mainly data assimilation. Later he co-authored (with *Ottó Gulyás*) a book entitled "Mathematical Statistical Methods in Meteorology". This is still an important reference in statistical training for Hungarian students reading

meteorology. In the second part of the 1980s he played a major role in the establishment of operational numerical weather prediction in Hungary by initiating cooperation with the Swedish Meteorological and Hydrological Institute (SMHI) in order to adapt their limited area model. Besides putting the SMHI model into operations, this adaptation work also led to the establishment of a small NWP team (consisting of 3–4 scientists at that time), which was the nucleus of the recent (much larger) NWP team of the Hungarian Meteorological Service. He was one of the early pioneers who visited Météo France in March 1991, to discuss and assess the feasibility of the LAM-ARPEGE project, which later became known as ALADIN. (And now it is an essential numerical weather prediction project not only in Central Europe, but also including the HIRLAM countries, who are now working on code cooperation with the ALADIN group.) He received his scientific degree at the Hungarian Academy of Sciences (which was later recognized as a PhD at the Eötvös Loránd University) in 1991 with a thesis entitled "The Application of Satellite Data in the Objective Analysis of Meteorological Fields". Dezső joined NOAA's Forecast Systems Laboratory in Boulder, Colorado for the first time between 1991 and 1993. After a short break for a return to Hungary, he continued his work in the US from 1995 to 1999 and, after another "Hungarian" break, from 2000 onwards. His work in the US was closely related to data assimilation with the development of the Rapid Update Cycle (RUC) and later Rapid Refresh (RR). During his years in Hungary he had several managerial positions (the highest being vice president) at the Hungarian Meteorological Service, but his main interest focused on the scientific aspects (rather than the administrational ones) of meteorology. In 1996, he was awarded the Doctor Habilitationis Degree by the Eötvös Loránd University, where he became an Associate Professor between 1999 and 2004.

Besides his official positions at the Hungarian Meteorological Service, Dezső was active in the social life of meteorology as well. He was a member of the Hungarian Meteorological Society, the Mathematical Society of Hungary, and lately the American Meteorological Society, too. He attained membership and became elected chairman of various Working Committees of the Hungarian Academy of Sciences (for Observations and Data Assimilation, Atmospheric Dynamics, Climate). He was member of the Editorial Board of the IDŐJÁRÁS (Quarterly Journal of the Hungarian Meteorological Service), where he made important contributions both as author and reviewer of numerous scientific papers.

Dezső was also famous for his passion of reading professional (during the early mornings) and recreational literature (in the evenings). He had a very extensive library on various topics of mathematics and physics, but he was also a fan of science fiction literature. He had a keen interest in sports, especially football, and avidly followed European sport events, football championships, and major international tournaments as much as time permitted. He very much regretted that in the United States opportunities to watch good football matches

were limited. This was just another reason, why, in the last years, he planned his final return to Hungary.

Dezső was a well-known and recognized person in the Hungarian meteorological society in spite of the fact that for the last 15 years he had been mostly living in the United States. His special, sometimes ironic and sarcastic sense of humor was highly appreciated. He kept in contact with many of us, and when he came home for a short visit, he never forgot to meet with old colleagues and friends and regularly presented his scientific achievements at the Hungarian Meteorological Society. Dezső was a great teacher of numerical weather prediction for an entire generation of Hungarian meteorologists. Many of us now working in numerical weather prediction or other related fields recognize him as our mentor. He was much more than that for some of us, for those having everyday contacts even when he was far away in space, but not in thoughts. It just means that many of us miss him tremendously, but we will always remember him as the "father" of numerical weather prediction in Hungary, a colleague who never forgot his roots in Hungary, and a friend to whom we could always address questions, being sure to get the most appropriate answers almost immediately.

Although this remembrance is a farewell to Dezső on the pages of IDŐJÁRÁS, we will never forget him, and we will follow the tracks he laid down for numerical weather prediction.

András Horányi and *Gábor Radnóti*

INSTRUCTIONS TO AUTHORS OF *IDŐJÁRÁS*

The purpose of the journal is to publish papers in any field of meteorology and atmosphere related scientific areas. These may be

- research papers on new results of scientific investigations,
- critical review articles summarizing the current state of art of a certain topic,
- short contributions dealing with a particular question.

Some issues contain "News" and "Book review", therefore, such contributions are also welcome. The papers must be in American English and should be checked by a native speaker if necessary.

Authors are requested to send their manuscripts to

Editor-in Chief of IDŐJÁRÁS
P.O. Box 39, H-1675 Budapest, Hungary
E-mail: antal.e@met.hu

including all illustrations. MS Word format is preferred in electronic submission. Papers will then be reviewed normally by two independent referees, who remain unidentified for the author(s). The Editor-in-Chief will inform the author(s) whether or not the paper is acceptable for publication, and what modifications, if any, are necessary.

Please, follow the order given below when typing manuscripts.

Title page: should consist of the title, the name(s) of the author(s), their affiliation(s) including full postal and e-mail address(es). In case of more than one author, the corresponding author must be identified.

Abstract: should contain the purpose, the applied data and methods as well as the basic conclusion(s) of the paper.

Key-words: must be included (from 5 to 10) to help to classify the topic.

Text: has to be typed in single spacing on an A4 size paper using 14 pt Times New Roman font if possible. Use of S.I. units are expected, and the use of negative exponent is preferred to fractional sign. Mathematical formulae are expected to be as simple as possible and numbered in parentheses at the right margin.

All publications cited in the text should be presented in the *list of references*, arranged in alphabetical order. For an article: name(s) of author(s) in Italics, year, title of article, name of journal, volume, number (the latter two in Italics) and pages. E.g., *Nathan, K.K.,* 1986: A note on the relationship between photo-synthetically active radiation and cloud amount. *Időjárás 90,* 10-13. For a book: name(s) of author(s), year, title of the book (all in Italics except the year), publisher and place of publication. E.g., *Junge, C.E.,* 1963: *Air Chemistry and Radioactivity.* Academic Press, New York and London. Reference in the text should contain the name(s) of the author(s) in Italics and year of publication. E.g., in the case of one author: *Miller* (1989); in the case of two authors: *Gamov* and *Cleveland* (1973); and if there are more than two authors: *Smith et al.* (1990). If the name of the author cannot be fitted into the text: *(Miller,* 1989); etc. When referring papers published in the same year by the same author, letters a, b, c, etc. should follow the year of publication.

Tables should be marked by Arabic numbers and printed in separate sheets with their numbers and legends given below them. Avoid too lengthy or complicated tables, or tables duplicating results given in other form in the manuscript (e.g., graphs).

Figures should also be marked with Arabic numbers and printed in black and white or color (under special arrangement) in separate sheets with their numbers and captions given below them. JPG, TIF, GIF, BMP or PNG formats should be used for electronic artwork submission.

Reprints: authors receive 30 reprints free of charge. Additional reprints may be ordered at the authors' expense when sending back the proofs to the Editorial Office.

More information for authors is available: antal.e@met.hu

Published by the Hungarian Meteorological Service

Budapest, Hungary

INDEX 26 361

HU ISSN 0324-6329